

Atomistic Modeling of Chemical Disorder in Materials: Bridging Classical Methods and AI-Assisted Approaches

Jiayu Peng,^{1,*} Peichen Zhong^{2,*}

¹Department of Materials Design and Innovation,
University at Buffalo, Buffalo, NY 14260, USA;

²Department of Materials Science and Engineering,
National University of Singapore, Singapore 117575, Singapore;

*Correspondence: jypeng@buffalo.edu (J.P.), zhongpc@nus.edu.sg (P.Z.)

Chemical disorder, originating from the mixed occupation of crystallographic sites by multiple elements, is widespread in metal alloys, ceramics, and other compositionally complex materials, where short- and long-range orderings can strongly influence their properties. Despite this importance, a central obstacle is the representation gap between experiments and simulations. Experiments often report disorder as partial occupancies and ensemble-averaged behaviors, whereas atomistic simulations and AI workflows usually require fully specified configurations. Tackling this gap requires computational methods that convert averaged disorder descriptions into representative configurational ensembles, while balancing cost, bias, and fidelity. This challenge has become more urgent in AI-driven computational discovery, where ignoring disorder may lead to AI workflows that misrank stability, misjudge novelty, and misdirect experiments with too-idealized representations. This Review systematically highlights how classical and AI-driven methods can bridge this representation gap. We assess the pros and cons of classical and AI-enabled approaches, spanning mean-field theories, cluster expansion, quasi-random approximations, Monte Carlo, and emerging schemes powered by the recent development of universal interatomic potentials and generative models. We further highlight how AI can accelerate classical computational schemes by lowering the cost of microstate evaluation, configurational exploration, and atomistic-to-thermodynamic closure. We also emphasize how AI can enable disorder-native capabilities, including disorder-aware workflow triage, new ordering-sensitive and alchemical representations, generative models of disordered structures and configurational distributions, and kinetics-aware prediction of processing-dependent disorder. Together, this framework outlines a practical roadmap toward disorder-native AI, which can transform chemical disorder from a representational obstacle into an essential, controllable parameter for realistic AI-accelerated materials discovery.

Table of Contents

Abstract	2
1. Introduction	5
2. Classical first-principles methods for disorder modeling	13
2.1 Effective-medium and mean-field theories	14
Virtual crystal approximation (VCA)	15
Coherent potential approximation (CPA)	15
2.2 Cluster-expansion-based on-lattice statistical mechanics	17
Theoretical foundations and formalism	17
Practical use and considerations	19
2.3 Quasi-random structural approximations	22
Special quasi-random structure (SQS) method	22
Relevant quasi-random approximations	24
2.4 Ensemble-based microstate averages	25
General framework	26
Partial OCCupation (POCC) formalism	26
Relevant finite-ensemble approaches	27
2.5 Stochastic sampling and molecular dynamics	29
Direct Monte Carlo sampling	29
Enhanced Monte Carlo strategies	30
Hybrid Monte Carlo–molecular dynamics methods	30
Relaxation-swap methods	31
Basin-hopping and minima-hopping methods	31
Genetic and evolutionary algorithms	32
2.6 Macroscopic thermodynamic models	32
Simplified thermodynamic screening descriptors	33
CALculation of PHAse Diagrams (CALPHAD)	34
3. Modern AI-assisted approaches for disorder modeling	35
3.1 ML as an accelerator for existing modeling formalisms	36
Accelerating microstate evaluations	37
Accelerating ensemble workflows	41
Accelerating thermodynamic closure	42
3.2 ML as an enabler for novel disorder-native capabilities	44

Enabling disorder-aware workflow triage	45
Enabling ordering-sensitive and alchemical representations	46
Enabling disordered structure and distribution generation	51
Enabling processing-aware disorder kinetic prediction	53
4. Grand challenges and future perspectives	55
4.1 Phase-level fidelity calibration and theory–experiment alignment	56
4.2 Disorder-native data, benchmarks, and uncertainty quantification	58
4.3 Disorder beyond site occupations: defect, charge, and magnetism	60
4.4 Multi-modal characterization as an inverse problem for disorder	61
4.5 Beyond bulk disorder: interfaces and heterogeneous environments	62
References	65

1. Introduction

Chemical disorder is widespread in materials and can often play an essential role in their phase stability and functional properties. It appears across a broad range of material classes, including metal alloys, ceramics, and other compositionally complex solids, where multiple elements may share crystallographic lattices in ways that are not perfectly ordered.¹ Such disorder can exhibit many forms, such as substitutional disorder in alloys,² cation disorder in oxides,³ anion disorder in mixed anion compounds,⁴ and vacancy disorder in defect-rich materials.⁵ The landscape of disorder becomes even richer in high-entropy and compositionally complex compounds, where six or more principal elements coexist on one or more sublattices.^{6–8} As these variations in local chemical compositions directly reshape bonding environments, they can strongly influence how a material stores charges,⁹ conducts electrons,¹⁰ controls diffusion,¹¹ catalyzes reactions,¹² and deforms under stress¹³ and radiation.¹⁴ For example, chemically disordered rocksalt cathodes¹⁵ and high-entropy solid electrolytes¹⁶ can exhibit unique transport and electrochemical behaviors relevant to energy storage in Li-ion batteries, while high-entropy alloys with different degrees of chemical disorder can possess significant differences in surface reactivity¹⁷ and durability.¹⁸ Therefore, chemical disorder is not a niche structural detail, but a crucial and tunable parameter that must be defined and understood clearly before optimizing materials systematically.

In solid materials, it is crucial to conceptually differentiate chemical (occupational) disorder from structural (positional) disorder, while recognizing that compositionally complex systems frequently couple the two (Fig. 1). Broadly speaking, disorder in materials refers to deviations from perfect crystalline order, but these deviations can arise either from how chemical species are distributed across lattice sites or from where atoms are positioned in space.^{19–21} Specifically, chemical disorder captures the probabilities of having multiple elements occupying equivalent crystallographic sites.¹ For instance, metal alloys with the lowest or highest degree of chemical disorder are intermetallics or random solid solutions, respectively.²² By contrast, for structural disorder, the dominant deviation lies in atomic positions rather than site identity,²³ as in crystals with substantial lattice distortions, defects, or displaced atoms that disrupt ideal periodicity. As examples, perovskite oxides can exhibit various types of structural disorder through octahedral tilting, Jahn–Teller distortion, and oxygen non-stoichiometry,²⁴ while materials with the utmost degree of structural disorder are amorphous solids lacking any crystalline lattices.²⁵ At the same time, these two families of disorder are often linked in practice rather than cleanly separable. In high-entropy alloys, for example, the random placement of differently sized and bonded atoms can perturb the surrounding lattices and induce local displacements, in which chemical disorder is accompanied by local structural distortions.^{26,27} Considering such distinction and correlation, this Review particularly focuses on disordered materials dominated by chemical disorder, even though readers can look elsewhere^{28–35} for broader perspectives on structural disorder.

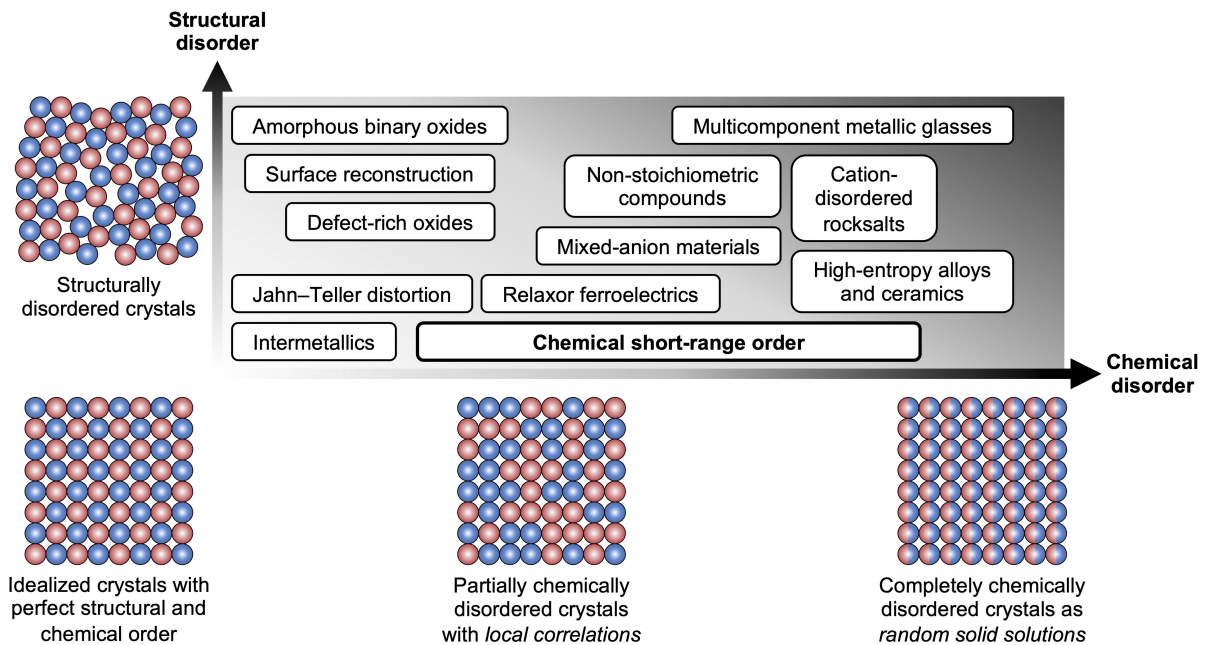


Fig. 1. Conceptual distinction and coupling between chemical and structural disorder. Schematic illustration of disorder in solid materials along two conceptual axes: chemical disorder (horizontal axis), describing the extent to which different species occupy crystallographic sites in an ordered, correlated, or random manner, and structural disorder (vertical axis), showing deviations of atomic positions from an ideal periodic lattice. The lower schematics indicate a continuum of chemical ordering, ranging from a perfectly ordered crystal (left), to a partially disordered crystal with local correlations or chemical short-range order (middle), to a completely chemically disordered crystal as a random solid solution (right). The upper-left schematic shows a structurally disordered material with markedly displaced atomic positions. Red and blue spheres denote different chemical species. Representative classes of solid materials are positioned within this space to illustrate typical combinations of chemical and structural disorder. The placements are qualitative to emphasize that disorder in materials is a continuum, rather than a binary classification.

Critically, chemical order and disorder are not a simple dichotomy, but instead they define a continuous spectrum that might span fully ordered, partially ordered, and dominantly disordered states (Fig. 1). Under various conditions, a material can possess long-range chemical order,³⁶ lose this order only partially,³⁷ or appear disordered on average while still retaining meaningful local correlations.^{38,39} On the one hand, compositionally complex materials with many elements that tend to achieve chemically disordered states may instead form highly ordered intermetallic lattices.^{40–43} On the other hand, the absence of long-range order in materials does not necessarily imply completely random mixing, because short-range order can persist through preferred local motifs, clustering tendencies, or avoidance between specific species.^{44,45} This continuity makes chemical disorder fundamentally a question of degree, length scale, and correlation, rather than a binary classification problem. These intermediate states can be the most scientifically crucial, as a modest change in local ordering may alter the distribution of atomic environments, without modulating the average crystal symmetry or electronic structure in an abrupt way.⁴⁶ As a result, materials that appear similarly disordered at the average-structure level may behave differently if their local chemical correlations differ. Framing chemical disorder as a continuum thus offers a robust foundation for understanding how to co-design short- and long-range orderings.

This continuum of chemical order and disorder can be physically understood by treating it as a statistical-mechanics problem, where the structure is linked to an ensemble of site-occupancy microstates selected by free-energy minimization. In this framework, disorder does not simply imply the lack of any visible ordering, but rather reflects the number of microscopic possibilities that are compatible with the macroscopic constraints of composition, temperature, pressure, and other parameters. Specifically, for chemically disordered solids, the key degrees of freedom are configurational: each microstate corresponds to a particular assignment of chemical species to crystallographic sites, and the resulting material behaviors depend on the statistical distribution of these site-occupancy patterns rather than on any configuration alone (Fig. 2a). This treatment connects chemical disorder to the configurational entropy.^{50,51} For a fully random solid solution (i.e., the ideal mixing limit), the configurational entropy (ΔS_{conf}) reaches its highest value:

$$\Delta S_{\text{conf}} = -Nk_{\text{B}} \sum_i x_i \ln x_i \quad (1)$$

where N is the total number of lattice sites, k_{B} is the Boltzmann constant, and x_i is the fraction of sites occupied by species i . While this ideal expression is useful, it assumes that all possible microscopic atomic arrangements have exactly the same energy and are thus equally probable. Real materials, however, are rarely this simple, as various pairs of chemical species can interact differently, making specific local atomic arrangements energetically more favorable than others. A simple way to move beyond ideal mixing is to keep the entropy term but add an energetic cost for unlikely neighbors. An example is the regular solution model,^{52–54} which keeps the entropy

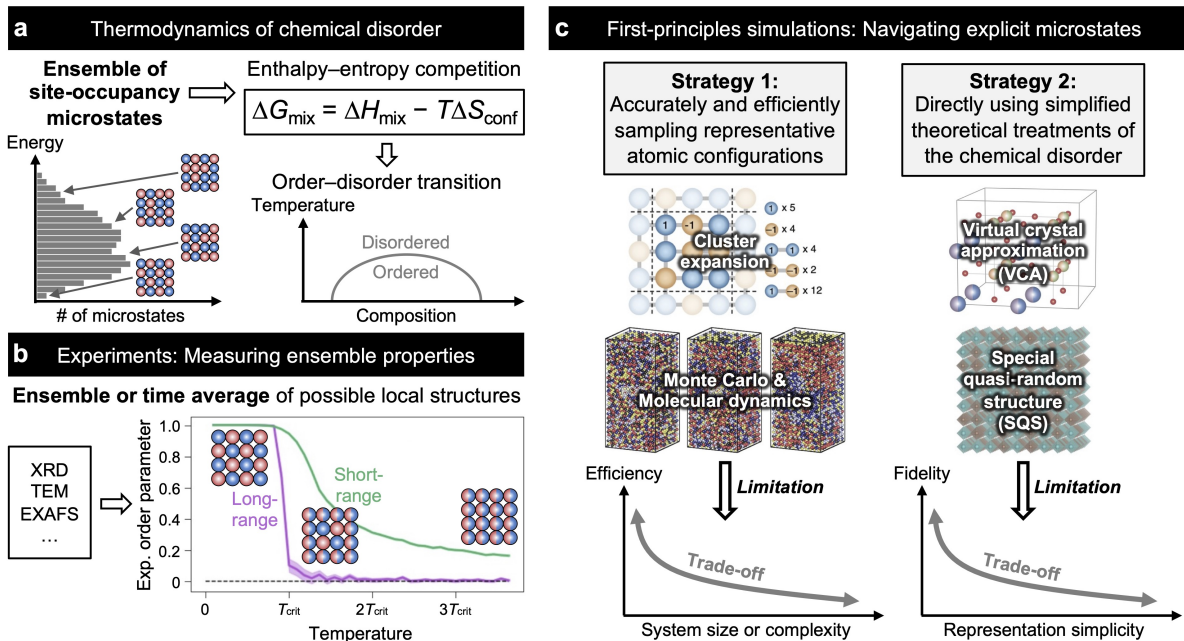


Fig. 2. Comparing thermodynamic, experimental, and computational perspectives on chemical disorder. (a) Chemical disorder is fundamentally a statistical-mechanics problem, stemming from many possible site-occupancy microstates with various energies. Its equilibrium properties are governed by the competition between the enthalpy of mixing and configurational entropy, which gives rise to temperature- and composition-dependent order–disorder transitions. (b) Experiments examine chemical disorder primarily through ensemble- or time-averaged observables rather than a unique atomically resolved configuration. Key techniques, e.g., X-ray diffraction (XRD), transmission electron microscopy (TEM), and extended X-ray absorption fine structure (EXAFS), typically yield averaged order descriptors across many local structures. The schematic indicates that the long-range order descriptor vanishes near a critical temperature, whereas the short-range order descriptor may persist to much higher temperatures, reflecting surviving local chemical correlations in many nominally disordered materials. (c) This leads to a critical challenge in disorder modeling: although experiments can directly get averaged properties of interest in disordered materials, to compute such properties, atomistic simulations still need to assess numerous explicit microstates over a massive configurational ensemble. Two broad strategies have been used. The first strategy explicitly samples representative configurations using classical methods (such as cluster expansion, Monte Carlo, and molecular dynamics), but they face a trade-off between efficiency and the need to increase system size or complexity. The second strategy builds upon simplified theoretical treatments of disorder (e.g., the virtual crystal approximation and special quasi-random structures), which can enhance tractability but may sacrifice fidelity to local chemical correlations. Together, these panels show the gap between the characterization and modeling of chemically disordered solids. Panel (b) adapted with permission from ref.⁴⁷, copyrighted by Springer Nature. Panel (c) adapted from refs.^{3,48,49}, CC BY 4.0.

of ideal mixing, but with an extra enthalpic penalty or preference for driving random mixing of different elements. In this framework, the Gibbs free energy of mixing (ΔG_{mix}) is:

$$\Delta G_{\text{mix}} = \Delta H_{\text{mix}} - T\Delta S_{\text{conf}} \quad (2)$$

where T is the temperature, and ΔH_{mix} is the enthalpy of mixing. For a binary system with site fractions x_A and x_B (i.e., $x_A + x_B = 1$), the enthalpic term is often approximated as:

$$\Delta H_{\text{mix}} = N\Omega x_A x_B \quad (3)$$

where Ω is an effective interaction parameter that describes whether two physically dissimilar neighbors (e.g., A–B) are enthalpically more favorable than similar ones (e.g., A–A and B–B): having $\Omega < 0$ facilitates the mixing of species A and B, while $\Omega > 0$ discourages their mixing. In this form, the enthalpic term represents the energetic preference for particular local chemical motifs, whereas the entropic term reflects the statistical tendency to access many configurations. Order–disorder transitions, therefore, emerge naturally from the compositional and temperature dependence of this entropy–enthalpy competition.^{37,55–59} As an example, at lower temperatures, the enthalpic contribution dominates and favors ordered states, while at higher temperatures, the growing entropic contribution gives rise to more random, chemically disordered configurations. In mean-field pictures,² the long-range order parameter can decrease continuously to zero at the critical ordering temperature, but even when long-range order disappears, local energetic biases can still preserve short-range chemical correlations, so that nominally disordered materials often remain far from completely random solid solutions. Altogether, thermodynamics determines the equilibrium tendency toward chemical order or disorder. Furthermore, kinetics might play a key role, as diffusion barriers, finite annealing times, and non-equilibrium operating conditions may hinder the system from reaching its thermodynamic ground state, preserve metastable disorder, or freeze in localized chemical correlations during synthesis, processing, and usage.^{36,60–65}

Experimentally, chemical disorder is usually not unambiguously resolved atom-by-atom as a specific configuration, but is instead inferred from measurements that capture an ensemble or time average of atomic structures over many local arrangements. This is exactly why no single technique fully resolves chemical disorder on its own, and why complementary measurements are needed across multiple length scales. In diffraction-based crystallography, Bragg scattering primarily encodes the average periodic structure, such as lattice symmetries, lattice parameters, and fractional site occupancies, while superlattice reflections further reveal the presence of long-range chemical order.³⁶ When deviations from the average periodic structure become important, diffuse scattering and pair distribution function analysis can be especially valuable, because they retain information about occupational and displacive correlations that are not captured by Bragg peaks alone, including short-range order.^{66,67} Complementary spectroscopies, such as extended

X-ray absorption fine structure, can further reveal element-specific coordination environments, local symmetry breaking, and preferred nearest-neighbor chemistries,^{68,69} whereas imaging and chemical mapping methods can provide projected local motifs, three-dimensional neighborhood statistics, and direct evidence of compositional heterogeneity.^{15,21,39,70} From these experiments, ensemble-averaged order descriptors can be derived (Fig. 2b). To characterize long-range order, a widely used quantitative descriptor is the sublattice order parameter² (η):

$$\eta = c_X^{\text{I}} - c_X^{\text{II}} \quad (4)$$

for a binary alloy on two sublattices, where c_X^{I} and c_X^{II} are the fractions of species X occupying sublattices I and II, respectively. Having $\eta = 0$ indicates a random distribution, while a larger $|\eta|$ indicates stronger long-range chemical ordering. In addition, for short-range order, a widely leveraged shell-resolved order descriptor is the Warren–Cowley parameter^{47,71,72} (ζ_{ij}^m):

$$\zeta_{ij}^m = 1 - \frac{P_{ij}^m}{x_j} \quad (5)$$

where P_{ij}^m is the probability that an atom of species i has a species j atom in its m th coordination shell, and x_j further denotes the overall concentration of species j in the material. By definition, $\zeta_{ij}^m = 0$ represents fully random mixing, whereas $\zeta_{ij}^m < 0$ highlights an enhanced preference for having i - j neighbors, and $\zeta_{ij}^m > 0$ indicates avoidance between species i and j , which has often been associated with local clustering or atomic segregation. Nonetheless, these experimentally derived order parameters remain a statistical average of an underlying configurational ensemble rather than an atomically resolved and unambiguously identified reconstruction of the full three-dimensional atomistic disorder. This limitation is critical, since average occupancies, shell-wise order parameters, and pair-correlation-based descriptors still cannot uniquely elucidate the exact arrangement of atoms in any given region.^{8,51,73} These experimental techniques suffer from high cost and low throughput, which makes them useful for analyzing selected samples but also limits their power in large-scale materials screening. In addition, experimental signatures traditionally regarded as evidence of short-range chemical order, e.g., diffuse features in electron diffraction of random alloys,⁷⁴ can be challenging to authenticate unambiguously, as they may alternatively arise from structural disorder, surface effects, or other symmetry-breaking artifacts.^{75,76} Overall, these pressing limitations necessitate the use and development of methods beyond experimental characterization to rationalize, engineer, and optimize chemical disorder in materials.

Computational approaches have shown great potential in addressing the intricate complexity of chemical disorder, but a crucial challenge in modeling such disorder is the mismatch between experiments and simulations, where experimental characterization typically captures ensemble-averaged behaviors, whereas atomistic modeling is generally performed on explicit microstates (Fig. 2c). As the properties of interest are usually determined by averages over many accessible

atomic arrangements, any realistic prediction of finite-temperature behaviors (or any meaningful comparison with experiments) must account for the configurational ensemble that is consistent with the chemical compositions and thermodynamic constraints of disordered solids, rather than relying on just a single deterministic structure. In practice, this challenge can be approached in two broad ways:^{47,73} one may explicitly sample many configurations and average their predicted properties, or one may directly employ effective theoretical treatments that represent underlying disorder statistically without enumerating every arrangement in full. Both strategies are highly valuable, but they both become progressively formidable with increasing numbers of elements, sublattices, defects, and local chemical correlations. For example, explicit sampling can quickly encounter a combinatorial explosion in the number of possible configurations, which can push first-principles calculations beyond practical limits.⁵⁵ Moreover, developing effective statistical descriptions can decrease the computational burden, but they might lose physical fidelity if the local chemical correlations that matter the most are oversimplified or neglected.⁴⁵ Consequently, simulations of chemical disorder are still severely constrained by the persistent trade-off among thermodynamic fidelity, computational cost, configurational bias, and scalability.

The rapid development of machine learning (ML) and artificial intelligence (AI) can bridge the gap between experiments and simulations and bypass the accuracy–cost trade-off in disorder modeling by boosting configurational sampling, energy minimization, and structural discoveries without omitting the disorder physics that exist in real materials (Fig. 3). State-of-the-art data-driven tools, e.g., universal interatomic potentials⁷⁷ and generative models,⁷⁸ can greatly expand the speed and scale of exploration, making broader sampling and faster screening more feasible than with direct first-principles simulations alone.⁷⁹ However, recent critiques of AI-accelerated computational materials discovery have also made clear that ML algorithms that cannot account for the various possibilities of chemical disorder can introduce major issues in high-throughput materials screening. High-throughput ML pipelines built around ordered, small-cell, effectively zero-temperature representations might over-predict highly ordered structures that are unlikely to persist at finite temperature, especially when configurational entropy would lead to disorder in real materials. In a recent example,⁸⁰ apparently “new” ordered predictions have been shown to correspond more realistically to already discovered disordered phases. More fundamentally, if disorder is ignored altogether, AI models may produce both false positives and false negatives by missing stabilizing or destabilizing effects that arise directly from local chemical randomness and short-range correlations.^{47,73} Therefore, ML and AI are not simply a faster replacement for physics-based modeling, but must themselves become physically sound and explicitly disorder-aware to reliably boost the understanding and design of chemical disorder in materials.

In this Review, we highlight the evolution and convergence of classical atomistic simulation methods and modern ML approaches as complementary computational tools to enable accurate,

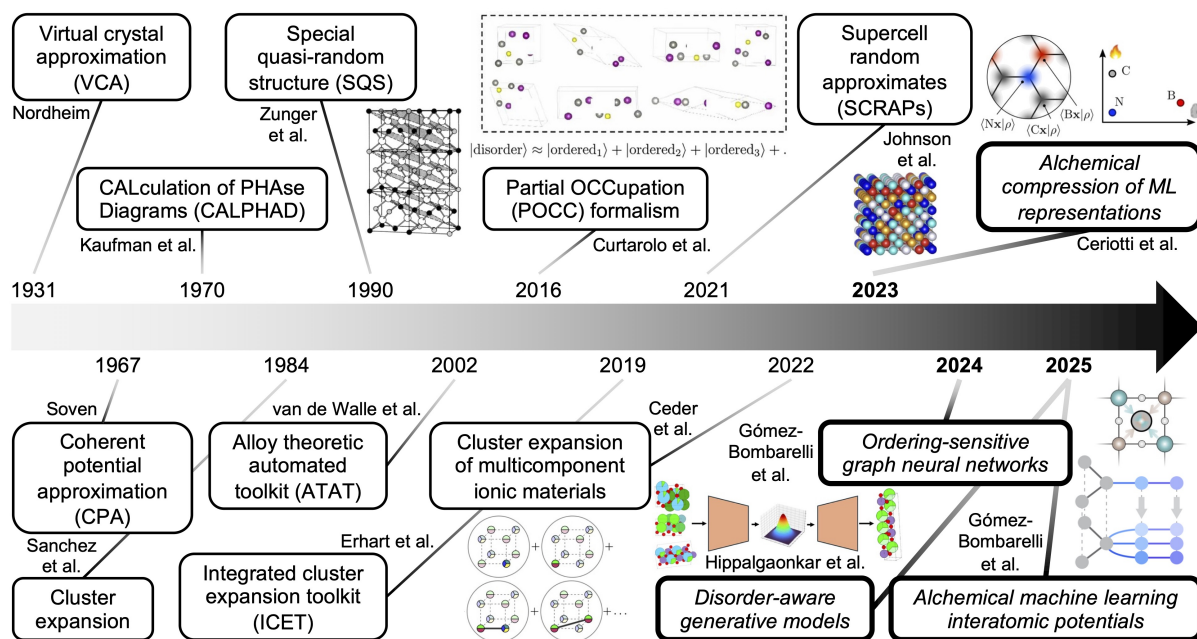


Fig. 3. Selected milestones in the development of computational methods for modeling chemically disordered materials. Chronological schematic illustrating essential methodological advances in modeling chemical disorder over nearly a century. Early computational approaches center on replacing explicit configurational complexity with effective averaged descriptions, which provide tractable mean-field or thermodynamic treatments of substitutional disorder without enumerating all atomic arrangements.^{81–83} A complementary line of development introduces more explicit configurational representations via cluster expansion (including its various implementations and extensions to more complex systems), thereby facilitating statistically grounded descriptions of configurational energetics and finite-temperature ordering.^{84–87} Moreover, structure-centered approximations are developed to represent chemical disorder with carefully designed quasi-random supercells that aim to mimic selected ensemble-averaged correlation functions, while remaining computationally practical for first-principles modeling.^{88–91} Beyond classical methods, recent milestones highlight the growing integration of ML into disorder modeling, which promotes configurational exploration, strengthens transferability across diverse complex chemical compositions, and preserves sensitivity to various coordination environments.^{92–95} Together, this timeline emphasizes the historical evolution from simplified average-atom and thermodynamic formalisms toward increasingly explicit, scalable, and data-driven treatments of disorder, while showing the ongoing convergence of classical statistical-mechanics methods and modern AI tools. The milestones shown here are intended as representative landmarks, rather than an exhaustive history of the field. Figure adapted from refs.^{87,93–95}, CC BY 4.0, and with permission from refs.^{89,91,92,96}, copyrighted by the American Physical Society and Springer Nature, respectively.

efficient, and physically robust atomistic modeling of chemically disordered materials (Fig. 3). Building on the combinatorial nature of configurational ensembles in disordered materials, we frame disorder modeling as a problem of how to represent, sample, and average over chemically complex microstates to ensure sufficient thermodynamic fidelity and minimal selection bias. We systematically compare the major strengths and key limitations of representative first-principles approaches, such as effective-medium and mean-field theories, cluster expansion, quasi-random structural approximations, ensemble-based averages, stochastic sampling, molecular dynamics, and macroscopic thermodynamic models—alongside rapidly emerging ML-driven schemes that might transform traditional simulation workflows using machine learning interatomic potentials (MLIPs), ordering-aware graph neural networks (GNNs), and generative AI. We emphasize not only the key benefits and drawbacks of individual approaches in throughput, accuracy, bias, and transferability but also illustrate how different tools can be combined, where classical methods supply interpretable thermodynamic formalisms, while ML further expands sampling scale and screening scope without discarding essential disorder physics. Finally, by examining remaining challenges in disorder modeling, we outline a forward-looking roadmap for developing physics-driven, disorder-predictive AI that integrates seamlessly with established statistical-mechanics formalisms and complex experimental observables, with the goal of promoting robust, unbiased elucidation and enabling accurate, efficient optimization of chemically disordered materials.

Table 1. Comparison of representative classical simulation methods for modeling chemical disorder.

Method category	Disorder representation	Sampling	Fidelity	Efficiency	Scalability
Effective-medium and mean-field theories (e.g., VCA and CPA)	Direct partial occupancy via averaged medium	No	Very low	High	High
Cluster-expansion-based on-lattice statistical mechanics (possibly with Monte Carlo)	Explicit on-lattice microstates via fitted Hamiltonian	Extensive	High	Medium	Medium
Quasi-random structural approximations (e.g., SQS)	One or a few supercells matching desired local chemical correlations	No ¹	Medium	High	Medium
Ensemble-based microstate averages (e.g., POCC)	Many explicit microstates with statistical averaging	Limited	High	Low	Low
Stochastic sampling and molecular dynamics	Explicit site occupations, usually coupled with atomic relaxations	Extensive	Very high	Very low ²	Low
Macroscopic thermodynamic models (e.g., CALPHAD)	Direct partial occupancy via analytical, empirical free-energy models	No	Low	High	High

¹ Excluding the negligible, one-time sampling during SQS construction.

² Might be accelerated substantially through parallel computing with GPU implementations, but remains expensive at the direct first-principles level.

2. Classical first-principles methods for disorder modeling

Classical approaches for modeling chemical disorder in solid materials can be understood most clearly with a crucial question: how can experimentally averaged, partially occupied disordered states be translated into a form that first-principles simulations can actually compute? Different methods address this question in fundamentally dissimilar ways (Table 1). Mean-field methods replace disordered crystals with an effective average medium. On the contrary, the most explicit approaches represent disorder through individual atomic configurations and recover observables by configurational averaging. Between these two limits lie a variety of classical strategies, each providing a distinct balance among physical realism, computational cost, and generality. Hence, the key distinction among diverse methods is not simply whether disorder is included, but rather how such disorder is represented, whether explicit sampling is required, and how experimentally meaningful properties are recovered from the underlying configurational landscape.

2.1 Effective-medium and mean-field theories

Effective-medium and mean-field theories^{81,82} offer the simplest way to connect experimentally reported partial occupancies with electronic-structure calculations. In experiments, a disordered crystal is typically described with an average representation, where a lattice site can be “partially species i and partially species j .” By contrast, standard first-principles simulations require fully specified crystal structures, where every crystallographic site is assigned to a definite atom. This mismatch is particularly crucial for density functional theory (DFT), because DFT solves for the ground-state electron density of an explicit arrangement of nuclei, as opposed to the ensemble average over various possible occupations. Consequently, conventional DFT for periodic solids cannot directly represent chemical disorder as partial site occupancy, unless one either samples many explicit configurations or uses an approximate averaged description of disorder.^{47,73}

Diverse effective-medium and mean-field methods have been developed precisely to bypass this limitation by replacing the many possible local atomic environments of a disordered crystal with a single averaged medium that can be directly treated within a periodic electronic-structure framework (Fig. 4a). The central idea behind them is to trade atomistic details for computational efficiency. Instead of enumerating or sampling the exponentially large set of configurations, one creates a translationally invariant “effective crystal structure” whose properties approximate the configurational average of the truly disordered system. This strategy can be particularly natural for substitutional disorder on a well-defined parent lattice, where the goal is to estimate average trends in phase stability,⁹⁷ electronic structure,⁹⁸ and functional properties⁹⁹ as the composition changes. This approximation has been especially influential in modeling metallic alloys, where the underlying disorder mainly broadens electronic states and renormalizes average interactions,

while the crystalline lattice structures of these materials remain relatively well-defined.

Virtual crystal approximation (VCA). VCA is the simplest realization of this averaging idea and is best viewed as a DFT-compatible approximation to partial site occupancy.⁸¹ Specifically, in VCA, a disordered site shared by two species i and j is replaced by a “fictitious atom” whose effective ionic potential ($V_{\text{VCA}}(\mathbf{r})$) is the composition-weighted average of the constituents:

$$V_{\text{VCA}}(\mathbf{r}) = x_i V_i(\mathbf{r}) + x_j V_j(\mathbf{r}) \quad (6)$$

where $V_i(\mathbf{r})$ and $V_j(\mathbf{r})$ indicate the site-centered ionic potentials of species i and j at position \mathbf{r} , respectively, while x_i and x_j are their corresponding concentrations. Through this treatment, the crystal remains perfectly periodic, so the problem can be treated using essentially the same standard first-principles machinery as an ordered solid. In practice, VCA is often implemented in periodic DFT calculations with averaged pseudopotentials⁹⁹ or closely related mixed-species constructions,⁹⁷ making it widely used to quickly estimate composition-dependent trends.

VCA is useful for reducing chemical disorder to a single periodic DFT calculation, but such a simplification is also its central weakness, as it removes the local fluctuations that often matter the most in disordered materials. Since no supercell construction or configurational sampling is required, VCA keeps the computational cost close to that of an ordered DFT calculation and is thus well suited for rapid scans of alloy compositions, approximate band filling, average lattice parameters, and broad energetic trends.^{97–99} This high efficiency has been particularly beneficial when the constituent elements in alloys are chemically similar, the lattice remains close to ideal, and the properties of interest depend primarily on smooth average behaviors.^{100,101} For instance, VCA has recently been applied to elucidate how Li ion transport is controlled by the short-range occupational order of mixed anions in disordered solid-state electrolytes.¹⁰² Nevertheless, since every site experiences the same averaged potential, VCA neglects site-to-site fluctuations, alloy scattering, local charge redistribution, unequal bond lengths, and short-range chemical order.⁹⁹ Therefore, it cannot capture disorder-induced band broadening, local lattice relaxations caused by size mismatch, or environment-specific bonding effects. As a result, VCA becomes markedly unreliable when disorder strongly couples to strain, localized electronic states, electronegativity differences, or bonding heterogeneity. In broad terms, VCA works best for weakly perturbative random alloys, but poorly for highly ionic–covalent and significantly distorted materials.

Coherent potential approximation (CPA). CPA goes beyond VCA’s simple representations by replacing a disordered material not with an averaged potential, but using an effective medium that reproduces the average scattering of electrons from its random lattice.⁸² Thus, CPA offers a more natural electronic-structure description of lattice disorder, especially when such disorder

broadens bands and influences transport. Formally, CPA approximates the exact configurational average of the one-electron Green’s function of a randomly substituted alloy:¹⁰³

$$\langle \mathcal{G}(z; \sigma) \rangle_{\sigma} \approx \bar{\mathcal{G}}(z) = \left[z - \hat{\mathcal{H}}_0 - \Sigma_{\text{CPA}}(z) \right]^{-1} \quad (7)$$

where $\mathcal{G}(z; \sigma)$ denotes the one-electron Green’s function for a particular atomic configuration σ , and $\langle \mathcal{G}(z; \sigma) \rangle_{\sigma}$ further represents the configurational average over all possible occupations. Moreover, $\bar{\mathcal{G}}(z)$ denotes the Green’s function of the coherent effective medium, z is the complex energy with an infinitesimal positive imaginary part, \mathcal{H}_0 is the periodic part of the Hamiltonian defined on the parent lattice, and $\Sigma_{\text{CPA}}(z)$ denotes the energy-dependent coherent potential (or effective self-energy) that represents the average scattering of this random alloy. Although this formalism might appear slightly abstract, its physical meaning is straightforward: CPA seeks a self-consistent medium in which replacing an average site by a real atomic species can produce, on average, no additional scattering. Hence, standard CPA is a single-site, mean-field theory, in which each site is embedded in an averaged environment. In first-principles calculations, CPA is most commonly combined with DFT through Green’s-function-based implementations, such as Korringa–Kohn–Rostoker CPA, where the substitutional disorder in mixed alloys is represented naturally through site-resolved scattering matrices on their fixed parent lattices.^{104–108}

CPA is powerful by capturing the average electronic consequences of substitutional disorder much more realistically than VCA while still avoiding explicit configurational sampling, but its single-site, effective-medium nature still limits the local physics it can describe. Compared with VCA, by retaining alloy scattering and disorder-induced spectral broadening, CPA gives a more realistic description of densities of states, magnetic moments, and transport properties, making it especially useful for random metallic alloys where electrons remain reasonably itinerant and the main role of disorder is to smear or renormalize the otherwise Bloch-like band structures.¹⁰⁹ As an example, CPA has been found to generate simulation results in excellent agreement with available experimental data for the optical gap in disordered transition metal dichalcogenides.¹¹⁰ Nevertheless, regarding limitations, because standard CPA still replaces the true configurational landscape with an averaged medium, it does not explicitly capture short-range order, clustering, pair or cluster correlations, local motif-dependent electrostatics, or local lattice relaxations such as unequal bond lengths and strain fields around mismatched atoms.⁸² These omissions become vital when local chemistry strongly affects the material behaviors, such as in some high-entropy alloys, ionic compounds, and covalent semiconductors with significant mismatch in atomic size or electronegativity.¹⁰³ Cluster and nonlocal extensions of CPA formalisms may recover part of this missing physics,¹¹¹ but the standard single-site form remains most reliable for substitutional disorder on an approximately undistorted parent lattice, e.g., in simple alloys.

Collectively, VCA and CPA occupy the most approximate but also the most computationally efficient end of the disorder modeling spectrum. Both methods can bypass explicit sampling by

replacing a disordered ensemble with an averaged medium, and both can be coupled with DFT to access composition-dependent properties at relatively low cost. VCA is the simpler and more broadly accessible approximation within periodic DFT workflows, while CPA is a more realistic choice when disorder scattering and spectral broadening are essential. However, both methods inherit the limitation of mean-field thinking: they capture only the average disordered state, not the distribution of local environments. This drawback has motivated the next family of methods, which keep the occupation variables explicit and treat configurational correlations directly.

2.2 Cluster-expansion-based on-lattice statistical mechanics

Cluster-expansion-driven methods approach chemical disorder in a fundamentally different way from the effective-medium and mean-field strategies. Rather than replacing a disordered crystal with an average representation, they treat this solid as an ensemble of explicit lattice-occupancy microstates and predict key properties by statistical averaging over the ensemble (Fig. 4b). This distinction matters, as local ordering, clustering, and order–disorder transitions are controlled by how many configurations are populated and how their energetics differ, not by a single averaged crystal. Hence, cluster expansion keeps the configurational physics that mean-field descriptions intentionally smooth out, while providing a practical route to finite-temperature prediction.

Theoretical foundations and formalism. The technical starting point of cluster expansion is to describe chemical disorder via a configurational ensemble on a parent lattice. In the canonical ensemble, the probability (P_s) of a microstate s with energy E_s at temperature T is:¹¹²

$$P_s = \frac{\exp(-\beta E_s)}{Z} \quad (8)$$

where $\beta = 1/(k_B T)$, k_B is the Boltzmann constant, and Z is the partition function:

$$Z = \sum_s \exp(-\beta E_s) \quad (9)$$

For chemically disordered materials, one can coarse-grain the problem by grouping together all vibrational and electronic states relevant to an occupational configuration σ . This treatment can lead to a configuration-dependent free energy $F(\sigma)$ and the equivalent expression:¹¹³

$$Z = \sum_{\sigma} \exp[-\beta F(\sigma)] \quad (10)$$

where the sum runs over all allowed occupational configurations. In this form, $F(\sigma)$ works as an effective free energy for the slow configurational degrees of freedom after the faster vibrational and electronic degrees of freedom have been coarse-grained out. In many practical applications, especially when the focus is on chemical ordering instead of vibrational thermodynamics, $F(\sigma)$

can be approximated by a lattice Hamiltonian built from the relaxed ground-state energy of each configuration.¹¹⁴ Earlier studies have shown that this approximation might shift order–disorder transition temperatures quantitatively, but it still preserves the overall topology of the computed phase diagrams.^{115–117} This coarse-graining approximation is what converts the complex many-body problem of chemical disorder into a lattice statistical-mechanics problem.

Cluster expansion provides the effective Hamiltonian that makes this configurational picture practical.^{84–87,118–123} Given a selected parent lattice, the configurational energy can be written as a sum over orbit-averaged cluster correlation functions, which allows both metallic alloys^{84,124} and lattice-based ionic systems^{125,126} to be effectively treated using the same general framework. For a multicomponent system, the configurational energy ($E(\boldsymbol{\sigma})$) is:⁴⁸

$$E(\boldsymbol{\sigma}) = \sum_{\omega} m_{\omega} J_{\omega} \Pi_{\omega}(\boldsymbol{\sigma}) \quad (11)$$

where ω denotes an orbit of symmetrically equivalent clusters, m_{ω} shows its multiplicity, J_{ω} is the effective cluster interaction (ECI), and $\Pi_{\omega}(\boldsymbol{\sigma})$ is the orbit-averaged correlation function:

$$\Pi_{\omega}(\boldsymbol{\sigma}) = \langle \Phi_{\alpha \in \omega}(\boldsymbol{\sigma}) \rangle_{\omega} \quad (12)$$

Here, $\Phi_{\alpha}(\boldsymbol{\sigma})$ is the corresponding basis function for a particular decorated cluster α :

$$\Phi_{\alpha}(\boldsymbol{\sigma}) = \prod_i \phi_{\alpha_i}(\sigma_i) \quad (13)$$

where σ_i specifies which species occupies site i , $\phi_{\alpha_i}(\sigma_i)$ is a site basis function, and $\langle \Phi_{\alpha \in \omega}(\boldsymbol{\sigma}) \rangle_{\omega}$ shows the average of $\Phi_{\alpha}(\boldsymbol{\sigma})$ over all clusters in orbit ω . In a nutshell, the correlation functions describe how atoms are arranged across the lattices, while the ECIs quantify how strongly those patterns contribute to the total energy of the chemically disordered systems.

Following the mathematical framework in Eqs. (11)–(13), a cluster expansion can be defined by how the interaction basis is chosen and fitted. In binary systems, the cluster expansion often reduces to an Ising-like representation with occupation variables analogous to $\{-1, 1\}$, whereas multicomponent and multi-sublattice systems require a larger set of orthogonal basis functions on each site, such as sinusoidal or indicator bases.^{127–130} Although the total number of possible configurations is enormous, the number of interaction terms that matter physically is often much smaller when the energetics are dominated by relatively local clusters, in particular if the fitting results respect the natural hierarchy from point terms to pairs, triplets, and higher-order atomic interactions.^{131–133} In principle, for a fixed parent lattice and a complete basis, cluster expansion is formally exact for representing on-lattice configurational energetics, but in practice it must be truncated and regularized to remain computationally and statistically tractable.¹²¹ Collectively, this formalism of cluster expansion highlights that its accurate and efficient construction is both

a physics problem and a regression problem: one must choose a parent lattice, define a tractable cluster space, build representative first-principles training structures, and eventually, fit a sparse, yet predictive Hamiltonian. Just as importantly, ensuring low fitting errors alone is not enough. A cluster expansion may predict training energies well but still yield incorrect thermodynamics if the low-energy motifs that dominate phase behaviors are not captured correctly, which is why ground-state-preserving fitting strategies can be crucial in configurational thermodynamics.¹³⁴

Practical use and considerations. Cluster expansion is most helpful when it is coupled with statistical sampling, as this combination converts a fitted lattice Hamiltonian into a vital tool for finite-temperature thermodynamics. Specifically, once the ECIs are known, the energy change associated with a trial configurational move can be evaluated very cheaply, making Monte Carlo sampling feasible over an extremely large number of atomic configurations. In canonical Monte Carlo, one proposes composition-conserving moves (such as swapping the species on two sites), computes the resulting energy change, and accepts the move with a probability^{15,135,136} (see Eq. (20) for details). In (semi-)grand-canonical sampling, the composition is allowed to vary under an imposed chemical potential, so the acceptance criterion also depends on the applied chemical potential and the corresponding change in particle number or species identity.^{137–140} This cluster expansion–Monte Carlo workflow has therefore become a standard route for predicting phase diagrams, order–disorder transformations, equilibrium long- and short-range orderings, and ion intercalation thermodynamics in diverse disordered solids.^{141–143} Although Monte Carlo is the most common companion technique, the same fitted Hamiltonians may also be analyzed using cluster-variation-type methods if a less computationally intensive treatment is sufficient.¹⁴⁴

The strength of cluster expansion is that it retains explicit configurational correlations while remaining much cheaper than direct first-principles sampling. As the sampled states are explicit microstates, rather than a single averaged medium, this method captures short-range order, local motif populations, ordering and clustering transitions, and composition-dependent connectivity trends that are outside the natural scope of effective-medium and mean-field theories.^{15,136,145,146} As an example, a recent cluster expansion–Monte Carlo study on entropy-stabilized oxides has shown that these chemically disordered materials can still retain measurable short-range order under synthesis-relevant conditions, even though increasing the chemical complexity suppresses the order–disorder transition and moves the structures closer to the ideal random limit¹⁴⁷ (Fig. 5a). Equally importantly, the fitted Hamiltonian remains strongly physically interpretable: pair terms often reflect nearest-neighbor preferences or aversions, while higher-order terms capture cooperative atomic motifs that cannot be directly reduced to pairwise interactions. For instance, recent cluster-decomposition analyses¹²³ have made model interpretability more quantitative by linking the fitted Hamiltonian to chemically meaningful local contributions. Collectively, these characteristics make cluster expansion especially useful for substitutional alloys, finite clusters,

nanoparticles, intercalation compounds, and other crystalline solid solutions that can be mapped cleanly onto well-defined parent lattices with only moderate local relaxation.^{84,124–126}

Ionic or chemically complex systems typically require additional care, as a short-range real-space cluster expansion may not capture long-range interactions efficiently enough on its own.⁸⁷ For instance, in multicomponent oxides,^{135,147} halide frameworks,¹⁴⁸ and multi-redox battery electrode materials,^{15,136,149} long-range Coulomb interactions, charge-balance constraints, and coupled cation–anion disorder can still remain essential even when the short-range chemistry is already represented reasonably well in cluster expansion. To address this challenge, a common extension is to augment the cluster expansion with an explicit electrostatic term ($E(\boldsymbol{\sigma})$):⁸⁷

$$E(\boldsymbol{\sigma}) = \sum_{\omega} m_{\omega} J_{\omega} \Pi_{\omega}(\boldsymbol{\sigma}) + \frac{E_0}{\epsilon_r} \quad (14)$$

where E_0 denotes the unscreened Coulomb energy from an Ewald summation based on nominal ionic charges, and ϵ_r is the effective dielectric constant. This electrostatically corrected cluster expansion has been especially useful for accurately modeling cation–anion short-range order,¹⁵⁰ heterovalent chemistry,¹⁵¹ and coupled vacancy ordering¹⁵² in complex disordered materials. Beyond improving energetic accuracy, this term also helps suppress highly charge-imbalanced and otherwise unphysical configurations during statistical sampling, keeping the configurational space under cluster-expansion-driven investigation more chemically meaningful. For example, in disordered rocksalt battery cathode materials, cluster-expansion-driven atomistic simulations have indicated that cation short-range order can strongly influence Li transport kinetics¹³⁶ (Fig. 5b). Additionally, charge-decorated, sparse lattice models combined with semi-grand-canonical cluster expansion–Monte Carlo can further infer Li-vacancy orderings, recover Li intercalation voltage profiles, and disentangle complex transition-metal and oxygen redox processes.¹⁵²

Broadly speaking, the core weaknesses of cluster expansion follow directly from its lattice-centered construction. Since cluster expansion is fundamentally based on on-lattice models, it is less reliable when disorder induces large off-lattice displacements, major coordination changes, defect formation, or strong local strain.^{48,121} Moreover, its complexity also grows rapidly with the number of components and candidate clusters, which makes basis selection, regularization, and training-set design increasingly crucial.^{129,152–154} Recent methodological advances have also introduced low-rank or tensor-factorized lattice models that can effectively compress interaction representations and strengthen the tractability of these approaches in chemically complex, high-dimensional configurational spaces.^{155–157} Moreover, long-range electrostatic interactions and elastic effects might converge slowly in a conventional real-space cluster expansion and require mixed-space treatments or auxiliary strain variables.^{158,159} In certain ionic materials, electronic degrees of freedom might not be fully separable from configurational disorder, which can limit the accuracy of a purely occupational Hamiltonian.¹⁶⁰ These issues do not remove the value of

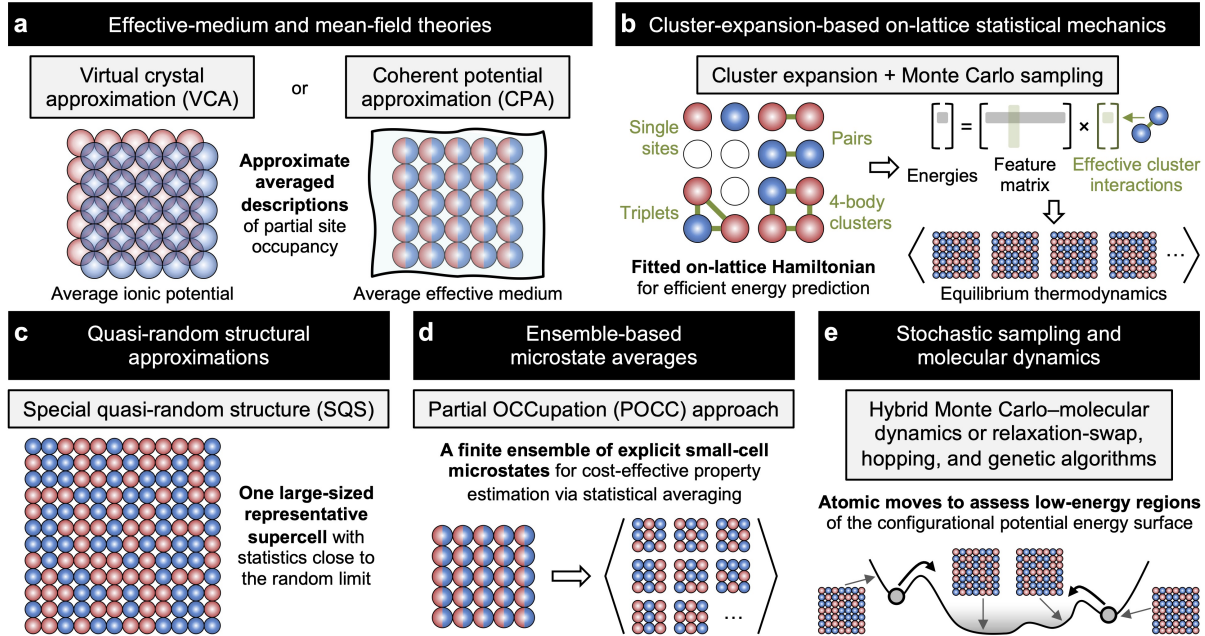


Fig. 4. Conceptual differences among classical atomistic simulation methods for modeling chemical disorder. (a) Effective-medium and mean-field theories (e.g., VCA and CPA) replace explicit disorder with a single averaged periodic medium that can be handled within a periodic electronic-structure simulation framework, trading atomistic details for computational efficiency. In VCA, constituent atoms are merged into an average ionic potential, whereas in CPA, disorder is represented through an effective medium that reproduces configurationally averaged scattering behaviors. These methods intentionally smooth out the local configurational fluctuations that exist in real disorder. (b) Cluster-expansion-based statistical mechanics retains configurational physics more explicitly by expressing the energy as a sum of effective atomistic interactions across single sites, pairs, triplets, and higher-order clusters. Once fitted, this lattice Hamiltonian can enable sampling (e.g., by Monte Carlo) to examine equilibrium thermodynamics, finite-temperature orderings, and short-range correlations across vast configurational ensembles. (c) Quasi-random structural approximations (e.g., SQS) represent disorder with one or a few representative supercells whose selected correlation functions approximate those of a fully random solid solution, allowing direct first-principles simulations without full ensemble sampling. (d) Ensemble-based microstate-average methods, illustrated by POCC, describe a disordered crystal as a finite statistical mixture of explicit ordered microstates, usually generated within a restricted cell size and fixed parent lattice. Observable properties are then obtained by averaging over this manageable set of symmetry-distinct configurations, providing an intermediate picture between single-structure approximations and extensive thermodynamic sampling. (e) Stochastic sampling and molecular dynamics probe the low-energy region of the configurational PES directly through atomic moves or dynamical trajectories. These approaches are valuable when disorder is accompanied by strong local relaxation, off-lattice distortions, or many nearly degenerate minima, such that the relevant disordered structures are better regarded as a collection of low-energy basins than as a single averaged crystal or an exhaustively enumerated ensemble. Red and blue spheres denote different chemical species.

cluster expansion, but they do define the range of systems for which it is most reliable.

Overall, cluster-expansion-based statistical mechanics provides a rigorous bridge between first-principles energetics and finite-temperature configurational thermodynamics. Its dominant advantage over effective-medium and mean-field theories is that it keeps explicit configurations and their correlations, which allows it to describe ordering physics with much greater detail and interpretability. Its central cost is that one must first build and validate a reliable, accurate lattice Hamiltonian, and this requirement becomes even more demanding for disordered solids with strong relaxation, long-range interactions, or high chemical complexity. These central strengths and weaknesses explain why cluster expansion remains one of the most powerful computational frameworks for chemical disorder, but also why one may sometimes leverage simpler modeling strategies when full configurational sampling is unnecessary or impractical.

2.3 Quasi-random structural approximations

Quasi-random structural approximations take a different route from the two methods discussed above. Effective-medium and mean-field strategies, such as VCA and CPA, replace a disordered crystal with an averaged medium, whereas cluster-expansion-based statistical mechanics builds an effective Hamiltonian and samples many configurations to recover equilibrium behaviors. In contrast, quasi-random structural approximations replace the full configurational ensemble with one (or a few) carefully chosen periodic supercells, whose local statistics mimic the disordered state (Fig. 4c). In this sense, they are representative-structure approaches: they retain an explicit atomistic lattice in first-principles simulations, but avoid full thermodynamic sampling.

Special quasi-random structure (SQS) method. The best-known approximation is the SQS approach. The key idea of SQS is to construct a supercell whose low-order correlation functions match those of an infinite random solution as closely as possible at a fixed composition. Notably, the original SQS demonstrations have shown that even small supercells can capture the first few physically important correlations of random alloys far better than a naive random occupation of the same cell.^{88,89} Once these supercells are created, they can be directly used in standard DFT simulation workflows as explicit structural models of the disordered phase.

The foundations of SQS are relevant to the cluster-correlation language in cluster expansion, while the goal is different. SQS uses the orbit-averaged correlation functions $\Pi_\omega(\boldsymbol{\sigma})$ and cluster basis functions $\Phi_\alpha(\boldsymbol{\sigma})$ in Eqs. (12) and (13), but they are leveraged to identify supercells whose correlations best reproduce those of the target disordered state. In a perfectly random alloy, the desired value of this correlation is characterized by the ensemble average ($\bar{\Pi}_\omega^{\text{rand}}$):

$$\bar{\Pi}_\omega^{\text{rand}} = \sum_{\boldsymbol{\sigma}} P_{\text{rand}}(\boldsymbol{\sigma}) \Pi_\omega(\boldsymbol{\sigma}) \quad (15)$$

where $P_{\text{rand}}(\boldsymbol{\sigma})$ is the probability of the configuration $\boldsymbol{\sigma}$ in this random ensemble. Specifically, for a binary alloy with occupation variables $\sigma_i \in \{-1, +1\}$, this target becomes:

$$\bar{\Pi}_{\omega}^{\text{rand}} = (2x - 1)^{|\omega|} \quad (16)$$

where x denotes the concentration of the $+1$ species, and $|\omega|$ represents the number of sites in the cluster. At equimolar composition ($x = 0.5$), a perfectly random binary alloy exhibits zero average correlations for all single-site clusters, pairs, triplets, and higher-order clusters.^{88,89}

Viewed this way, the SQS construction becomes a finite-cell optimization problem. Among all configurations compatible with a chosen composition and supercell size, the algorithm seeks the structure whose correlation vector is closest to the target vector over a selected set of cluster orbits \mathcal{O} . A common objective function ($\mathcal{E}_{\text{SQS}}(\boldsymbol{\sigma})$) for this optimization task is:

$$\mathcal{E}_{\text{SQS}}(\boldsymbol{\sigma}) = \sum_{\omega \in \mathcal{O}} w_{\omega} \left[\Pi_{\omega}(\boldsymbol{\sigma}) - \bar{\Pi}_{\omega}^{\text{target}} \right]^2 \quad (17)$$

where w_{ω} is the weight assigned to orbit ω , and $\bar{\Pi}_{\omega}^{\text{target}}$ shows the target correlation for the orbit. This weighted squared-deviation form in Eq. (17) offers a convenient generic representation of the underlying optimization task to capture the correlation-matching spirit of SQS,^{88,89} although many recent implementations have introduced alternative objective functions, including criteria that focus on either prioritizing exact matching of the maximum number of target correlations¹⁶¹ or explicitly balancing correlation accuracy against DFT cost.¹⁶² Thus, while SQS borrows the correlation language of cluster expansion, it does not fit interaction coefficients or construct an effective Hamiltonian. Instead, the correlations are used only to build representative structures. Hence, SQS is not random in a literal sense, but rather the periodic configuration whose selected low-order statistics best approximate the target disordered ensemble within a finite supercell.

The main appeal of SQS is that it converts disorder into one or a few explicit supercells that can be used directly in first-principles DFT simulations. As SQS supercells can be relaxed, local lattice distortions¹⁶³ and charge redistribution¹⁶⁴ can emerge naturally, making SQS much more realistic than averaged-medium approaches for various structural and electronic problems. This practical advantage explains why SQS has been applied successfully across a massive range of materials systems. The correlation matching also allows SQS to outperform an arbitrary random supercell of the same size, as it reduces finite-size artifacts that may otherwise arise from small periodic cells. Classical work has shown the usefulness of SQS for metallic alloys^{88,89,163,164} and ceramic solid solutions.¹⁶⁵ More recent studies on high-entropy alloys continue to treat SQS as one of the most practical DFT-ready structural models, particularly when the key objective is to capture local-environment effects, rather than exact finite-temperature thermodynamics.^{166–168} Moreover, the broad use of SQS has been supported by steady advances in structure generation. Modern implementations typically search in the discrete configurational space using stochastic

optimization, systematic enumeration, or hybrids of the two. A practical consequence is that, as the number of components and relevant pair or multi-site correlations increases, accurate SQS models require larger supercells, which raises DFT cost. A widely used implementation is the `mcSQS` package¹⁶¹ within the alloy theoretic automated toolkit (ATAT),⁸⁵ which can search for supercells that exactly match as many target correlations as possible, while optimizing the shape and atomic occupations of these supercells using a well-established multi-sublattice framework. Representative modern toolchains also include newer ecosystems, such as the integrated cluster expansion toolkit (ICET),⁸⁶ as well as reproducible workflow layers (e.g., SimplySQS).¹⁶⁹ With tools such as ATAT and ICET, SQS has become a practical and broadly used approximation for assessing the phase stability and functional properties of chemically disordered solids.^{170,171}

At the same time, the same simplification that offers SQS its practical power also defines its limitations. As one or a few supercells are used to substitute a full ensemble, conventional SQS does not by itself provide configurational entropy, temperature-dependent short-range order, or the distribution of fluctuations across many microstates.^{172,173} SQS is therefore best viewed as a practical structural approximation to a chosen disordered state, rather than as a complete theory of disorder. In practice, it works best when the physically relevant disordered state is close to the ideal random limit. The reliability of SQS decreases significantly when this ideal random state is no longer the physically relevant target, especially in systems where long-range electrostatics or strong local chemical preferences drive substantial short-range order.¹⁷⁴ For instance, related difficulties have been increasingly observed in cation-disordered rocksalt materials, where local ordering, electrostatics, and relaxation effects are strongly coupled.⁶⁶ Such limitations motivate future quasi-random approximations to target non-random local correlations more explicitly.

Relevant quasi-random approximations. The SQS idea can be extended naturally when the physically relevant disordered state is not perfectly random. Instead of matching the correlation functions of an ideal random alloy, one can construct a representative supercell that matches the correlation functions of a short-range-ordered state. This task can be achieved using the special quasi-ordered structure (SQoS) approach, where the short-range-order correlations are obtained from Monte Carlo simulations on a DFT-based cluster expansion model, and the SQoS method further constructs DFT-manageable supercells whose correlations approximate these ensemble-averaged short-range-order states.¹⁷⁵ More generally, this example shows that cluster expansion and Monte Carlo can be used to determine the equilibrium correlation pattern, whereas a short-range-order-targeted representative structure (such as SQoS) provides one explicit configuration that approximates it for detailed first-principles calculations. Furthermore, a related but distinct framework is the supercell random approximate (SCRAP), introduced for accelerated modeling of high-entropy alloys.⁹¹ Similar to SQS, SCRAP replaces the full configurational ensemble by an optimized explicit supercell. However, this new method is formulated around target one-site

and pair probabilities and uses a hybrid cuckoo-search strategy to explore large compositional and ordering spaces efficiently (Fig. 5c). By design, SCRAP can target non-random short-range order as well as the fully random limit, so it is best regarded as a broader relative of SQS, rather than simply another implementation. Broadly speaking, these methods tackle the key weakness of conventional SQS. Their limitation, however, is that the target correlations must come from elsewhere, e.g., an experiment or another thermodynamic model, so they do not actually remove the need for statistical mechanics when the goal is to determine the equilibrium state itself.

Taken together, these quasi-random approximations occupy an intermediate regime between averaged-medium descriptions and full statistical-mechanics sampling. Traditional SQS is most effective when the relevant disordered states are close to the ideal random limit, while beyond-random variants such as SQoS and SCRAP extend the same representative-supercell concept to systems with significant short-range order. Their main advantage is that they retain explicit local environments in a DFT-manageable form, whereas their main limitation is that they approximate a chosen disorder state rather than derive the full equilibrium ensemble. In addition, as they are ultimately static approximations, finite-temperature properties still require additional treatment, e.g., via phonon calculations, molecular dynamics, or Monte Carlo sampling built on top of the representative structures. For these reasons, these static quasi-random structural approximations are generally most valuable as baseline models of random disorder, representative structures for first-principles calculations, or inputs to more complete finite-temperature frameworks.

2.4 Ensemble-based microstate averages

Ensemble-based microstate-average methods describe a chemically disordered crystal as a finite statistical mixture of various explicit ordered configurations, which makes them fundamentally distinct from the three strategies discussed above. In effective-medium and mean-field methods, disorder is replaced by an averaged environment, so specific local arrangements are not modeled explicitly. In cluster expansion, the core object is a fitted effective Hamiltonian, which is further sampled across a large configurational space. In SQS, disorder is approximated by one or a few specially designed supercells that reproduce selected correlation functions of random alloys. In contrast, ensemble-based methods begin by choosing a finite set of explicit microstates that all satisfy the target composition and parent lattice, and then recover observables by averaging over this set. The central approximation is thus that, instead of treating the full (and usually massive) possibilities of local atomic arrangements, these ensemble-based approaches average over only a computationally manageable subset of representative configurations (Fig. 4d). In this context, they can be viewed as a middle ground between SQS and cluster expansion: they retain explicit atomistic configurations like SQS, but estimate properties from statistical averages over multiple configurations, as in cluster-expansion-based statistical mechanics.

General framework. The formalism is straightforward. Let s_i denote microstate i , meaning one fully occupied ordered configuration consistent with the target composition. Moreover, let g_i be the configurational degeneracy of such a microstate. $F_i(T)$ is its free energy at temperature T . Then, the probability of microstate i within the chosen ensemble ($P_i(T)$) is:

$$P_i(T) = \frac{g_i \exp[-\beta F_i(T)]}{\sum_j g_j \exp[-\beta F_j(T)]} \quad (18)$$

where $\beta = 1/(k_B T)$, k_B is the Boltzmann constant, and the denominator is the partition function of the finite ensemble. Any observable A can then be estimated as:

$$\langle A \rangle_T = \sum_i P_i(T) A_i \quad (19)$$

where A_i represents the value of this observable for microstate i . In the simplest case, $F_i(T)$ is approximated by the relaxed DFT energy (or enthalpy) of this microstate, although vibrational, magnetic, or electronic contributions can be further added when necessary. An early conceptual foundation for this category of methods rests on formulating symmetry-adapted configurational modeling in a reduced space of independent site-occupancy configurations, while keeping their degeneracy explicit.^{176,177} In practice, the central task becomes how to construct the finite set of microstates in a way that is both computationally feasible and physically representative. Hence, the main approximation in these ensemble-based microstate-average methods does not lie in the statistical-mechanics formalism itself, but in replacing the immense number of possible atomic arrangements with a manageable finite ensemble of representative microstates.

Partial OCCupation (POCC) formalism. The best-known realization of the finite-ensemble microstate-average concept is the POCC approach⁹⁰ used in AFLOW high-throughput atomistic simulation workflows.⁹⁶ With this approach, a partially occupied structure is mapped to a set of ordered derivative supercells that reproduce the target composition as closely as possible within a chosen finite cell size, following the broader logic of combinatorial supercell construction for atomic substitutions.^{90,178} Symmetry is further used to identify the distinct microstates, and only symmetry-inequivalent configurations are retained explicitly, with multiplicities restored via the degeneracy factors g_i . After the energies and other properties of these microstates are computed, ensemble averages are obtained from their statistical weights. Representative applications have shown that POCC can be applied not only to describe partial occupancy itself, but also to derive disorder-aware descriptors for driving the discovery of chemically complex solids (Fig. 5d). For instance, POCC configurational energy distributions from ordered microstates have been used to uncover synthesizable single-phase high-entropy carbides¹⁷⁹ and later extended into disordered enthalpy–entropy descriptors to facilitate broader high-entropy ceramics discovery.¹⁸⁰

This explicit-supercell strategy is powerful because it retains real-space local environments and enables direct averaging of diverse properties, but it is also costly because many microstates must be computed explicitly. Every member of the ensemble is a standard crystal structure with full site occupancies. Thus, standard first-principles workflows can be applied directly without modifying the underlying electronic-structure method. As each microstate can also be computed independently, these workflows are naturally parallel. This makes the method especially useful when one wants to evaluate ensemble-averaged properties beyond total energies, such as lattice dynamics,¹⁸¹ optical response,¹⁸² and thermal expansion behaviors.¹⁸³ Notably, a useful way to view its relation to SQS is that an SQS can be regarded as one member of a larger configurational ensemble. SQS is designed to mimic the random limit with one carefully chosen structure, while ensemble averaging allows the relative importance of different atomic configurations to change with temperature via their Boltzmann weights. This finite-temperature flexibility is particularly essential in chemically complex ceramics, where disorder can strongly affect phase stability and vibrational properties.¹⁸⁴ Nonetheless, the trade-off is that the number of distinct configurations that are expected to be computed grows rapidly with cell size and chemical complexity. Hence, the POCC approach remains constrained by finite supercell size and computational cost.

Relevant finite-ensemble approaches. Recent studies have further broadened the category of finite-ensemble microstate-average approaches beyond canonical POCC, while maintaining the same central idea: a chemically disordered crystal can be approximated as a weighted collection of explicit microstates. Some methods replace exhaustive enumeration with random or targeted sampling, which can make microstate averaging more practical for chemically complex systems while preserving this ensemble-averaging logic.^{185–189} Ensemble-based averaging has also been leveraged to reproduce local-environment-sensitive spectroscopic observables, where signals of nuclear magnetic resonance are modeled by summing the contributions from multiple ordered microstates.¹⁹⁰ Moreover, a particularly succinct example has been shown for multicomponent double perovskite oxides (Fig. 5e), where the distribution for the DFT-derived energies of only six symmetrically distinct small-cell cation-ordered prototypes is sufficient to accurately predict the experimental likelihood of long-range B-site cation disorder across a massive compositional space.³ Taken together, these examples highlight the vast diversity of finite-ensemble strategies that complement POCC for different materials classes, observables, and computational scales.

Overall, these microstate-average approaches occupy a valuable middle ground in chemical disorder modeling. They are more physically explicit than mean-field methods as they examine local environments directly, more flexible than SQS as they average over multiple configurations rather than just one, and typically simpler than cluster expansion as they avoid fitting an effective Hamiltonian. Their main strength is generality: in principle, any property that can be computed for an ordered microstate can be averaged across the ensemble afterward. Nonetheless, they are

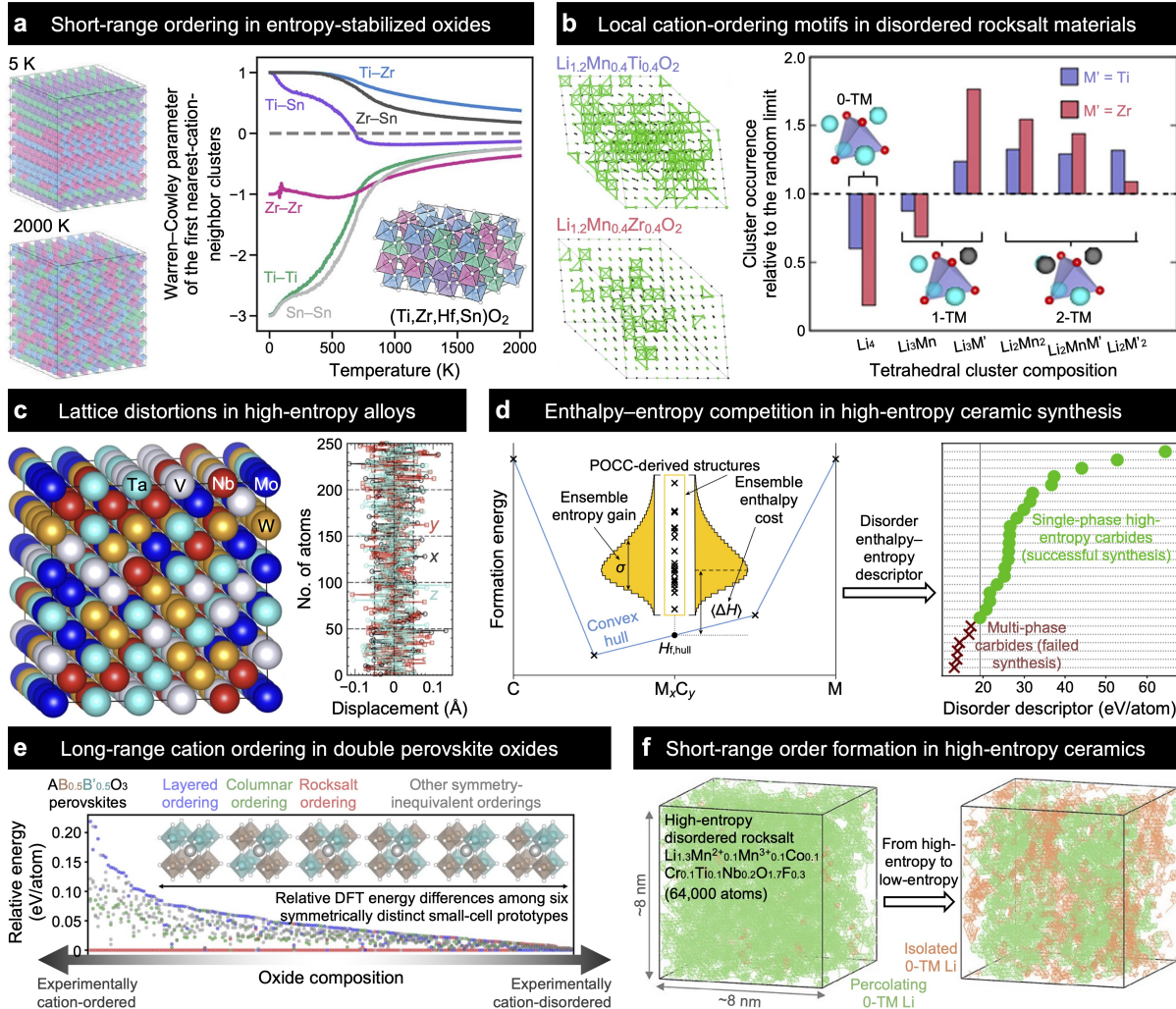


Fig. 5. Representative applications of classical atomistic simulation methods for modeling chemical disorder. (a) Cluster expansion–Monte Carlo can reveal persistent chemical short-range ordering in entropy-stabilized oxides at elevated temperatures.¹⁴⁷ (b) In disordered rocksalts, cluster-expansion-based Monte Carlo simulations quantify local motifs that can affect Li transport, where 0-transition-metal-neighbored (0-TM) tetrahedral channels for facile Li ion migration are highlighted by green bonds.¹³⁶ (c) A SCRAP-optimized 250-atom supercell for an equimolar TaNbMoWV random solid solution shows no short-range order in the first three nearest-neighbor shells, exhibiting local heterogeneity in lattice distortions.⁹¹ (d) A finite set of POCC-derived ordered crystal structures can give rise to a distribution of formation energies around the convex hull, from which a disorder enthalpy–entropy descriptor can be constructed to rationalize and screen whether multicomponent ceramic syntheses are likely to lead to single-phase high-entropy products or instead decompose into multi-phase mixtures.¹⁸⁰ (e) A compact finite ensemble of six B-site ordering prototypes is sufficient to predict experimental long-range cation order vs. disorder in $A_2BB'O_6$ double perovskite oxides across a massive chemical space.³ (f) Stochastic relaxation-swap sampling drives initially random high-entropy ceramic structures toward lower-energy short-range-ordered states, leading to the emergence of critical isolated 0-TM channels that can significantly influence long-range Li ion transport.¹⁹¹ Panel (a) adapted with permission from ref.¹⁴⁷, copyrighted by the American Chemical Society. Panels (b), (d), and (e) adapted from ref.¹³⁶, ref.¹⁸⁰, and ref.³, respectively, CC BY 4.0. Panel (c) adapted with permission from ref.⁹¹, copyrighted by Springer Nature. Panel (f) adapted with permission from ref.¹⁹¹, copyrighted by John Wiley and Sons.

limited by combinatorial growth: as the number of components, partially occupied sublattices, or relevant correlation lengths increases, the explicit ensemble needs to be truncated or sampled approximately, and the final result depends on whether the retained microstates still capture the key local physics of chemical disorder. Thus, these methods are often best viewed as controlled finite-ensemble approximations, rather than exact descriptions of the thermodynamic limit.

2.5 Stochastic sampling and molecular dynamics

Stochastic sampling and molecular-dynamics-based methods become particularly helpful when chemical disorder cannot be described adequately by any single one of the atomistic simulation frameworks discussed earlier (Table 1). Notably, in cluster expansion, Monte Carlo mainly acts as a statistical-mechanics solver for a pre-fitted lattice-model Hamiltonian. Additionally, quasi-random structural approximations (e.g., SQS) work by compressing complex chemical disorder into one or a few representative supercells, while ensemble-based methods (e.g., POCC) instead average over the full set of symmetry-distinct microstates within a limited cell size. By contrast, the present category of methods explores the low-energy region of the configurational potential energy surface (PES) more directly through stochastic moves or dynamical trajectories, without requiring either a pre-fitted lattice model, representative supercell configurations, or exhaustive enumeration of the entire small-cell ensemble. This perspective is especially useful in modeling chemically disordered materials showing large local structural relaxation, off-lattice distortions, or many nearly degenerate configurations, where the statistically important atomic structures are often best viewed as a subset of low-energy basins on a rough PES landscape (Fig. 4e). For this reason, purely random configurational sampling is usually inefficient for chemically disordered materials. The number of possible occupational arrangements grows combinatorially, while the statistically essential low-energy configurations occupy only a small fraction of the overall PES, particularly when local relaxation is strong. Random structures are thus usually more helpful as initial seeds or reference configurations than as the primary means of sampling disorder.

Direct Monte Carlo sampling. Direct sampling using Monte Carlo is a natural starting point, as it generates a Markov chain whose long-time distribution approaches the target ensemble. In the standard Metropolis scheme, a trial configuration is accepted with probability (P_{acc}):

$$P_{\text{acc}} = \min [1, \exp(-\beta\Delta E)] \quad (20)$$

where $\beta = 1/(k_{\text{B}}T)$, k_{B} is the Boltzmann constant, T is the temperature, and $\Delta E = E_{\text{new}} - E_{\text{old}}$ is the energy change between the trial and current states. For chemically disordered solids, this trial move may involve a species swap, vacancy motion, a change in site occupancy, or a coupled occupational–displacive update.^{49,192–194} For example, DFT-based Metropolis Monte Carlo has

been combined with full structural relaxation after each swap to reveal pronounced short-range order in SiSn alloys.¹⁹⁵ Moreover, a Monte Carlo framework with selective atom swapping and repeated relaxation has been used to predict the order-to-disorder transitions in multicomponent MXenes.¹⁹⁶ The main benefit of this approach is that it targets equilibrium statistics without first reducing the problem to a fitted effective Hamiltonian. However, this method can be inefficient when each atomic move must be evaluated on a rugged, continuously relaxing PES.

Enhanced Monte Carlo strategies. Various enhanced Monte Carlo methods can improve on plain Metropolis sampling by helping the system cross barriers more efficiently. As an example, simulated annealing gradually lowers the temperature parameter in Monte Carlo simulations so that the search first explores broadly and then concentrates on lower-energy regions.¹⁹⁷ Replica-exchange Monte Carlo (i.e., parallel tempering) runs multiple replicas at different temperatures and swaps them occasionally, which allows low-temperature trajectories to benefit from barrier crossing at higher temperatures.^{198–200} These approaches remain close to Boltzmann sampling, but they differ in cost: simulated annealing is simple and widely used, whereas replica exchange is better suited to rugged PES landscapes at the price of running multiple replicas.

Hybrid Monte Carlo–molecular dynamics methods. Molecular dynamics can complement Monte Carlo by evolving atoms continuously on their PES landscape and thus capturing thermal motion, anharmonicity, and local structural relaxation naturally. This approach is essential when the energy depends not only on what species occupy which sites, but equally importantly on how the surrounding lattice responds. Nevertheless, direct molecular dynamics is usually inefficient for equilibrating substitutional disorder because changes in site occupancy are rare on accessible simulation time scales.²⁰¹ Fortunately, hybrid Monte Carlo–molecular dynamics methods tackle this mismatch by coupling discrete chemical updates with continuous relaxation, e.g., by adding short molecular dynamics segments between Monte Carlo moves.²⁰² This coupling is physically well motivated as occupational variables are typically slow and activated, while local positional relaxation is much faster, enabling Monte Carlo to update the chemical states of atomic motifs, whereas molecular dynamics can re-equilibrate the surrounding structural basin. For instance, a hybrid Monte Carlo–molecular dynamics approach has been developed to examine how boron and carbon interstitials drive distinct short-range-ordered motifs in Inconel-type superalloys.²⁰³ In the most rigorous formulation, a trajectory of molecular dynamics can be used as a proposal move and coupled with a Metropolis correction to recover the target ensemble exactly, whereas many materials-oriented implementations instead apply short segments of molecular dynamics more pragmatically to relax atomic positions between occupational updates using Monte Carlo. These schemes are well-suited to disordered materials in which the energetic cost of a chemical rearrangement depends strongly on local distortion, including systems with large size mismatch,

heterovalent substitution, or soft structural modes. However, because each occupational update must still be coupled to explicit dynamical relaxation, hybrid Monte Carlo–molecular dynamics schemes can remain computationally expensive and may still struggle to navigate highly rugged PES landscapes efficiently, motivating the more aggressive search strategies discussed next.

Relaxation-swap methods. Relaxation-swap approaches can push the logic of hybrid Monte Carlo–molecular dynamics further through replacing finite-temperature segments of molecular dynamics simulations with direct structural relaxation of each altered configuration.²⁰⁴ Starting from an occupational state σ_{n-1}^* and relaxed coordinates \mathbf{R}_{n-1}^* , such approaches propose a new occupational state σ'_n and obtain the corresponding relaxed structure (\mathbf{R}'_n) from:

$$\mathbf{R}'_n = \underset{\mathbf{R}}{\operatorname{argmin}} U(\sigma'_n, \mathbf{R}) \quad (21)$$

where $U(\sigma, \mathbf{R})$ represents the potential energy as a function of occupational state σ and atomic coordinates \mathbf{R} . The move is then evaluated using the relaxed energy difference (ΔE_n):

$$\Delta E_n = U(\sigma'_n, \mathbf{R}'_n) - U(\sigma_{n-1}^*, \mathbf{R}_{n-1}^*) \quad (22)$$

which can be subsequently accepted or rejected by designing a criterion based on ΔE_n . Notably, this strategy can be particularly beneficial when local relaxation contributes substantially to the energetics of chemical disorder. By relaxing altered configurations before comparing energies, these methods can avoid the low acceptance rates that can arise if strained, unrelaxed structures are evaluated directly. Crucially, a practical modern example is the short-range order swapping method, which uses descriptor-guided atom swaps, feature selection, and Bayesian optimization to construct atomistic structural models efficiently from initially random crystal lattices, thereby providing a strongly practical heuristic alternative to costly explicit thermodynamic sampling¹⁹¹ (Fig. 5f). Nevertheless, the thermodynamic meaning of these relaxation-swap strategies should be stated carefully: they sample relaxed inherent structures, rather than exploring the full finite-temperature vibrational ensemble. Therefore, the central value of such relaxation-swap methods is in identifying statistically important low-energy local structural motifs efficiently.

Basin-hopping and minima-hopping methods. These two types of hopping methods should be better regarded as landscape-exploration tools than as exact ensemble samplers. Specifically, basin-hopping perturbs the lattice structure and then immediately relaxes it, converting the PES into a network of local minima and jumps between basins.²⁰⁵ As an example, a basin-hopping scheme for multi-cation perovskites has been established to identify low-energy cation-ordering patterns more efficiently than cluster-expansion-based modeling.²⁰⁶ Moreover, minima-hopping combines short escape trajectories from molecular dynamics with local relaxation to search for

new low-energy minima efficiently.^{207,208} These methods are especially helpful when positional relaxation is as important as site occupancy, as they do not require a fixed-lattice representation. However, because these methods prioritize efficient discovery of low-energy minima rather than rigorous thermodynamic weighting, they do not directly result in equilibrium ensemble averages and can also be too sensitive to the design of the perturbation or escape moves.

Genetic and evolutionary algorithms. Genetic algorithms and evolutionary methods address the same low-energy search problem from a population perspective by evolving many candidate configurations simultaneously. Candidate structures are selected according to a fitness measure and combined via crossover and mutation to produce new populations.²⁰⁹ For instance, a genetic algorithm has been used to predict stable chemical orderings in bimetallic nanoparticles across a broad size, shape, and compositional space of FePt nanoparticles.²¹⁰ The primary advantage of these approaches is that they can assess multiple competing low-energy basins at once, which is helpful for chemically disordered materials with many nearly degenerate occupational patterns. Symmetry-adapted crossover schemes and more recent hybrids that incorporate Metropolis-like acceptance rules have further improved their efficiency and statistical relevance.^{211,212} However, these algorithms can be computationally demanding because many candidate structures must be evaluated simultaneously. In addition, the convergence of evolutionary approaches may depend sensitively on their representation, fitness function, and crossover or mutation operators.

Overall, these atomistic modeling approaches span a continuum from equilibrium sampling to low-energy exploration of PES landscapes. Direct and replica-exchange Monte Carlo, as well as hybrid Monte Carlo–molecular dynamics methods, remain closest to statistical mechanics in the strict sense, whereas relaxation-swap, hopping, and genetic algorithms are most effective as tools for locating the low-energy configurations that dominate disordered material behaviors. In practice, their usefulness depends strongly on access to fast, accurate energy prediction models, which is why they have become substantially more powerful when coupled with modern MLIPs and relevant surrogate Hamiltonians.^{58,64,213,214} Their practical reach has been expanded further by large-scale parallel computing and implementations with graphics processing units (GPUs). For example, the recently proposed SMC-X method exploits generalized checkerboard updates on accelerator hardware to push Monte Carlo on chemically complex metallic alloys to billion-atom scales.^{215,216} Moreover, PyHEA combines GPU-accelerated Monte Carlo with global and local search strategies to boost short-range-order simulations in high-entropy alloys.²¹⁷ Looking further ahead, although quantum computing remains at an early stage, recent work suggests that quantum annealing may offer a complementary route for sampling thermodynamically relevant low-energy atomic configurations within chemically disordered materials.²¹⁸

2.6 Macroscopic thermodynamic models

In distinction to atomistic simulation approaches, macroscopic thermodynamic models describe chemical disorder at the macroscopic phase level rather than with explicit atomic configurations. Instead of enumerating countless microstates and averaging over them, these methods represent each disordered phase directly by its free energy (or other important thermodynamic properties) as a function of temperature, pressure, and composition. Therefore, they are most valuable when the main goal is to predict phase boundaries, chemical potentials, and synthesis windows, rather than to understand and optimize the exact atomic motifs within a disordered structure.

Simplified thermodynamic screening descriptors. The simplest macroscopic approach is to leverage the same enthalpy–entropy competition introduced earlier in Eqs. (1)–(3), but apply it mainly as a screening tool rather than as a full phase-equilibria model. In this picture, disorder is favored when the entropic stabilization is large enough to offset the enthalpic penalty of mixing. Typical implementations fall into two related forms. Some retain an explicit but simplified free-energy model by coupling ideal configurational entropy with approximate mixing enthalpies to screen random solid solutions against competing ordered phases. As an example, DFT-derived binary interaction parameters have been combined with the regular solution model to unveil new compositions likely to stabilize single-phase high-entropy alloys across the periodic table.²¹⁹ In addition, other approaches move one step further toward large-scale screening by replacing one or both thermodynamic terms with more empirical but still physically motivated descriptors for order–disorder tendency or synthesizability.^{37,56,57} Related descriptor ideas can also be extracted from explicit microstate ensembles, providing a useful bridge to the ensemble-based approaches discussed earlier, e.g., for driving computational discovery of high-entropy ceramics.^{179,180}

These simplified methods are attractive because their speed, interpretability, and ease of use make them powerful tools for screening broad disorder trends across large chemical spaces, but these simplifications are also their central weaknesses because they limit thermodynamic rigor. By relying on a small number of physically meaningful quantities, they can quickly distinguish general tendencies toward random solid solutions, ordered compounds, or phase separation and are therefore especially helpful for high-throughput studies of high-entropy alloys and ceramics without requiring a full thermodynamic database.^{37,56,57,219} Nonetheless, since they are not full free-energy models, they often rely on ideal (or near-ideal) entropy expressions, coarse enthalpy estimates, or empirical decision boundaries. Furthermore, they usually do not enforce full phase coexistence, mass balance across multiple competing phases, or detailed sublattice chemistries. Thus, they are fast screening tools, rather than full substitutes for phase-equilibria modeling.

CALculation of PHase Diagrams (CALPHAD). CALPHAD⁸³ has long been known as an established macroscopic framework for modeling chemical disorder. In CALPHAD, each phase is assigned a parameterized Gibbs free-energy model whose form describes the relevant physics of that phase, such as substitution on one or more sublattices, vacancies, magnetic ordering, and non-stoichiometry. At fixed temperature T , pressure p , and overall composition, equilibrium is obtained by minimizing the total Gibbs free energy of the multicomponent system (G_{sys}):

$$G_{\text{sys}} = \sum_{\phi} n_{\phi} G^{\phi}(T, p, \{y_i^{\phi}\}) \quad (23)$$

where ϕ labels the phases present, n_{ϕ} denotes the amount of phase ϕ , G^{ϕ} shows the molar Gibbs free energy of phase ϕ , and y_i^{ϕ} is the composition or site-fraction variables in this phase model. For substitutional solutions, CALPHAD follows exactly the same free-energy logic as Eq. (2), but it further extends it into a flexible phase-modeling framework.²²⁰ In practice, the free energy of each phase is described as a sum of reference-state terms, configurational entropy terms, and non-ideal interaction terms, often using Redlich–Kister expressions for substitutional solutions and compound-energy or sublattice formalisms for ordered, ionic, or non-stoichiometric phases. The model parameters are further examined against diverse inputs, including phase boundaries, activities, calorimetry, order–disorder transition temperatures, and selected first-principles data. During database assessment, these parameters are optimized such that a single set of free-energy functions is able to reproduce the heterogeneous inputs as consistently as possible. At the same time, this assessment preserves the topology of binary, ternary, and higher-order phase relations. For instance, a CALPHAD sublattice description of the Al–Ni system has been created to model its A1-to-L1₂ order–disorder transition via an entirely phase-level, non-atomistic framework.²²¹ Thus, CALPHAD differs formally from atomistic modeling methods, such as cluster expansion, SQS, and Monte Carlo sampling. CALPHAD is a top-down description that starts from phase-level free-energy functions and determines equilibrium by thermodynamic minimization, while atomistic methods are bottom-up descriptions that start from explicit configurations and recover thermodynamics of chemical disorder by statistical averaging over microscopic states.

The crucial strength of conventional CALPHAD is that it converts diverse experimental and computational inputs into a thermodynamically self-consistent free-energy framework that can be applied efficiently, but this coarse-grained treatment is also its key limitation, as it sacrifices direct microscopic details.²²⁰ Once a database has been built, CALPHAD can rapidly compute phase diagrams and fractions, chemical potentials, partitioning trends, and their thermodynamic driving forces across broad compositional and temperature spaces, which is why it has become a dominant tool for developing multicomponent alloys and ceramics with well-defined lattices. CALPHAD can also incorporate magnetic, vibrational, and electronic free-energy contributions via semi-empirical but thermodynamically consistent expressions, which are often cumbersome

to assess in traditional atomistic workflows, e.g., cluster-expansion-based statistical mechanics. Its flexibility is further showcased by compound-energy and sublattice formalisms, which allow partial ordering, vacancies, non-stoichiometry, and substitutions to be described within a unified Gibbs free-energy framework. However, because conventional CALPHAD represents disorder mainly at the phase and mean-field levels, it cannot explicitly resolve local atomic arrangements, short-range order, or site-specific electronic structure. Its interaction parameters should thus be interpreted as effective thermodynamic descriptors, rather than direct microscopic interactions. As a result, the predictive reliability of pure CALPHAD methods depends heavily on the quality and transferability of the underlying assessment, particularly in chemically complex systems or poorly characterized compositional spaces. In addition, database development is labor-intensive as the phase models must be selected carefully, while assessments across binaries, ternaries, and higher-order systems must remain mutually consistent. Overall, these strengths and weaknesses are exactly why CALPHAD remains indispensable for efficient phase-level prediction, yet also why it needs to be extended to further recover the missing local configurational physics.

Recent developments have extended CALPHAD in two critical directions. Specifically, one direction boosts CALPHAD by incorporating more realistic configurational statistics, allowing short-range ordering to be treated more explicitly than in conventional mean-field descriptions. For example, the cluster variation method has recently been combined with CALPHAD and the Fowler–Yang–Li transform to enable a more practical thermodynamic framework with intrinsic chemical short-range order.¹⁴⁴ The other direction couples CALPHAD with atomistic modeling of chemical disorder, where atomistic simulations offer mixing enthalpies, ordering tendencies, and finite-temperature corrections, while CALPHAD further translates these inputs into phase-diagram-ready thermodynamic functions. Modern tools, such as ATAT,⁸⁵ offer a practical route for mapping first-principles calculations of atomistic energies onto CALPHAD thermodynamic models in high-throughput workflows.²²² In addition, for high-entropy alloys, cluster expansion has been coupled with a mean-field statistical-mechanics model and DFT energies to infer solid-solution transition temperatures,²²³ highlighting how atomistically assessed disorder energetics can be transformed into CALPHAD-driven hierarchical screening of multicomponent materials. Taken together, these developments further establish CALPHAD as an integration layer between microscopic energetics and engineering-scale thermodynamic prediction—an essential role that is becoming even more important, as MLIPs and other AI tools are increasingly being leveraged as fast upstream engines for thermodynamic assessments of chemical disorder.^{224–227}

3. Modern AI-assisted approaches for disorder modeling

Modern AI-assisted approaches for modeling chemically disordered materials are generally best regarded not as replacements for classical statistical mechanics, but as a new, complementary

set of data-driven tools for boosting the scale, fidelity, efficiency, and transferability with which disordered configurational ensembles are represented, sampled, and interpreted. The task is the same: chemical disorder is determined by a massive set of symmetry-inequivalent occupational microstates whose relative populations depend collectively on energy, entropy, temperature, and processing history (Fig. 2). Classical methods provide the physical foundation for tackling this problem, but they are still constrained by the combinatorial growth of the configurational space, the high cost of relaxing and evaluating various possible structures, and the persistent challenge of recovering ensemble-dependent quantities from limited first-principles data. To address these bottlenecks, ML and AI can serve two complementary roles. First, when coupled with classical modeling workflows, ML and AI can accelerate these established workflows by replacing costly energy, force, relaxation, or property evaluations with faster surrogate models that can facilitate configurational exploration, molecular dynamics, and ensemble averaging at much larger length and time scales. Second, beyond acceleration, recent advances have introduced disorder-native capabilities that have been challenging to realize with classical methods alone, such as ordering-sensitive ML representations, disorder-propensity prediction, differentiable chemical identities, and generative models for configurational thermodynamics. Thus, the central distinction among modern AI-driven approaches is not simply whether they use ML, but what physical objects they learn, where they enter the disorder simulation workflows, and whether they primarily boost an existing approximation or provide a brand-new way to represent and model chemical disorder.

3.1 ML as an accelerator for existing modeling formalisms

ML acceleration of established disorder modeling formalisms is easiest to understand by asking which bottleneck in classical simulation workflows the learned ML model is designed to tackle. In this category of data-driven methods, ML does not replace the statistical-mechanics backbone of disorder modeling, but instead lowers the cost of applying established simulation frameworks to chemically complex configurational ensembles. This acceleration can occur at three strongly connected levels (Fig. 6a). First, at the microstate level, the learned models can make individual configurations cheaper to evaluate by predicting energies, forces, stresses, structural relaxations, and configuration-level properties. Second, at the ensemble level, they make the exploration and averaging of different microstates more tractable by coupling surrogate evaluations with Monte Carlo, molecular dynamics, active learning, configurational navigation, or ensemble averaging. Third, at the macroscopic level, they help translate atomistic or ensemble-level information into phase-level thermodynamic descriptions, where uncertainty-aware simulations are increasingly needed for complex multicomponent systems. This hierarchy is helpful because it separates the physical object being learned from the classical framework being accelerated: in all three cases, the configurational ensemble remains the central part of disorder modeling, while ML decreases

the cost and increases the scale and data efficiency with which this ensemble is evaluated.

Accelerating microstate evaluations. The first and most mature acceleration layer targets the repeated, expensive assessment of various site-occupancy microstates. In SQS, finite-ensemble microstate averaging, hybrid Monte Carlo–molecular dynamics, or finite-temperature sampling, one of the most costly procedures is usually the prediction of relaxed structures, energies, forces, stresses, and configuration-level properties for numerous different atomic arrangements. MLIPs directly address such a bottleneck by learning a surrogate PES, thereby replacing repeated first-principles calculations with much more efficient energy and force evaluations.^{228–231} Descriptor-based^{232,233} and graph-based ML models^{234–238} can also be used to infer scalar quantities directly when forces are not needed. In this sense, ML does not alter the underlying statistical-mechanics problem. Instead, it makes each explicit configuration sufficiently low-cost to evaluate, allowing larger supercells, deeper sampling, and broader chemical spaces to be computationally feasible.

MLIPs have evolved from descriptor-based, system-specific force fields toward increasingly expressive and transferable atomistic models. Early MLIPs represent local atomic environments using handcrafted symmetry functions, smooth-overlap descriptors, or relevant representations, and then learn the mapping from these descriptors to atomic energy contributions.^{239,240} These models have pioneered the core idea that DFT-quality energies and forces can be approximated without explicitly solving the electronic-structure problem, but their prediction performance and model transferability depend heavily on the chosen descriptors and training domain.^{228,229} More recent MLIPs increasingly use GNN-based architectures,^{241–245} where atoms or crystallographic sites are treated as graph nodes and local neighbor relationships are treated as graph edges. Such GNN-driven MLIPs learn many-body environment representations directly from data, reducing the need for manual feature engineering and promoting transferability across diverse chemistries and structural motifs.^{246–248} Equivariant message-passing GNN-powered MLIPs further encode rotational and translational symmetries into the architecture,^{249–253} which can be highly valuable for learning complex forces and tensorial responses in chemically disordered solids.^{254,255}

This message-passing view provides a compact way to see how modern graph-based MLIPs evaluate a fixed disordered microstate. For a site-occupancy microstate σ with atomic positions $\{\mathbf{q}_i\}$, each atom i has a hidden feature vector $\mathbf{u}_i^{(\ell)}$ at the GNN layer ℓ , initialized from its discrete chemical identity σ_i and updated by aggregating information from neighboring atoms:²⁴³

$$\boldsymbol{\mu}_i^{(\ell)} = \sum_{j \in \mathcal{N}(i)} \mathcal{M}_\theta^{(\ell)}(\mathbf{u}_i^{(\ell)}, \mathbf{u}_j^{(\ell)}, \mathbf{b}_{ij}) \quad (24)$$

$$\mathbf{u}_i^{(\ell+1)} = \mathcal{U}_\theta^{(\ell)}(\mathbf{u}_i^{(\ell)}, \boldsymbol{\mu}_i^{(\ell)}) \quad (25)$$

$$\widehat{E}_\theta(\sigma, \{\mathbf{q}_i\}) = \sum_i \rho_\theta(\mathbf{u}_i^{(L)}) \quad (26)$$

$$\widehat{\mathbf{f}}_{i,\theta} = -\frac{\partial \widehat{E}_\theta}{\partial \mathbf{q}_i} \quad (27)$$

Here, $\boldsymbol{\mu}_i^{(\ell)}$ is the aggregated message received by atom i at layer ℓ , $\mathcal{N}(i)$ is its neighbor set, and \mathbf{b}_{ij} is an edge embedding denoting the local geometry of the i - j atomic pair, such as interatomic distance, direction, or other symmetry-adapted geometric features. The functions $\mathcal{M}_\theta^{(\ell)}$ and $\mathcal{U}_\theta^{(\ell)}$ are learned message and update functions, respectively; ρ_θ is the learned atomic-energy readout; L is the final message-passing layer; and θ denotes trainable GNN parameters. The hats indicate ML-derived quantities: \widehat{E}_θ is the predicted total potential energy of the specified microstate, and $\widehat{\mathbf{f}}_{i,\theta}$ is the corresponding force acting on atom i , obtained by differentiating the predicted energy with respect to its atomic position. The schematic form in Eqs. (24)–(27) is not meant to suggest that all MLIPs are graph-based. Rather, it shows the architectural logic of many state-of-the-art MLIPs used for molecular and materials simulations. In disorder modeling, a vital point is that the occupational state is predefined before the MLIP is evaluated: each lattice site i is assigned a definite species σ_i , and the model further predicts the energy and forces of this specific atomic arrangement. Hence, conventional GNN-driven MLIPs can accelerate the evaluation of explicit configurations, but they do not by themselves determine which microstates should be generated, sampled, and thermodynamically weighted. These MLIPs are best understood as fast evaluators of explicit atomic configurations, whose broader value in disorder modeling eventually depends on how they are coupled to downstream sampling, search, and ensemble-averaging workflows.

Disordered alloys, multicomponent oxides, and high-entropy materials can offer demanding testbeds for microstate-level ML acceleration, as useful MLIP surrogates need to be transferable across chemical spaces while remaining sensitive to local motifs. Large first-principles datasets spanning ordered and disordered structures (including high-entropy alloys) have recently shown that the prediction performance depends strongly on whether the training data include sufficient configurational and relaxation diversity.^{236,258} Likewise, training-set design methods that sample diverse local motifs have produced accurate MLIPs for predicting stacking-fault energies, short-range order, heat capacities, and phase diagrams of both simple and high-entropy alloys²⁵⁶ (Fig. 6b). Once such desired local-environment coverage is achieved, MLIPs can transform otherwise prohibitive first-principles calculations into tractable disorder modeling or screening workflows. For instance, MLIPs have enabled large-scale simulations of GeSn alloys, revealing short-range ordering and local structural features that would be difficult to access using direct DFT alone.²⁵⁹ In high-entropy oxides, MLIP-driven computational workflows have been used to map complex compositional spaces, rationalize experimentally observed single-phase oxide compositions via bond-length and mixing-enthalpy descriptors, and further prioritize synthesizable candidates in broader search spaces with MLIP-relaxed structures and energy-variance-based descriptors.^{58,59} Beyond general PES evaluation, this MLIP-based microstate-level acceleration similarly applies

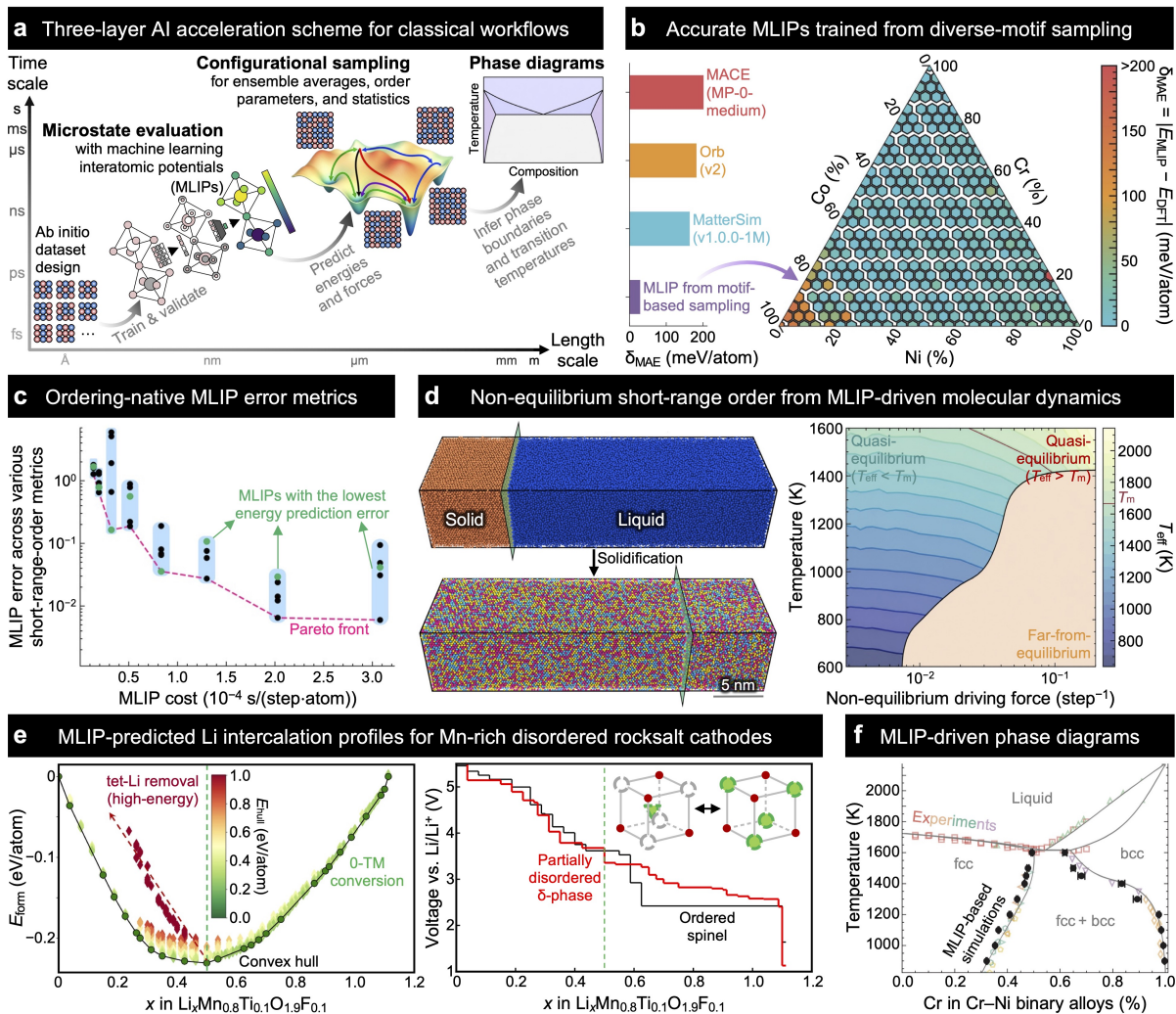


Fig. 6. ML as an accelerator for established atomistic and thermodynamic formalisms for disorder modeling. (a) ML can accelerate all three key layers of conventional disorder modeling workflows, from microstate evaluation to configurational sampling and phase-diagram prediction. (b) Diverse-motif sampling reduces both the magnitude and compositional variability of energy errors relative to broadly trained universal MLIPs.²⁵⁶ (c) Low energy errors alone do not necessarily find the MLIPs that best predict short-range-order-sensitive properties.²⁵⁷ (d) High-fidelity MLIP-driven molecular dynamics enables large-scale simulations of non-equilibrium processing, highlighting how solidification might give rise to short-range-order states beyond equilibrium annealing pathways.⁶³ (e) Fine-tuned universal MLIP simulations help resolve disorder-enabled Li intercalation pathways in Mn-rich disordered rocksalt cathodes, linking Li–vacancy configurations and phase transformation to voltage profiles and accessible capacity.⁶⁴ (f) MLIP-driven sampling converts atomistic energetics into phase diagrams with phase boundaries comparable to experiments and CALPHAD.²⁵⁶ Panels (b), (c), (d), and (f) adapted from ref.²⁵⁶, ref.²⁵⁷, and ref.⁶³, respectively, CC BY 4.0. Panel (e) adapted with permission from ref.⁶⁴, copyrighted by the American Physical Society.

to other specialized tasks that repeatedly appear in disorder modeling workflows, e.g., structural relaxation, defect energetics, and atomic segregation. For example, chemistry-driven relaxation models based on chemical subgraph matching can reduce or bypass expensive DFT relaxations in low-energy configurational exploration of disordered crystal structures.²⁶⁰ Collectively, these studies show that useful microstate-level surrogates are not merely generic energy models: their training data, descriptors, and validation targets must be aligned with the local chemical motifs, relaxation modes, and relative energy scales that control realistic disorder physics in materials.

The design of training data and model validation criteria strongly affects whether microstate-level MLIP surrogates are reliable for disorder modeling, rather than only accurate on traditional disorder-insensitive test sets.^{261,262} Efficient small-cell sampling has been recently employed for multi-principal element alloys to show that these representative small-cell structures can provide a high-quality training dataset for modeling phase transitions, local chemical ordering, and other thermodynamic properties in several multicomponent systems.²⁶³ Moreover, a systematic study of MLIP-driven short-range-order modeling in CrCoNi alloys has shown that conventional held-out energy errors do not necessarily correlate with the ability to capture local-ordering-sensitive quantities, including stacking-fault energies and phase stability, motivating training-data design principles targeted directly at short-range-order fidelity²⁵⁷ (Fig. 6c). These examples show a key requirement for disorder-focused MLIPs: a robust validation protocol must assess whether these models learn the relative energetic ordering, local motif preferences, and ensemble statistics.^{3,93}

Recent advances in universal MLIPs may further expand the reach of microstate evaluation, but their use in disorder modeling still requires careful validation against local ordering physics. Here, universal MLIPs refer to broadly pretrained PES surrogates trained across large chemical and structural datasets^{264–271} to reproduce energies and forces from a specific level of electronic-structure theory.^{77,272} These general-purpose MLIPs have made zero-shot or few-shot structural relaxation, formation energy ranking, and large-scale materials screening efficient across broad chemical spaces.^{264,265,273–278} This capability is particularly attractive for chemically disordered materials, as many of them retain well-defined parent lattices and constituent elements, making universal MLIPs helpful first-pass accelerators for estimating relaxation trends, thermodynamic driving forces, and synthetic accessibility.^{64,279–281} However, broad chemical coverage does not automatically guarantee disorder-aware accuracy for such universal MLIPs. Local strain, charge redistribution, high-energy transition states, and near-degenerate microstates may still place the local environments or relative energy scales outside the training data distribution. For instance, universal MLIPs can misrank atomic configurations in mixed-valence systems when electronic entropy and charge ordering are not properly represented.²⁸² Therefore, universal MLIPs should be regarded as powerful accelerators and physically informative priors, instead of automatically reliable substitutes for disorder-specific model benchmarking, fine-tuning, and validation.

Overall, microstate-level ML accelerators address the first layer of the modeling bottleneck. They make explicit configurations much cheaper to relax, evaluate, and rank, but real disordered states are determined by statistical populations of various competing microstates, rather than by any single configuration alone. Hence, the broader scientific value of these accelerators depends on the next workflow layer: coupling fast surrogate evaluations to configurational sampling and ensemble-averaging protocols to correctly recover the statistical nature of chemical disorder.

Accelerating ensemble workflows. Once individual microstates become efficient to evaluate, the next acceleration layer turns fast ML evaluations into physically meaningful configurational statistics. Chemical disorder is rarely determined by a single low-energy structure alone. Short-range order, configurational entropy, diffusion-relevant motifs, and functional responses emerge from populations of accessible configurations.^{47,73} ML is thus most helpful at this layer when it is embedded into well-established sampling workflows, e.g., Monte Carlo, molecular dynamics, finite-ensemble averaging, and active-learning-driven configurational search. In these methods, ML provides fast prediction of energies, forces, properties, and uncertainty estimates, while the configurational ensemble is still sampled, weighted, and interpreted using statistical mechanics, consistent with the same ensemble averaging formalism introduced in Eqs. (18) and (19).

ML-accelerated Monte Carlo illustrates this strategy by preserving the statistical-mechanics sampler while replacing costly energetic or property evaluations with learned surrogates. Recent attention-based GNN models coupled with Monte Carlo have been used to infer configurational entropy and order–disorder transition temperatures, with a critical observation that the variance of energy prediction errors across various configurations can matter more for disorder properties than ordinary average test error.²³⁸ Similarly, lattice GNN surrogates have enabled Monte Carlo simulations of complex Lu–H–N solid solutions, where interstitial disorder and multicomponent occupation make direct first-principles sampling impractical.²¹³ Beyond energetics, equivariant GNNs integrated with Monte Carlo have been applied to predict ensemble-averaged functional properties, e.g., electrical and optical conductivities in termination-disordered MXenes.²¹⁴ Such examples show how ML can extend ensemble-based strategies from energy averaging to diverse essential observables, while keeping the final prediction as a statistically robust quantity.

Active learning and configurational search algorithms address a complementary bottleneck: determining which atomistic configurations to evaluate, revisit, or use for retraining. In ternary Pd–Pt–Sn alloys, uncertainty-aware GNN surrogates have been employed to explore structures and predict formation energetics with far fewer DFT calculations than exhaustive high-fidelity workflows.²³⁷ Graph-theory-based Monte Carlo tree search has also been introduced to identify representative atomic configurations in disordered solids as the supercell size and compositional complexity increase.²⁸³ Similarly, ML-accelerated evolutionary Monte Carlo has been coupled with MLIPs to explore phase behavior and segregation of compositionally complex materials in

reactive environments.²⁸⁴ Relevant ML-powered Monte Carlo frameworks have been proposed to uncover order–disorder transitions in complex alloys over time scales inaccessible to classical molecular dynamics simulations.²⁸⁵ These methods are best regarded as accelerators of explicit configurational space navigation, rather than directly generating the ensemble distribution itself.

MLIP-driven sampling and dynamics extend ML acceleration from equilibrium statistics to short-range-order evolution across realistic length scales, time scales, and processing pathways. Large-scale ML-enabled atomistic simulations have helped quantify chemical short-range order in metallic alloys,²⁸⁶ while MLIP-powered molecular dynamics have shown that solidification, deformation, and thermomechanical processing can generate non-equilibrium short-range-order states distinct from equilibrium predictions^{63,287} (Fig. 6d). Similar methods have been expanded to disorder-to-partial-order transformation in Mn-rich disordered rocksalt cathode materials for Li-ion batteries⁶⁴ (Fig. 6e), short-range ordering in covalently bonded high-entropy carbides,²⁸⁸ and configurational entropy in compositionally complex ferrite spinels.²⁸¹ These examples show how MLIPs can move disorder simulations beyond individual equilibrium configurations toward finite-temperature, history-dependent, and statistically converged descriptions of disorder.

Collectively, these examples show that ensemble-level ML acceleration succeeds only when faster evaluation is converted into statistically faithful disorder observables. Therefore, the core validation target needs to shift from isolated energy or force errors to the fidelity of the sampled ensemble itself, e.g., its underlying microstate rankings, order parameters, and kinetic pathways. The next step is to propagate ensemble averages into macroscopic thermodynamic descriptions, where ML assists with thermodynamic closure, uncertainty quantification, and data integration.

Accelerating thermodynamic closure. The third acceleration layer begins where microstate evaluation and ensemble sampling finish: transforming atomistic or configurational information into macroscopic thermodynamic descriptions. Many practical questions relevant to chemically disordered solids ultimately require a deep understanding of phase boundaries, miscibility gaps, order–disorder transition temperatures, and synthesis windows, rather than merely microscopic atomic configurations or sampled local motifs. CALPHAD and related thermodynamic models are indispensable for such a purpose, as they provide phase-level free-energy descriptions across various compositions and temperatures. In this context, ML is most helpful as a data-integration and uncertainty-quantification tool, parameterizing thermodynamic models from first-principles or experimental data, unveiling composition–temperature regions where additional calculations are most informative, and propagating atomistic uncertainty into phase-level predictions.²²⁴

Recent operational workflows demonstrate that this thermodynamic closure can be achieved via three concrete routes: automated thermodynamic data generation, experimental-data-guided parameter refinement, and phase-diagram-level benchmarking of ML surrogates. For instance, MLIP-driven CALPHAD workflows can now generate SQS energies, vibrational contributions,

and liquid-phase molecular-dynamics-derived data at substantially lowered computational cost and further use the resulting phase diagrams as application-level tests of MLIP accuracy.^{225,226} A related Pt–W case study has shown that MLIP-derived thermodynamic data can be combined with experimental phase-equilibria information to refine CALPHAD parameters, with a modest adjustment to physically grounded Gibbs-energy descriptions substantially boosting agreement with experimentally measured phase boundaries.²²⁷ Complementary MLIP studies across alloy compositional spaces have demonstrated that phase diagrams provide stringent thermodynamic validation targets beyond static energy errors, highlighting that calibrated MLIPs can reproduce experimentally consistent phase boundaries across diverse alloy systems²⁵⁶ (Fig. 6f). Together, these studies help define a practical AI-driven closure route: ML first accelerates the generation, benchmarking, and tuning of thermodynamic inputs, while CALPHAD and relevant phase-level formalisms preserve the interpretable free-energy structure needed for equilibrium prediction.

Atomistic-to-thermodynamic integration becomes particularly valuable in high-dimensional compositional spaces where brute-force phase-diagram construction is difficult. As an example, GNN surrogates can predict configuration- and pressure-dependent equation-of-state quantities that are subsequently transformed into Gibbs energies and phase diagrams for a multicomponent interstitial solid solution.²¹³ This workflow is highly useful, as it does not stop at configurational evaluation. Instead, it uses ML-accelerated sampling to produce thermodynamic quantities that can be interpreted at the phase level. A complementary approach has been developed for multi-principal element alloys, where the thermodynamic stability of complex alloys can be estimated from lower-dimensional subsystem energetics with meV-scale accuracy, while retaining a strong connection to cluster-expansion theory and experimentally reported synthesizability trends.¹⁵⁴ Collectively, these examples show that ML-assisted atomistic models can supply disorder-aware inputs for thermodynamic assessments, while phase-level constraints can subsequently suggest which compositions, configurations, and temperature ranges deserve further evaluation.

Uncertainty quantification is the key requirement that distinguishes thermodynamic closure from standard high-throughput atomistic prediction. Critical phase boundaries, miscibility gaps, and order–disorder transition temperatures can shift substantially when competing free energies differ by merely a few meV/atom. Hence, single-value ML predictions can be insufficient unless uncertainties are propagated into the thermodynamic model. In chemically disordered materials, this uncertainty can arise from various sources, e.g., first-principles errors, ML surrogate errors, finite-size configurational sampling, incomplete theoretical treatments of vibrational, magnetic, and electronic entropies, and experimental errors.²²⁰ To evaluate these uncertainties, Bayesian thermodynamic assessments, Gaussian-process corrections, ensemble-driven models, gradient-informed optimization, and active-learning loops can all help identify composition–temperature regions where predictions remain underconstrained.²²⁴ Without these analyses, ML-accelerated

thermodynamic closure may appear informative while remaining physically undervalidated.

At this closure layer, agentic workflows can be helpful as orchestration tools that coordinate physically constrained simulation steps. Large-language-model-driven computational AI agents may help coordinate first-principles calculations, MLIP relaxations, configurational sampling, thermodynamic parameter fitting, and experimental data assimilation in closed loops.^{289–292} The scientific value of these agentic tools, however, will depend on whether the underlying physical modeling, uncertainty estimates, and thermodynamic constraints remain explicit, auditable, and reproducible.^{224,293} A realistic near-term goal is thus not black-box, autonomous phase-diagram discovery, but robust atomistic-to-thermodynamic pipelines in which ML accelerators offer fast and uncertainty-calibrated inputs, while thermodynamic formalisms further enforce consistency across phases, compositions, and temperatures to facilitate reliable phase-level prediction.

Taken together, these three acceleration layers show that ML can greatly expand the practical reach of established disorder formalisms without changing their physical foundations. It makes microstate evaluation less expensive, ensemble exploration broader, and thermodynamic closure more scalable, while the physical description and predictive interpretation of chemical disorder remain deeply grounded in classical statistical mechanics and solid-state thermodynamics.

3.2 ML as an enabler for novel disorder-native capabilities

ML can also move beyond accelerating classical simulation workflows by making disorder itself the direct target of prediction, representation, generation, and optimization. This role is different from the acceleration strategies discussed earlier, where ML mainly lowers the cost of applying well-established simulation formalisms for faster microstate evaluation, broader configurational sampling, and more physically grounded thermodynamic closure. By contrast, in this category of data-driven approaches, ML offers fundamentally new ways to interact directly with chemical disorder prior to, during, and beyond conventional atomistic simulations. ML can first function as a disorder-aware decision layer, identifying when an ordered computational candidate should be analyzed cautiously, routed into explicit, high-fidelity disorder modeling, or reinterpreted as an ordered derivative of a known disordered family. It can further improve the representation of disorder by preserving the ordering and symmetry of coordination environments and describing key alchemical relationships that conventional ML representations of solid-state materials may obscure. Beyond prediction and representation, generative AI approaches can directly construct disordered crystals, representative configurational ensembles, and thermodynamic distributions, rather than only assessing atomistic configurations selected with an external sampling workflow. Lastly, kinetics-informed ML models can target barriers, rates, transition rules, and first-passage times that predict how disorder forms, relaxes, and becomes trapped under crucial synthesis and operating conditions. These disorder-native AI capabilities are best regarded as complementary

extensions, instead of replacements for conventional ML-accelerated sampling workflows: they help clarify when disorder must be modeled, how it should be represented, what configurational distributions should be generated, and which kinetic steps may govern disorder experimentally.

Enabling disorder-aware workflow triage. Disorder-aware triage can offer a vital upstream AI capability that is different from simply accelerating an existing disorder modeling workflow. Instead of evaluating explicit microstates, sampling a known configurational ensemble, or using a thermodynamic model, the core prediction task is to decide whether an ordered computational candidate from high-throughput screening^{265,294,295} and generative inverse design^{78,296,297} should be trustworthy in the first place. This disorder-triage capability has become increasingly critical, as high-throughput screening and generative workflows still mainly operate on highly idealized, chemically ordered structures,^{265,295,296} whereas experimentally reported materials often contain partial occupancies, occupational disorder, and symmetry-averaged crystal descriptions.^{80,298,299} A disorder-aware triage tool can thus help estimate whether an ordered candidate downselected from high-throughput screening and inverse design workflows is trustworthy or, alternatively, it should be viewed as disorder-prone for further computational or experimental examination.

The most straightforward form of disorder-aware triage is to make crystallographic disorder itself the prediction target. For instance, ML classifiers trained on experimental inorganic crystal structures can learn chemical trends associated with crystallographic disorder and estimate how frequently such chemical disorder occurs in computational databases.²⁹⁹ This framing is crucial, as it can be utilized as a signal indicating when conventional convex-hull evaluation of ordered structures^{262,265,296} should be interpreted cautiously and followed by more detailed and rigorous disorder analysis.^{80,299} Relevant property-oriented ML workflows also show that experimentally reported chemical disorder can provide helpful structure–property information. As an example, an experimental structure–conductivity database of Li-containing compounds has been coupled with graph-based ML featurization to classify both ordered and disordered structures as possible superionic Li conductors, leading to subsequent screening and experimental validation of a new ion-conductor material.³⁰⁰ Overall, these examples show that disorder-aware learning and triage can promote both workflow routing and property screening by treating experimental disorder as valuable information in AI-driven materials discovery, rather than as representational noise.

Disorder-aware triage also requires crystallographic representations and comparison toolkits that can place ordered and disordered structures on a common basis. For example, a symmetry- and Wyckoff-sequence-based ML representation has recently been built to encode both ordered and disordered solids, including co-occupying atomic species and continuous site-stoichiometry information.³⁰¹ Such a representation tackles a database-scale challenge that previous atomistic descriptors cannot solve cleanly: deciding whether two crystal data records describe genuinely distinct compounds, or alternatively, differently ordered or partially occupied representations of

the same underlying disordered structure. This comparison issue has been particularly important for assessing novelty in AI-generated or high-throughput ordered structures.^{80,302–305} Moreover, order–(dis)order family trees based on group–subgroup relationships have been further designed to identify cases in which an apparently new ordered structure is more appropriately considered as an ordered child of an existing disordered parent.³⁰⁶ Recent critiques of generative AI models reinforce the same point, showing that apparent predictions can overlap with compounds already represented in training data and that novelty evaluation should thus account for order–(dis)order structural relationships, rather than based on only data absence from an existing database.³⁰⁷ For disorder modeling, this warning is particularly consequential, as an AI-predicted ordered crystal structure should not automatically be regarded as a new material if it is either configurationally, symmetrically, or compositionally related to an experimentally reported disordered phase.

Overall, disorder-aware workflow triage offers a vital front-end capability that complements, rather than replaces, explicit disorder modeling. In other words, these methods do not determine the equilibrium distribution of site-occupancy microstates, nor do they bypass the need for SQS, cluster expansion, Monte Carlo, finite-ensemble averaging, and MLIP-enhanced sampling when detailed disorder thermodynamics is required. Their essential value is instead to make AI-driven materials screening or generation workflows more physically grounded, before costly follow-up calculations and experiments are performed. By identifying when disorder should be considered explicitly, when ordered predictions require reinterpretation, and when apparently novel crystal structures are better viewed as different representations of known chemical disorder, this triage layer can help promote experimentally grounded decisions in AI-driven materials discovery.

Enabling ordering-sensitive and alchemical representations. After a crystal candidate has been identified as potentially disorder-relevant, the next ML problem is to represent its ordering degrees of freedom without removing the distinctions that make different microstates physically meaningful. This capability differs from using an MLIP or GNN purely as an efficient evaluator of a fixed configuration. In conventional microstate evaluation, the site occupations are already specified, and the model primarily infers energies, forces, stresses, or properties of these explicit atomic arrangements.^{228–231,234} In disorder-sensitive representation learning, by contrast, the key question is whether ML models can preserve the symmetry, site occupation, local coordination, short-range correlation, and chemical-identity information needed to distinguish configurations that may share the same composition and average lattice. This requirement is important because relative microstate stability, local motif preference, and short-range order can all depend heavily on subtle differences that are easily lost if the representation is too compositionally coarse.

Ordering-aware representations first address the discrete symmetry problem that arises when various lattice occupational configurations are physically distinct but compositionally identical. Conventional symmetry-invariant GNNs can struggle to differentiate diverse symmetry-distinct

orderings of the same crystalline composition, while symmetry-aware graph representations can better retain the critical ordering information needed for energy and property prediction⁹³ (Fig. 7a). The implication for disorder modeling is straightforward: an ML model cannot accurately rank different microstates if its representation maps physically inequivalent ordering patterns to nearly identical features, as these ordering differences might be exactly what control the relative energies and Boltzmann weights of the configurations. Related representation needs arise when the relevant disorder variable is not a single ordered microstate, but a spatially distributed short-range-order pattern. Multiscale ML-based analyses of metallic alloys have shown how chemical short-range order can be assessed at realistic length scales using symmetry-sensitive equivariant GNNs and related to local lattice distortions and experimentally relevant spatial statistics^{286,308} (Fig. 7b). In this view, long- and short-range chemical orderings can become ML-resolved state variables for learning, rather than merely perturbations around ideal random solid solutions.

Chemically complex disorder requires ML representations that can learn chemical similarity more continuously than one-hot elemental labels allow. For example, alchemical variants of ML representations based on the smooth overlap of atomic positions³¹⁰ have shown that correlations between chemical species can be optimized from data, giving rise to learned chemical similarity maps resembling and extending periodic-table chemical trends.³¹¹ This idea can be valuable for chemically disordered materials, since multicomponent compositional spaces are more tractable when elements are embedded in a continuous, similarity-aware manifold, rather than treated as uncorrelated categorical identities. Alchemical compression has further converted this concept into a practical simulation approach for chemically complex disorder by reducing the effective compositional dimensionality of high-entropy alloys. For example, an alchemically compressed representation has been developed to construct an MLIP spanning 25 transition metals, retaining semi-quantitative accuracy for alloy energetics and short-range-order trends while also enabling the extraction of chemical rules from the compressed alchemical manifold.⁹² Recently, the same compressed chemical representation has also been extended to modeling surface segregation in high-entropy alloys, where local compositional preferences are amplified by symmetry-broken surface environments.³¹² These studies highlight that ML-learned chemical manifolds can make large chemically complex disorder spaces much more navigable, while still retaining chemically meaningful ordering trends and segregation tendencies in data-driven disorder modeling.

A more direct alchemical modification of GNN-based MLIPs can promote site identity itself from a discrete data label to an interpolable, differentiable, and optimizable model parameter.⁹⁵ The novelty is not simply building MLIPs that predict energies faster, but enabling a new family of MLIPs where chemically disordered lattice sites become directly computable input variables. In conventional GNN-driven MLIPs, each site is assigned one definite chemical identity before message passing begins. By contrast, alchemical graph augmentation allows a crystallographic

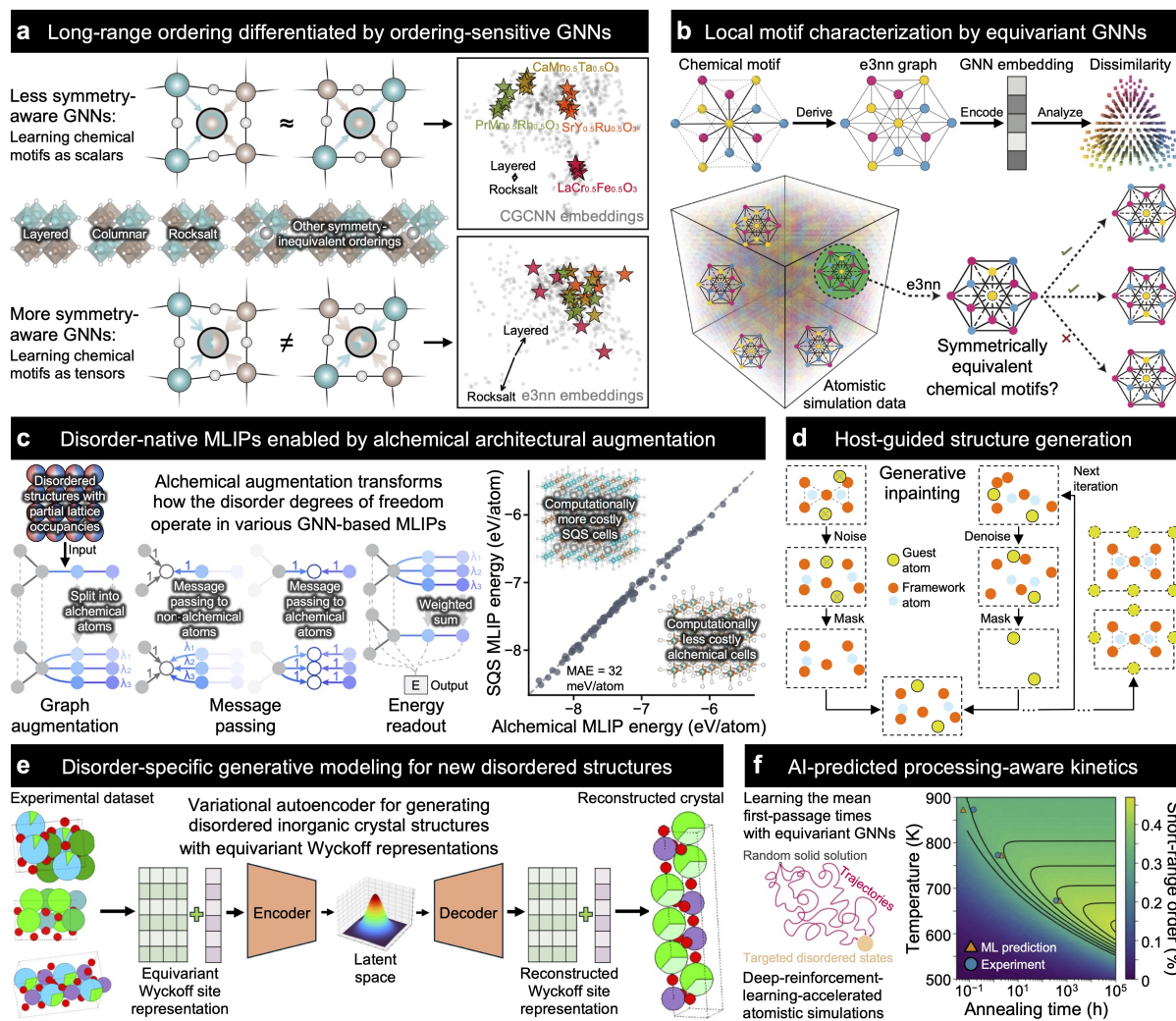


Fig. 7. ML as an enabler of disorder-native capabilities beyond conventional atomistic simulation workflows. (a) Symmetry-equivariant GNNs can better distinguish long-range orderings that conventional invariant models can regard as nearly equivalent, enabling ordering-dependent energetics to be learned more faithfully.⁹³ (b) Equivariant GNNs identify symmetrically equivalent chemical motifs and embed them into a dissimilarity space for quantifying short-range order beyond traditional Warren–Cowley parameters.^{286,308} (c) Alchemical augmentation can introduce continuous site-occupancy degrees of freedom into MLIPs, enabling compact disorder representations and low-cost disorder energetic prediction.⁹⁵ (d) Host-guided inpainting generation uses a symmetrized framework to place guest atoms, driving the diffusion-model-driven generation of crystal structures with intercalation chemistry.³⁰⁹ (e) Disorder-native generative models encode partial occupancies using equivariant Wyckoff representations, enabling reliable generation of symmetry-consistent disordered structures.⁹⁴ (f) Mean-first-passage-time learning combines equivariant GNNs and reinforcement learning to predict short-range-order kinetics beyond traditionally accessible time scales.⁶⁵ Panels (a), (b), (c), (e), and (f) adapted from ref.⁹³, refs.^{286,308}, ref.⁹⁵, ref.⁹⁴, and ref.⁶⁵, respectively, CC BY 4.0. Panel (d) adapted with permission from ref.³⁰⁹, copyrighted by the Royal Society of Chemistry.

site to carry multiple possible chemical identities with continuous weights, and thus, the partial occupancy on this lattice site can be an interpolable and optimizable MLIP parameter (Fig. 7c), rather than just a post-processing approximation.⁹⁵ This formulation can be written as a minimal extension of the conventional graph-based MLIP notation in Eqs. (24)–(27). We can consider a crystallographic site i that can be represented by K_i alchemical states, which are further indexed by $a = 1, \dots, K_i$. Each alchemical state has a definite chemical identity χ_{ia} and a non-negative alchemical weight λ_{ia} . For a partially occupied site, the alchemical weights imply the fractional contribution of each possible chemical identity. Thus, they are non-negative and sum to one:

$$\sum_{a=1}^{K_i} \lambda_{ia} = 1, \quad \lambda_{ia} \geq 0 \quad (28)$$

A non-disordered, fully occupied lattice site is simply recovered by setting $K_i = 1$ and $\lambda_{i1} = 1$. Through this alchemical graph augmentation, the original site i is replaced by alchemical nodes (i, a) that share the same atomic position \mathbf{q}_i but are initialized using the corresponding chemical identities χ_{ia} . Consequently, the message aggregation in Eqs. (24) and (25) is modified as:

$$\tilde{\boldsymbol{\mu}}_{ia}^{(\ell)} = \sum_{(j,c) \in \tilde{\mathcal{N}}(i,a)} \gamma_{ia,jc} \mathcal{M}_{\theta}^{(\ell)} \left(\tilde{\mathbf{u}}_{ia}^{(\ell)}, \tilde{\mathbf{u}}_{jc}^{(\ell)}, \mathbf{b}_{ij} \right) \quad (29)$$

$$\tilde{\mathbf{u}}_{ia}^{(\ell+1)} = \mathcal{U}_{\theta}^{(\ell)} \left(\tilde{\mathbf{u}}_{ia}^{(\ell)}, \tilde{\boldsymbol{\mu}}_{ia}^{(\ell)} \right) \quad (30)$$

where tildes denote quantities defined on the alchemically augmented graph, $\tilde{\mathcal{N}}(i, a)$ represents the neighbor list of the alchemical node (i, a) , c indexes the alchemical state on neighboring site j , and $\gamma_{ia,jc}$ indicates a non-learned message weight that rescales selected message contributions according to the alchemical composition. An asymmetric weighting scheme consistent with the original graph message-passing process in the underlying non-alchemical MLIP is:

$$\gamma_{ia,jc} = \begin{cases} \lambda_{jc}, & K_i = 1, K_j > 1 \\ 1, & \text{otherwise} \end{cases} \quad (31)$$

This weighting scheme allows a partially occupied neighboring site to contribute to the message passing based on its fractional chemical identity, while keeping the learned message and update functions, $\mathcal{M}_{\theta}^{(\ell)}$ and $\mathcal{U}_{\theta}^{(\ell)}$, unchanged from the underlying non-alchemical MLIP. The readout in Eq. (26) can be further replaced by a weighted sum over alchemical node contributions:

$$\widehat{E}_{\theta}^{\text{alc}}(\{\lambda_{ia}\}, \{\mathbf{q}_i\}) = \sum_i \sum_{a=1}^{K_i} \lambda_{ia} \rho_{\theta} \left(\tilde{\mathbf{u}}_{ia}^{(L)} \right) \quad (32)$$

The forces remain available by differentiating the MLIP energy with respect to atomic positions:

$$\widehat{\mathbf{f}}_{i,\theta}^{\text{alc}} = - \frac{\partial \widehat{E}_{\theta}^{\text{alc}}}{\partial \mathbf{q}_i} \quad (33)$$

As the energy is also differentiable with respect to the alchemical weights, the same automatic-differentiation machinery can provide useful compositional space gradients that highlight how changing the partial occupancy of a mixed lattice site would raise or lower the predicted energy. For the crystallographic site i , this compositional space gradient can be written as:

$$\mathbf{g}_{i,\theta}^\lambda = \nabla_{\lambda_i} \widehat{E}_\theta^{\text{alc}} = \left(\frac{\partial \widehat{E}_\theta^{\text{alc}}}{\partial \lambda_{i1}}, \dots, \frac{\partial \widehat{E}_\theta^{\text{alc}}}{\partial \lambda_{iK_i}} \right) \quad (34)$$

where $\lambda_i = (\lambda_{i1}, \dots, \lambda_{iK_i})$ shows the alchemical weights on site i , and $\mathbf{g}_{i,\theta}^\lambda$ is the corresponding compositional space gradient. These gradients make the stoichiometry of any disordered lattice site directly optimizable. Gradient-driven optimization can update the fractional occupancies in the direction that lowers the predicted energy, while projecting the updated weights back so that these stoichiometric parameters in disordered crystals remain non-negative and sum to one:

$$\lambda_i^{(t+1)} = \Pi_{\Delta_i} \left[\lambda_i^{(t)} - \eta_\lambda \mathbf{g}_{i,\theta}^\lambda \right] \quad (35)$$

where t is the optimization step, η_λ is the step size for the alchemical weights, $\Delta_i = \{\lambda_i : \lambda_{ia} \geq 0, \sum_{a=1}^{K_i} \lambda_{ia} = 1\}$ is the set of physically valid fractional occupancies on site i , and Π_{Δ_i} denotes the projection step that maps the updated weights back into this allowed set. Hence, alchemical graph augmentation fundamentally changes the role of chemical identity in GNN-based MLIPs. Instead of treating lattice site occupation as a fixed discrete input, it makes the partial occupancy an internal, differentiable degree of freedom that can be interpolated, optimized, and compared across ordered and disordered representations of the same parent structure. Because the learned message, update, and readout functions from underlying non-alchemical MLIPs are preserved, this alchemical graph augmentation strategy can, in principle, be applied across different GNN-driven MLIP backbones^{251,264} and can benefit from the continuous improvements in pretrained universal MLIPs²⁶² without requiring a brand-new alchemical model trained from scratch. This enables disorder-native operations, e.g., gradient-based compositional optimization, alchemical free-energy calculations for substitutions and vacancies, and accurate, efficient classification of experimental long-range order–disorder competition in multicomponent perovskite materials.⁹⁵ In this sense, alchemical MLIPs convert partial occupancy that requires enumeration and post-processing for effective sampling into a differentiable, optimizable variable in these models.

Taken together, ordering-sensitive and alchemical representations have made representation design itself a disorder-native ML capability. Symmetry-aware GNNs help preserve distinctions among physically inequivalent ordered microstates. Short-range-order-sensitive representations expose local chemical correlations. Alchemical compression further makes chemically complex compositional spaces more navigable, and alchemical MLIPs transform partial occupancy into a directly interpolable and differentiable model parameter. Crucially, these advances are not only architectural refinements that improve prediction accuracy: they also determine which disorder

variables remain visible to the model in the first place. At the same time, their value for disorder modeling must ultimately be judged by configurational and thermodynamic fidelity. Physically robust representations must therefore preserve microstate rankings, local ordering trends, order parameters, and ensemble-level observables at an energy scale relevant to Boltzmann weighting, rather than only achieving low errors on conventional held-out energy and force benchmarks.

Enabling disordered structure and distribution generation. After vital disorder parameters become visible using ordering-sensitive and alchemical representations, a subsequent disorder-native AI capability is to generate disordered structures or configurational distributions directly. This approach is different from using ML only within an externally defined ensemble workflow. In ML-boosted Monte Carlo, molecular dynamics, active learning, or finite-ensemble averaging, the sampling procedure is generally specified outside the model, while ML offers fast energies, properties, or uncertainty estimates.^{64,213,214,237} By contrast, in generative modeling, the learned object can be a plausible disordered crystal description, a representative category of microstates, a benchmarked statistical distribution over disordered configurations, or an approximation to a thermodynamic object (such as a partition function). Thus, ML starts to help build the disorder ensemble itself, rather than only assessing configurations selected by another algorithm.

Generalized generative models for inorganic materials^{78,297} have already shown how crystal-structure distributions can be learned from large-scale datasets, but they still need stronger ways to represent and validate partial occupancy and related order–disorder relationships. MatterGen has set a leading example: it acts as a diffusion model that simultaneously generates atom types, fractional coordinates, and lattice degrees of freedom, which can be fine-tuned toward chemical, symmetry, or scalar property constraints.²⁹⁶ It represents a crucial advance for inverse materials design, including reported improvements in stable, unique, and new structure generation and an experimental validation example involving a compositionally disordered material. Nonetheless, while the MatterGen workflow has already attempted to account for disorder via order–disorder structural matching,²⁹⁶ a subsequent crystallographic reanalysis³⁰⁷ has argued that the Ta–Cr–O validation example is more appropriately interpreted as a known disordered rutile solid-solution family rather than a genuinely novel compound, showing that disorder remains a difficult failure mode for current generative materials modeling. The central challenge is thus not only whether an AI model can generate thermodynamically low-energy ordered structures, but whether it can recognize when an ordered prediction should be better interpreted as merely an approximation to an already known disordered phase. Conditional generation may partly narrow this gap when the parent lattice or host framework is known. As a representative example, crystal host-guided generation combines inpainting generation with universal MLIP relaxation to generate missing or uncertain structural components within various host frameworks, which is naturally relevant to partial occupancy, intercalation chemistry, vacancies, and site-mixing problems³⁰⁹ (Fig. 7d).

Thus, while generalized generative models provide the foundation for learning crystal-structure distributions, disorder-native crystal generation still requires tools that can distinguish genuinely new disordered materials from ordered representations of known disorder in solid materials.

Disorder-specific generative modeling thus requires representations that can directly capture partial occupancies, rather than only producing ordered approximations. One route toward this target is to generate Wyckoff-level objects, as shown by WyckoffDiff,³¹³ which uses symmetry-based prototypes to preserve crystallographic symmetries by construction. Dis-GEN also offers an essential example of this shift by designing a crystallographic equivariant representation that can accommodate partial occupancies while further ensuring symmetry consistency⁹⁴ (Fig. 7e). Since this generative framework is trained on experimental structures from the Inorganic Crystal Structure Database^{314,315} and directly operates on disordered crystallographic descriptions,²⁹⁸ it moves generative modeling closer to the way disordered solids are reported experimentally. The conceptual advance is therefore not simply the generation of another ordered configuration, but the generative modeling of symmetry-consistent partial-occupancy structures that can represent disordered materials more compactly than explicit enumeration of different ordered microstates. More recently, DMFlow has extended this direction by using a unified representation for ordered and disordered crystal structures, combined with simplex-constrained flow matching to generate physically valid disorder weights.³¹⁶ These methods have established the representational basis for disorder-native generation, while also raising the next question of whether generated partial-occupancy descriptions capture the correct configurational statistics in disordered solids.

Generative models for chemical disorder further require benchmarks that assess whether the generated configurations reproduce the correct statistical distribution of site occupations, rather than only whether individual structures appear valid or novel. Dismal-Bench provides a helpful step in this direction through its fixed-composition $\text{Fe}_{60}\text{Ni}_{20}\text{Cr}_{20}$ alloy datasets, where generative models are evaluated for their ability to reproduce face-centered-cubic alloy configurations with various degrees of short-range order.³¹⁷ As the composition and lattice type are preselected, AI-generated alloy structures can be compared directly against known configurational distributions using cluster fingerprints and short-range-order statistics, making this benchmark more relevant to chemical disorder than conventional validity or novelty metrics. This example highlights that disorder-native generative benchmarks should examine not only whether a model can generate plausible atomic configurations, but whether it can reproduce the occupational correlations that define the underlying configurational ensemble in realistic chemically disordered materials.

Beyond disordered crystal-structure generation, a more ambitious disorder-native generative target is the thermodynamic distribution of microstates. Autoregressive samplers adapted to the semi-grand canonical ensemble provide one lattice-based realization of this idea: SEGAL learns condition-dependent microstate probabilities at predefined temperature and chemical potential,

driving free-energy and phase-stability estimation while remaining compatible with an arbitrary internal-energy model.³¹⁸ More recent any-order autoregressive and marginalization models can further improve scalability by enabling out-painting from smaller to larger lattices and memory-efficient direct training, extending thermodynamic generation toward larger alloy supercells and across wider temperature–chemical-potential conditions.³¹⁹ Another vital example is an inverse variational autoencoder that has been developed to iteratively generate atomistic configurations, evaluate them via atomistic calculations, and update the model toward estimation of the partition function.³²⁰ A feature of this approach is that it does not require a pre-existing training dataset, but instead builds the relevant configurational sampling set through the generative-learning loop itself. For U–Pu mixed oxides, this framework has been used to compute point-defect formation energies and concentrations, thereby showing how local chemical environments influence defect behaviors. These examples highlight how thermodynamic generative modeling can be valuable for modeling chemically disordered materials: the central goal is to recover ensemble statistics, e.g., defect concentrations, free energies, short-range-order tendencies, and averaged properties, without exhaustively enumerating all the microstates that contribute to the partition function.

Overall, generative AI can move disorder simulations from evaluating predefined atomistic configurations toward constructing the vital disordered structures, configurational distributions, and thermodynamic objects that should be analyzed in the first place. Nevertheless, the value of these generative models depends on whether the generated outputs are faithful to the underlying disorder physics, not just whether they are structurally valid, low in energy, or apparently novel. A disorder-native generative model must therefore preserve partial occupancies, order–disorder relationships, occupational correlations, microstate statistics, and thermodynamic weights at the level required for ensemble prediction. In this setting, generative AI is most beneficial when it is integrated with crystallographic constraints, accurate energy models, agentic ML workflows, and validation versus ensemble-level observables. Such an integration can help make generative AI a complementary tool for statistical mechanics: not a replacement for sampling, but a way to compress and prioritize the disorder distributions that merit detailed thermodynamic evaluation.

Enabling processing-aware disorder kinetic prediction. After disordered crystal structures and related thermodynamic distributions are generated, another disorder-native AI capability is to capture the kinetic quantities that control how chemical disorder forms, relaxes, and becomes trapped. This role is different from using ML models (e.g., MLIPs) only to run longer molecular dynamics trajectories: faster PES exploration can extend accessible length and time scales, but direct MLIP-driven molecular dynamics can still be too expensive for activated diffusion events, vacancy-mediated site exchanges, and processing-scale relaxation, as these processes may occur on time scales far longer than affordable atomistic trajectories.³²¹ By contrast, when ML learns migration barriers, jump probabilities, transition rules, kinetic rates, or mean first-passage times,

the learned model becomes a reduced kinetic description of disorder evolution. This distinction is important, as disorder is not always an equilibrium endpoint: it may alternatively be a history-dependent state affected by annealing, quenching, and other common operating conditions.

One route toward processing-aware disorder kinetics is to learn the local transition rules that determine diffusion-induced chemical ordering. A neural-network-based kinetic framework has been established to predict path-dependent migration barriers and simulate individual vacancy-mediated atomistic jumps using an efficient on-lattice structural and chemical representation.⁶⁰ Applied to refractory NbMoTa alloys, this approach has revealed a temperature regime in which B2-type chemical ordering is maximized and connected such a behavior to diffusion multiplicity and heterogeneous atomic mobility. This example highlights how ML-driven kinetic models can be more than fast evaluators of static configurations by learning the barrier landscape and jump statistics that determine which ordering pathways can actually develop through diffusion.

A complementary approach is to learn the time required for a chemically disordered system to relax toward a desired ordering state. Deep reinforcement learning combined with temporal-difference learning has been used to predict the mean first-passage times for diffusive relaxation and short-range-ordering formation in medium- and high-entropy alloys⁶⁵ (Fig. 7f). In this ML-powered modeling framework, reaction models encode vacancy-diffusion events, reinforcement learning promotes the search for lower-energy ordering trajectories, and a learned time estimator restores the kinetic information needed to connect these trajectories to physical relaxation times. By connecting the dependence of short-range-order formation to temperature, time, and vacancy concentration, this approach helps separate thermodynamic driving forces from kinetic trapping. It helps tackle a key question that static energetics alone cannot answer: not only which ordering pattern is favorable, but how long it takes to form under a particular processing condition.

These kinetic models can be especially essential because experimentally observed chemical disorder often reflects competition between thermodynamic preference and kinetic accessibility. Annealing temperature, quench rate, defect concentration, diffusion barriers, and local chemical environment can jointly determine whether a material may reach equilibrium short-range order, stay metastable, or freeze into a non-equilibrium distribution of local motifs. Static calculations and equilibrium sampling can predict favorable configurations or ensemble averages, but kinetic models are critical for determining whether those configurations are reachable on realistic time scales and whether they would be retained after processing. A limitation of these kinetic models is that small errors in barriers, attempt frequencies, or transition probabilities might compound into much larger prediction errors in long-time evolution. Thus, robust validation requires more than short-time trajectory agreement: these ML-driven kinetic models should be able to capture experimentally known diffusion coefficients, ordering time scales, rare-event statistics, and key order-disorder trends across compositions, temperatures, and other processing conditions.

Taken together, these disorder-native capabilities have transformed AI from a cost-reduction tool for classical workflows into a fundamentally new approach to identify, represent, generate, and dynamically encode the physical objects and design principles that define chemical disorder. Disorder-aware triage helps unveil when ordered predictions require explicit disorder treatment. Ordering-sensitive and alchemical representations preserve the essential structural and chemical variables that largely control microstate ranking, local motif preference, and ensemble statistics. Generative models construct partial-occupancy structures and configurational distributions that can serve as valuable inputs for disorder prediction. Kinetic models eventually connect disorder states to various processing pathways through which they can form, relax, and become trapped. The core value of these disorder-native AI capabilities is not to completely replace SQS, cluster expansion, Monte Carlo, and MLIP-powered sampling, but to make such established tools more targeted, disorder-aware, and experimentally grounded. The central challenge ahead is therefore integration: disorder-native AI approaches must be coupled with statistically rigorous sampling, accurate energy models, uncertainty quantification, and kinetic validation to ensure that disorder can be predicted efficiently and reliably across thermodynamic and processing conditions.

4. Grand challenges and future perspectives

In conclusion, classical and AI-driven modeling approaches have jointly expanded the chemical complexity and atomistic length and time scales accessible for chemically disordered materials. Classical approaches have made chemical disorder computationally tractable by replacing the impractical enumeration of all site-occupancy microstates with complementary approximations (Figs. 4 and 5): effective average media, fitted lattice-model Hamiltonians, representative quasi-random supercells, finite-size ensembles, stochastic sampling, and macroscopic thermodynamic models. These classical methods have established the physical language of disorder simulations by transforming partial site occupancies, local correlations, configurational entropies, and phase equilibria into directly computable quantities. Nonetheless, these classical modeling approaches remain constrained by a representation–sampling bottleneck: as chemical complexity, sublattice diversity, local structural relaxation, and finite-temperature effects increase, relevant microstates become harder to select, evaluate, weight, and validate without introducing bias. To address this critical bottleneck, AI can play two complementary roles: it can accelerate established modeling strategies (Fig. 6), and it can further enable new disorder-native ML workflows, representations, and predictions that have been challenging to realize using conventional methods alone (Fig. 7). As accelerators, ML can largely reduce the cost of microstate evaluation, expand configurational sampling, and facilitate atomistic-to-thermodynamic closure through energy prediction models, uncertainty-boosted searches, and data-driven phase-diagram assessments. As enablers, ML can also catalyze new disorder-native capabilities, such as disorder-aware workflow triage, ordering-

sensitive and alchemical representations, generative construction of disordered lattice structures and thermodynamic distributions, and fast kinetic prediction of processing-dependent orderings. Overall, these methodological developments mark a key transition from merely making disorder computable to making the modeling broader, faster, more accurate, and more directly connected to critical thermodynamic and kinetic quantities that govern realistic chemical disorder.

Despite this methodological transition, faster and more flexible simulation workflows do not automatically guarantee more faithful prediction of chemical disorder. While classical atomistic and thermodynamic formalisms are relatively mature, many emerging AI-driven approaches for disorder modeling have so far been demonstrated on simplified lattices, limited chemical spaces, idealized benchmark systems, and confined configurational datasets (Fig. 3). Consequently, the broader value of these AI-assisted modeling workflows will largely depend on whether they can transfer to more realistic, complex disordered materials, where multiple sublattices, strong local relaxation, entangled internal degrees of freedom, finite-temperature entropies, kinetic trapping, and heterogeneous environments may all jointly control the relevant configurational ensembles. A useful disorder-native AI model should thus capture the free energies, local motif populations, transition temperatures, kinetic accessibility, and important ensemble-averaged observables that determine the experimental behaviors and properties of chemically disordered materials.

This gap between faster modeling and more trustworthy prediction defines the future agenda for AI-assisted disorder modeling (Fig. 8). The next step is not simply to substitute conventional formalisms with larger ML models, but to integrate these data-driven strategies with free-energy calibration, experimental constraints, uncertainty quantification, additional degrees of freedom, and physically robust ensembles that expand beyond bulk crystals. Such tasks can be viewed as increasingly realistic tests for AI-driven modeling, transitioning from model and data calibration to complex physical variables, experimental inversion, and heterogeneous environments.

4.1 Phase-level fidelity calibration and theory–experiment alignment

The first goal in this forward-looking agenda is to make experimentally constrained free-energy behaviors the central targets of AI-assisted atomistic disorder modeling, rather than relying only on energy and force labels. Traditional modeling formalisms and modern ML accelerators have substantially expanded the capability to represent, assess, sample, and interpret configurational ensembles, but this advance does not by itself guarantee predictive alignment with experiments. A model that reproduces DFT energies and forces and promotes a statistically rigorous sampling workflow may still result in incorrect thermodynamics if small residual biases reorder thermally accessible microstates or distort their Boltzmann weights. This distinction is important because experiments typically resolve composition–temperature phase boundaries and short-range-order trends. These experimental observables depend on collective free-energy competition of various

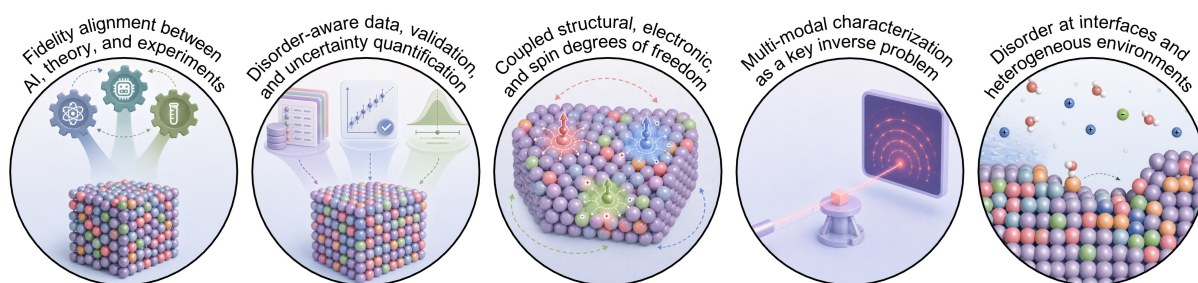


Fig. 8. Grand challenges and future directions for AI-powered modeling of chemically disordered materials. Schematic summary of five key challenges for making AI-driven disorder simulations more predictive, transferable, and experimentally grounded. These vital directions include: (1) aligning AI with statistical-mechanics theory and experimental observables at the free-energy level; (2) developing disorder-aware datasets, validation protocols, and uncertainty estimates to capture realistic local motifs, microstate rankings, and ensemble properties; (3) extending disorder modeling beyond lattice site occupations to coupled structural, charge, and magnetic degrees of freedom; (4) leveraging multi-modal characterization data as an inverse problem for identifying physically plausible disorder ensembles; and (5) expanding disorder modeling to surfaces, interfaces, and heterogeneous environments involving reservoirs, adsorbates, solvents, and dynamically reactive conditions. Taken together, these directions collectively point toward physically robust AI-accelerated workflows that can reliably elucidate, evaluate, control, and optimize thermodynamically meaningful disorder ensembles for various desired material behaviors and properties.

microstates across the entire ensemble, rather than on a single relaxed microstate.

Free-energy fidelity should thus be calibrated at the ensemble level, where small PES errors can be amplified into large phase-level errors. In disordered solids, phase stability is determined by how configurational statistics and finite-temperature corrections jointly transform microstate energetics into experimentally observed thermodynamics. The configurational entropy term sets the statistical weight of competing site-occupancy microstates, while vibrational free energies further shift the stability of various ordered and disordered phases. For instance, first-principles phase-stability analysis of the $\text{Li}_2\text{S}-\text{P}_2\text{S}_5$ system has shown that Li configurational disorder and further vibrational corrections are crucial for reproducing experimental trends.³²² Therefore, the key requirement is not only to predict a local PES, but to learn the finite-temperature free-energy hierarchy that determines which disorder states are the most thermodynamically accessible.

A practical solution is observable-driven calibration, where atomistic ML models are refined against experimentally essential ensemble properties. For molecular simulations, differentiable and reweighting-based strategies have already demonstrated that this idea is technically feasible. Differentiable trajectory reweighting can learn MLIPs directly from thermodynamic, structural, and mechanical observables,³²³ and a similar differentiable molecular MLIP platform has made energies, forces, ensemble averages, and free energies accessible to automatic differentiation.³²⁴ Relevant differentiable simulation approaches have shown that dynamical observables (such as transport and spectroscopic data) can serve as calibration targets.³²⁵ Electrolyte-centered studies have shown a similar principle by demonstrating that bottom-up quantum-chemical training can be facilitated by experimental alignment against macroscopic observables.^{326–328} Although such

examples do not directly study the thermodynamics of chemical disorder, they offer a key lesson for this field: atomistic ML models can remain microscopically grounded while being calibrated against key experimental observables beyond their original energy and force training labels.

For chemically disordered solids, phase diagrams and CALPHAD-derived thermodynamics offer a natural interface for making theory–experiment alignment operational. Rather than using MLIPs only as upstream generators of thermodynamic inputs or leveraging CALPHAD only as a downstream phase-diagram tool, a future workflow should close the loop between them, where MLIPs and other atomistic ML models provide local configurational energetics, relaxations, and short-range-order information, while experimental phase equilibria can constrain whether these atomistic inputs predict the correct phase-level free-energy behaviors.^{226,329} Recent experiment-calibrated uncertainty strategies have sharpened this argument further, as the model uncertainty should be determined not only by how closely an MLIP can reproduce a selected DFT reference, but also how reliably its results reflect experimentally measurable reality.³³⁰ Related simulation-to-experiment distribution-alignment strategies for generative AI models point toward a similar direction by treating the refinement target as an experimentally consistent ensemble, rather than an unconstrained simulation prior.³³¹ In this view, experimental properties of disordered solids should no longer be regarded only as the final validation targets, but as active calibration metrics that can continuously refine atomistic ML models to enable trustworthy disorder prediction.

4.2 Disorder-native data, benchmarks, and uncertainty quantification

Once experimental behaviors become the calibration targets, the next goal is to develop datasets that faithfully represent the disorder ensembles being examined. Critically, dataset construction is not merely a technical task of adding more structures: it is a physical assumption about which microstates, local orderings, distortions, and thermodynamic regimes the AI models are allowed to learn. Existing large-scale databases for materials informatics^{294,332} and MLIP training,^{264–271} together with relevant ML prediction benchmarks,^{262,333,334} have been transformative for general atomistic modeling. Nevertheless, these fundamental resources are not designed specifically for disorder thermodynamics, short-range-order statistics, and finite-temperature behaviors. Recent disorder-focused efforts^{154,236,258,317} have begun to shift toward disorder-aware data construction and benchmark development, but they remain specialized by material families, disorder classes, target properties, and model types, rather than forming a generalized ML training and validation framework for disorder prediction. Future datasets should thus include not only relaxed ordered prototypes, but also symmetrically distinct orderings, short-range-ordering structures, off-lattice relaxations, and other crucial configurations that matter in disordered solids. As such expanded coverage can quickly become combinatorial, disorder-native dataset construction will also need selection strategies that avoid redundant configurations while preserving physically meaningful

local environments. Learned local-environment similarity metrics,^{335,336} for instance, can prune redundant orderings and identify representative supercells for efficient data generation, making disorder-native datasets broader without making their construction too exhaustive.

Disorder-native datasets also require thermodynamically faithful labels, as disorder stability is often controlled by meV/atom-scale free-energy differences. Hence, systematic label bias can be as damaging as missing configurations. An error that appears minor for individual structures may reorder competing microstates, distort Boltzmann weights, and shift predicted short-range-ordering tendencies or phase boundaries. The bias can arise from the choice of DFT functionals, as well as from magnetic initialization, charge-state assignments, relaxation protocols, and other factors.^{3,268,337} Recent thermodynamic workflows^{294,338} and MLIP studies^{339–341} have indicated that multi-fidelity learning can greatly improve thermodynamic consistency across chemistries. For disorder modeling, these strategies can be especially helpful, as broad low-fidelity coverage can be paired with targeted higher-fidelity labels for capturing critical configurations that control ordering and phase stability. Overall, new disorder-native datasets should be judged not only by structural diversity and chemical coverage, but also by whether their labels have enough fidelity for the microstate rankings and free-energy trends that AI models are expected to learn.

Benchmarking efforts for AI-assisted disorder modeling must measure disorder fidelity, not only average prediction errors. Mean absolute errors in energies and forces remain valuable, but they do not necessarily imply whether a model preserves the configurational physics of disorder. This limitation has already appeared in short-range-order-focused MLIP studies.^{256,257} Broader universal MLIP benchmarks similarly show that models can perform well near common training distributions, while failing for defects, migration barriers, and non-equilibrium structures.^{334,342} Future disorder-native benchmarks should thus test microstate rankings, local motif preferences, short-range-order statistics, and ensemble-averaged observables, ideally via cross-regime splits that probe the ML transferability between ordered and disordered structures, random and short-range-ordered states, low- and high-temperature configurations, and simple and compositionally complex systems. Representation-level diagnostics^{343–345} can help reveal whether MLIP models with similar scalar errors encode local motifs and order–disorder relationships differently.

Uncertainty quantification should accompany every step of the disorder modeling workflow. A useful question is whether an AI model is interpolating in the training-set disorder ensembles or extrapolating to unseen chemistries. Recent studies^{346–348} have widely shown that uncertainty is essential for reliable atomistic simulations. For chemically disordered solids, this uncertainty should indicate how confidence levels change when predictions are aggregated from individual microstates into order parameters, free energies, phase boundaries, and macroscopic properties. A useful uncertainty estimate should identify which regions of the configurational ensembles are underrepresented, which label sources may be biased, and which experiments, adversarial stress

tests, and higher-fidelity calculations would reduce ambiguity. Hence, disorder-native datasets, benchmarks, and uncertainty estimates should not be treated as supporting infrastructure, but as qualification criteria that assess when ML predictions are trustworthy for disordered solids.

4.3 Disorder beyond site occupations: defect, charge, and magnetism

In functional materials, site occupations and atomic positions may not always be the full set of degrees of freedom required to faithfully capture chemical disorder. Defects illustrate this point, as vacancies, interstitials, and non-stoichiometry can influence not only which species occupy a parent lattice, but also which lattice sites are available, which local atomic motifs are stable, and which migration pathways are accessible under synthesis and operating conditions.³⁴⁹ This distinction is especially critical for chemically complex solids, where defect formation energies become distributions over local orderings and chemical environments.^{5,194,233,350,351} Recent data-driven approaches for defect energetics^{352–354} and defect-driven structural reconstructions^{355–357} suggest that these processes can increasingly be modeled at larger scales. Future disorder-aware AI models should treat defects as part of the same ensembles as chemical disorder, rather than as isolated perturbations after the substitutional disorder has already been resolved.

Charge orderings and long-range interactions provide a second frontier where the relevant disorder variables are not fully specified by atomic positions and species labels. For instance, in mixed-valence solids, multiple charge-ordering patterns may be compatible with similar nuclear arrangements, and electronic configurational entropy can strongly influence phase behaviors.¹⁶⁰ A recent study has shown that many MLIPs can assign $\text{Fe}^{2+}/\text{Fe}^{3+}$ states in NaFePO_4 incorrectly and lead to erroneous ordering energetics, whereas embedding charge-state information directly into the MLIP representations improves the energetic ranking.²⁸² Charge-informed simulations with MLIPs²⁶⁴ point toward a related direction and have already been useful for modeling phase transformations in mixed-valence battery cathode materials.⁶⁴ More broadly, recent long-range MLIP developments have introduced charge equilibration,^{358,359} latent Ewald summation,^{360–364} and reciprocal-space^{365–368} or attention-based nonlocal representations^{369,370} to model atomistic systems where local disorder controls charge transfer, long-range fields, and dielectric response. These architectures are not, by themselves, disorder sampling frameworks, but they provide key machinery for disorder modeling when charge distribution and polarization are critical.

Magnetism offers a third frontier where the disorder ensembles might include spin variables, moment amplitudes, and spin–lattice coupling in addition to lattice occupations. A lattice-based route has been provided by spin cluster expansions, which extend cluster-expansion formalisms from lattice site occupations to localized spin variables and comprehensively encode exchange, anisotropy, and higher-order magnetic couplings permitted by crystal symmetries.^{371,372} In this physical framework, first-principles energies are mapped onto effective spin Hamiltonians on a

parent lattice,³⁷³ which can be further sampled through Monte Carlo to predict magnetic phase diagrams¹²² and composition-dependent phase boundaries in magnetic alloy systems.^{374,375} The strength of this approach is its interpretability and statistical-mechanics rigor when the magnetic problems map cleanly onto well-defined lattices, but its core limitation emerges when chemical disorder, local relaxation, moment stability, and off-lattice distortions evolve together. To tackle this limitation, recent spin-aware MLIPs^{376–382} and Hamiltonian-learning models^{383,384} push this logic toward continuous atomistic modeling by treating lattice coordinates, magnetic moments, spin–orbit coupling, and electronic-structure Hamiltonians within their learned representations. For disordered magnets, the critical opportunity is thus to move beyond a fixed-lattice magnetic Hamiltonian and toward AI models in which site occupations, relaxations, moment amplitudes, and spin orientations can co-evolve within the same finite-temperature disorder ensembles.

Taken together, defects, charge states, and magnetic variables can expand disorder modeling from a problem of assigning chemical species to lattice sites into a broader problem of sampling coupled structural, electronic, and spin degrees of freedom. The long-term target for disorder simulations is therefore a unified finite-temperature framework in which chemical swaps, defect reactions, atomic relaxations, charge redistribution, long-range electrostatic responses, and spin updates are performed consistently on a shared PES. Such a framework would allow AI-assisted simulations to predict favorable occupational patterns together with defect populations, charge states, and magnetic textures that are physically accessible under realistic conditions.

4.4 Multi-modal characterization as an inverse problem for disorder

The experiment–simulation gap discussed above also makes disorder characterization an inverse problem: rather than predicting experimental results from known atomistic ensembles, one must infer which latent ensembles of atomistic configurations may have led to the measured signals. Different experimental techniques, including diffraction,^{36,74} scattering,^{66,67} spectroscopies,^{68,69} imaging,^{15,21,39} and chemical mapping,⁷⁰ each probe distinct aspects of chemical disorder, such as average symmetries, pair correlations, charge states, and element-specific local coordination environments. Consequently, none of these modalities uniquely determines the full distribution of microscopic microstates on its own. Notably, this non-uniqueness has long been recognized in the neighboring field of structural disorder,^{28–35} where non-crystalline structures are typically derived from complex experimental data through underdetermined inverse problems, rather than reconstructed atom by atom.³⁸⁵ Thus, the central challenge is not only to detect whether disorder exists, but to infer which configurational ensembles are consistent with measurements.

This inverse problem can be tackled through two complementary strategies: forward-model-constrained inference and learned inverse generation. First, for the forward direction, candidate ensembles generated by first-principles atomistic simulations or MLIP-powered configurational

sampling can be translated into predicted experimental observables. This process is important, since experimental signatures are ensemble projections. For instance, cation-disordered rocksalt materials require both short-range order and bond-length relaxation to reproduce experimental pair distribution functions.⁶⁶ While extended X-ray absorption fine structure is locally sensitive, complex concentrated alloys can yield non-unique fits.⁶⁸ Moreover, diffuse electron-diffraction features may not uniquely reveal short-range ordering,^{74–76} but the combination of microscopy, diffraction, and atomistic modeling has recently been shown to better constrain the hidden local motifs.^{21,39,386} Second, for the inverse direction, recently proposed differentiable and generative frameworks have shown how experimental signals can be utilized to refine or generate atomistic structures directly.^{387–394} These inverse-generation demonstrations have centered on ordered and structurally disordered systems, rather than chemically disordered ensembles, but they can offer useful templates for chemical-disorder-specific methods. Together, these tools can generate and eliminate competing ensemble hypotheses for refining against complex multi-modal data.

Beyond inferring and generating candidate structures, AI-driven modeling can help integrate multi-modal measurements into probabilistic constraints on chemical disorder. ML models have been developed to predict or fit complex spectroscopic signatures from atomistic structures and infer structural descriptors from measured spectra.^{395–397} Related methods designed for electron microscopic data can turn large experimental datasets into more quantitative constraints on local structures.^{398,399} More broadly, multi-modal and cross-modality frameworks point toward future workflows in which the combined data streams from diffraction, spectroscopy, and microscopy can be analyzed jointly, rather than regarded as independent evidence.^{400–403} In this setting, AI adds value by propagating constraints across modalities to find the key disorder ensembles.

In summary, AI-driven interpretation of multi-modal experimental data should be regarded as disorder ensemble identification, instead of deterministic reconstruction of a “true” atomistic configuration. Even when a structural model reproduces a diffraction pattern with high apparent agreement with experimental data, recent ML analyses have shown that high spectral similarity does not necessarily guarantee structural correctness.⁴⁰⁴ Therefore, a reliable workflow needs to combine AI inference with uncertainty quantification, thermodynamic constraints, and physical priors, together with robust forward and inverse models that elucidate which structural features are truly identifiable. In this regard, characterization becomes an active component of disorder modeling: simulations supply physically plausible microstates, while AI updates the ensembles toward those most consistent with physical constraints and characterization signatures.

4.5 Beyond bulk disorder: interfaces and heterogeneous environments

Looking ahead, the next stage of disorder modeling must move beyond equilibrium bulk parent lattices toward the heterogeneous environments where interfacial disorder can control material

behaviors and properties. Many functional responses are governed not by the bulk phases alone, but by surfaces, grain boundaries, and hetero-interfaces. These environments break translational symmetries, alter local coordination environments, reshape electrostatics and strains, and create local chemical potentials that can possibly lead to segregation, reconstruction, vacancy ordering, amorphization, and interfacial phases that are absent from the bulk.^{187,312} This issue is especially clear in electrochemistry and heterogeneous catalysis,^{405–407} where surface reconstruction might occur through leaching, corrosion, redeposition, ion insertion, adsorbate-induced restructuring, and dissolution–precipitation equilibria.^{408–410} In these cases, a nominally well-defined material surface or interface is often better understood as a condition-dependent ensemble of metastable states rather than as a single static termination, as discussed in more detail in a recent perspective article on data-driven modeling of electrocatalyst stability and surface reconstruction.¹⁸ Hence, the relevant disorder configurational ensembles should expand from bulk site occupations to the heterogeneous, reactive, and metastable environments in which materials actually function.

At the modeling level, this expansion calls for grand-canonical, reactive, and kinetics-aware treatments of disorder as a coupled ensemble problem. Surface or interfacial disorder depends not only on site occupations, but also on adsorbate coverage, solvent or electrolyte environment, electrochemical potential, and ion exchange with external environments. While first-principles thermodynamic tools, including surface phase⁴¹¹ and Pourbaix diagrams,⁴¹² can provide helpful equilibrium baselines, their predictions are limited by the surface terminations, reconstructions, coverages, and metastable states included in the candidate sets.^{413,414} More fundamentally, these environmental variables can influence the accessible configurational space itself, as atoms may migrate between the bulk and the surface, vacancies may be generated or annihilated, adsorbates or electrolyte species may stabilize otherwise energetically unfavorable motifs, and metastable reconstructions may persist because of kinetic barriers.^{18,415} Therefore, extending bulk disorder modeling methods to heterogeneous environments requires more than larger supercells or more complex occupations on a fixed parent lattice: it requires advanced hybrid on-lattice/off-lattice sampling strategies,^{413,416} MLIPs validated for defective and low-coordination environments,⁴¹⁷ alchemical or ordering-sensitive ML representations for local composition and segregation,^{93,312} and generative AI models that can propose plausible surface microstates beyond human-selected templates.⁴¹⁸ For electrochemical interfaces, these workflows must further account for solvation effects, electrolyte ions, electric fields, and charge-transfer processes,^{419,420} as these parameters might reshape both the thermodynamic stability and kinetic accessibility of interfacial disorder. Thus, the key goal is not simply to sample more configurations, but to identify which disordered motifs are persistent and kinetically reachable under realistic heterogeneous conditions.

Taken together, these grand challenges point toward a broader methodological transition in atomistic disorder modeling. The central goal is no longer only to transform partial occupancies

into tractable configurations, or to accelerate the assessment of many candidate microstates, but to unveil the disorder ensembles that are thermodynamically meaningful, kinetically accessible, experimentally identifiable, and relevant to desired material behaviors and properties. Reaching this target will require AI-accelerated workflows that remain grounded in statistical mechanics, calibrated by experimental observables, qualified by uncertainty estimates, and flexible enough to account for chemical, structural, electronic, magnetic, interfacial, and processing-dependent degrees of freedom. If developed in such a direction, AI will not merely make existing disorder simulations faster: it will help transform chemical disorder from a representational obstacle into a controllable design variable for materials discovery across chemical and functional spaces.

Conflicts of interest

There are no conflicts of interest to declare.

Data availability

No new data were generated or analyzed as part of this Review.

Acknowledgments

J.P. acknowledges the University at Buffalo for offering start-up funds to support this work. P.Z. acknowledges the NUS Presidential Young Professorship start-up funding.

References

1. A. Simonov and A. L. Goodwin, *Nat. Rev. Chem.*, 2020, **4**, 657–673.
2. F. C. Nix and W. Shockley, *Rev. Mod. Phys.*, 1938, **10**, 1–71.
3. J. Peng, J. Damewood and R. Gómez-Bombarelli, *Cell Rep. Phys. Sci.*, 2024, **5**, 101942.
4. S. D. Young, J. Chen, W. Sun, B. R. Goldsmith and G. Pilania, *Chem. Mater.*, 2023, **35**, 5975–5987.
5. X. Zhang, J. Kang and S.-H. Wei, *Nat. Comput. Sci.*, 2023, **3**, 210–220.
6. L. Han, S. Zhu, Z. Rao, C. Scheu, D. Ponge, A. Ludwig, H. Zhang, O. Gutfleisch, H. Hahn, Z. Li and D. Raabe, *Nat. Rev. Mater.*, 2024, **9**, 846–865.
7. W.-L. Hsu, C.-W. Tsai, A.-C. Yeh and J.-W. Yeh, *Nat. Rev. Chem.*, 2024, **8**, 471–485.
8. J. Ding, *Nat. Rev. Mater.*, 2026, **11**, 82–83.
9. S. Kang, S. Lee, H. Lee and Y.-M. Kang, *Nat. Rev. Chem.*, 2024, **8**, 587–604.
10. D. Hirai, *Chem. Mater.*, 2026, **38**, 559–571.
11. K. Jun, Y. Chen, G. Wei, X. Yang and G. Ceder, *Nat. Rev. Mater.*, 2024, **9**, 887–905.
12. V. A. Mints, J. K. Pedersen, J. C. Olsen, M. K. Plenge, M. Arenz and J. Rossmeisl, *J. Am. Chem. Soc.*, 2026, **148**, 4815–4825.
13. S. Chen, Z. H. Aitken, S. Pattamatta, Z. Wu, Z. G. Yu, D. J. Srolovitz, P. K. Liaw and Y.-W. Zhang, *Nat. Commun.*, 2021, **12**, 4953.
14. Y. Zhang, Y. N. Osetsky and W. J. Weber, *Chem. Rev.*, 2022, **122**, 789–829.
15. Z. Lun, B. Ouyang, D.-H. Kwon, Y. Ha, E. E. Foley, T.-Y. Huang, Z. Cai, H. Kim, M. Balasubramanian, Y. Sun, J. Huang, Y. Tian, H. Kim, B. D. McCloskey, W. Yang, R. J. Clément, H. Ji and G. Ceder, *Nat. Mater.*, 2021, **20**, 214–221.
16. Y. Zeng, B. Ouyang, J. Liu, Y.-W. Byeon, Z. Cai, L. J. Miara, Y. Wang and G. Ceder, *Science*, 2022, **378**, 1320–1324.
17. J. Peng, J. K. Damewood, J. Karaguesian, R. Gómez-Bombarelli and Y. Shao-Horn, *Joule*, 2021, **5**, 3069–3071.
18. J. Peng, *J. Chem. Phys.*, 2025, **163**, 040902.

19. K. C. Hass, R. J. Lempert and H. Ehrenreich, *Phys. Rev. Lett.*, 1984, **52**, 77–80.
20. V. V. Sokolovskiy, V. D. Buchelnikov, M. A. Zagrebin, P. Entel, S. Sahoo and M. Ogura, *Phys. Rev. B*, 2012, **86**, 134418.
21. S. Moniri, Y. Yang, J. Ding, Y. Yuan, J. Zhou, L. Yang, F. Zhu, Y. Liao, Y. Yao, L. Hu, P. Ercius and J. Miao, *Nature*, 2023, **624**, 564–569.
22. W. Hume-Rothery, R. Smallman and C. Haworth, *The Structure of Metals and Alloys*, Metals and Metallurgy Trust, London, 1969.
23. M. Zacharias and J. Even, *ACS Energy Lett.*, 2025, **10**, 5635–5643.
24. M. A. Peña and J. L. G. Fierro, *Chem. Rev.*, 2001, **101**, 1981–2018.
25. Y.-T. Cheng and W. L. Johnson, *Science*, 1987, **235**, 997–1002.
26. H. Song, F. Tian, Q.-M. Hu, L. Vitos, Y. Wang, J. Shen and N. Chen, *Phys. Rev. Mater.*, 2017, **1**, 023404.
27. J. P. Barber, W. J. Deary, A. N. Titus, G. R. Bejger, S. S. I. Almishal and C. M. Rost, *Mater. Horiz.*, 2025, **12**, 10453–10477.
28. D. A. Drabold, *Eur. Phys. J. B*, 2009, **68**, 1–21.
29. P. Biswas, D. N. Tafen, F. Inam, B. Cai and D. A. Drabold, *J. Phys. Condens. Matter*, 2009, **21**, 084207.
30. L. Berthier and G. Biroli, *Rev. Mod. Phys.*, 2011, **83**, 587–645.
31. E. B. Jones and V. Stevanović, *npj Comput. Mater.*, 2020, **6**, 56.
32. L. Berthier and D. R. Reichman, *Nat. Rev. Phys.*, 2023, **5**, 102–116.
33. Y. Liu, A. Madanchi, A. S. Anker, L. Simine and V. L. Deringer, *Nat. Rev. Mater.*, 2025, **10**, 228–241.
34. L. Wolf, A. Novick and V. Stevanović, *J. Appl. Phys.*, 2025, **137**, 095101.
35. A. Madanchi, E. Azek, K. Zongo, L. K. Béland, N. Mousseau and L. Simine, *ACS Phys. Chem. Au*, 2025, **5**, 3–16.
36. N. Schlegel, S. Punke, C. M. Clausen, U. Friis-Jensen, A. F. Sapnik, D. Stoian, O. Aalling-Frederiksen, D. Gautam, J. Rossmeisl, R. K. Pittkowski, M. Arenz and K. M. Ø. Jensen, *Chem. Mater.*, 2025, **37**, 939–953.

37. B. C. Wyatt, Y. Yang, P. P. Michałowski, T. Parker, Y. Morency, F. Urban, G. Kadagishvili, M. Tanwar, S. P. Muhoza, S. K. Nemani, A. Bedford, H. Fang, Z. D. Hood, J. Jang, K. Kamath, B. G. Wright, R. Disko, A. Thakur, S. Han, N. Ghosh, X. Xu, Z. Fakhraai, Y. Gogotsi, A. Vojvodic, D.-e. Jiang and B. Anasori, *Science*, 2025, **389**, 1054–1058.
38. Z. Huang, T. Li, B. Li, Q. Dong, J. Smith, S. Li, L. Xu, G. Wang, M. Chi and L. Hu, *J. Am. Chem. Soc.*, 2024, **146**, 2167–2173.
39. L. M. Vogl, S. Chen, P. Schweizer, X. Jin, S.-Q. Yu, J. Liu, T. Li and A. M. Minor, *Science*, 2025, **389**, 1342–1346.
40. Y. P. Wang, B. S. Li and H. Z. Fu, *Adv. Eng. Mater.*, 2009, **11**, 641–644.
41. M. Cui, C. Yang, S. Hwang, M. Yang, S. Overa, Q. Dong, Y. Yao, A. H. Brozena, D. A. Cullen, M. Chi, T. F. Blum, D. Morris, Z. Finfrock, X. Wang, P. Zhang, V. G. Goncharov, X. Guo, J. Luo, Y. Mo, F. Jiao and L. Hu, *Sci. Adv.*, 2022, **8**, eabm4322.
42. H. Wang, Q.-F. He and Y. Yang, *Rare Met.*, 2022, **41**, 1989–2001.
43. Z. Liu and L. Zhang, *J. Alloys Compd.*, 2024, **981**, 173716.
44. X. Chen, Q. Wang, Z. Cheng, M. Zhu, H. Zhou, P. Jiang, L. Zhou, Q. Xue, F. Yuan, J. Zhu, X. Wu and E. Ma, *Nature*, 2021, **592**, 712–716.
45. W. Chen, L. Li, Q. Zhu and H. Zhuang, *MRS Bull.*, 2023, **48**, 762–768.
46. Z. Pei, Y. Gong, P. Singh, Y. Li, F. Körmann, Q. Xie, K. Wang, X. Wu, S. Mu, M. C. Gao, P. K. Liaw, Y. Tong, F. Zhang, Y. Wang and R. Li, *Curr. Opin. Solid State Mater. Sci.*, 2026, **41**, 101254.
47. A. Ferrari, F. Körmann, M. Asta and J. Neugebauer, *Nat. Comput. Sci.*, 2023, **3**, 221–229.
48. P. Ekborg-Tanner, P. Rosander, E. Fransson and P. Erhart, *PRX Energy*, 2024, **3**, 042001.
49. L. J. Santodonato, P. K. Liaw, R. R. Unocic, H. Bei and J. R. Morris, *Nat. Commun.*, 2018, **9**, 4520.
50. M. Brahlek, M. Gazda, V. Keppens, A. R. Mazza, S. J. McCormack, A. Mielewczyk-Gryń, B. Musico, K. Page, C. M. Rost, S. B. Sinnott, C. Toher, T. Z. Ward and A. Yamamoto, *APL Mater.*, 2022, **10**, 110902.
51. S. S. Aamlid, M. Oudah, J. Rottler and A. M. Hallas, *J. Am. Chem. Soc.*, 2023, **145**, 5991–6006.

52. W. L. Bragg and E. J. Williams, *Proc. R. Soc. London. A. Math. Phys. Sci.*, 1934, **145**, 699–730.
53. W. L. Bragg and E. J. Williams, *Proc. R. Soc. London. A. Math. Phys. Sci.*, 1935, **151**, 540–566.
54. E. J. Williams, *Proc. R. Soc. London. A. Math. Phys. Sci.*, 1935, **152**, 231–252.
55. C. Toher, C. Oses, D. Hicks and S. Curtarolo, *npj Comput. Mater.*, 2019, **5**, 69.
56. D. Dey, L. Liang and L. Yu, *J. Am. Chem. Soc.*, 2024, **146**, 5142–5151.
57. S. S. I. Almishal, M. Furst, Y. Tan, J. T. Sivak, G. Bejger, J. Petruska, S. V. G. Ayyagari, D. Srikanth, N. Alem, C. M. Rost, S. B. Sinnott, L.-Q. Chen and J.-P. Maria, *Nat. Commun.*, 2025, **16**, 8211.
58. J. T. Sivak, S. S. I. Almishal, M. K. Caucci, Y. Tan, D. Srikanth, J. Petruska, M. Furst, L.-Q. Chen, C. M. Rost, J.-P. Maria and S. B. Sinnott, *Phys. Rev. Lett.*, 2025, **134**, 216101.
59. O. A. Dicks, S. S. Aamlid, A. M. Hallas and J. Rottler, *Comput. Mater. Sci.*, 2026, **267**, 114581.
60. B. Xing, T. J. Rupert, X. Pan and P. Cao, *Nat. Commun.*, 2024, **15**, 3879.
61. Y. Han, H. Chen, Y. Sun, J. Liu, S. Wei, B. Xie, Z. Zhang, Y. Zhu, M. Li, J. Yang, W. Chen, P. Cao and Y. Yang, *Nat. Commun.*, 2024, **15**, 6486.
62. V. P. Bacurau, P. A. F. P. Moreira, G. Bertoli, A. F. Andreoli, E. Mazzer, F. F. de Assis, P. Gargarella, G. Koga, G. C. Stumpf, S. J. A. Figueroa, M. Widom, M. Kaufman, A. Fantin, Y. Cao, R. Freitas, D. Miracle and F. G. Coury, *Nat. Commun.*, 2024, **15**, 7815.
63. M. Islam, K. Sheriff, Y. Cao and R. Freitas, *Nat. Commun.*, 2025, **16**, 8926.
64. P. Zhong, B. Deng, S. Anand, T. Mishra and G. Ceder, *Phys. Rev. Mater.*, 2025, **9**, 105404.
65. H. Chun, H. Tang, B. Xing, R. Gomez-Bombarelli and J. Li, *Preprint at arXiv*, 2025, 10.48550/arXiv.2411.17839.
66. N. J. Szymanski, Z. Lun, J. Liu, E. C. Self, C. J. Bartel, J. Nanda, B. Ouyang and G. Ceder, *Chem. Mater.*, 2023, **35**, 4922–4934.
67. H. Deng, J.-Y. Qi, Q.-H. Xia, J. Li and X. Zhang, *Preprint at arXiv*, 2025, 10.48550/arXiv.2506.05684.

68. H. Joress, B. Ravel, E. Anber, J. Hollenbach, D. Sur, J. Hatrick-Simpers, M. L. Taheri and B. DeCost, *Matter*, 2023, **6**, 3763–3781.
69. D. Morris, Y. Yao and P. Zhang, *ACS Nano*, 2026, **20**, 8959–8970.
70. M. He, W. J. Davids, A. J. Breen and S. P. Ringer, *Nat. Mater.*, 2024, **23**, 1200–1207.
71. J. M. Cowley, *Phys. Rev.*, 1950, **77**, 669–675.
72. N. Norman and B. E. Warren, *J. Appl. Phys.*, 1951, **22**, 483–486.
73. D. Raabe, J. R. Mianroodi and J. Neugebauer, *Nat. Comput. Sci.*, 2023, **3**, 198–209.
74. F. G. Coury, C. Miller, R. Field and M. Kaufman, *Nature*, 2023, **622**, 742–747.
75. F. Walsh, M. Zhang, R. O. Ritchie, A. M. Minor and M. Asta, *Nat. Mater.*, 2023, **22**, 926–929.
76. F. Walsh, M. Zhang, R. O. Ritchie, M. Asta and A. M. Minor, *Sci. Adv.*, 2024, **10**, eadn9673.
77. E. C.-Y. Yuan, Y. Liu, J. Chen, P. Zhong, S. Raja, T. Kreiman, S. Vargas, W. Xu, M. Head-Gordon, C. Yang, S. M. Blau, B. Cheng, A. Krishnapriyan and T. Head-Gordon, *Nat. Rev. Chem.*, 2026, **10**, 212–230.
78. H. Metni, L. Ruple, L. N. Walters, L. Torresi, J. Teufel, H. Schopmans, J. Östreicher, Y. Zhang, M. Neubert, Y. Koide, K. Steiner, P. Link, L. Bär, M. Petrova, G. Ceder and P. Friederich, *Adv. Mater.*, 2026, **38**, e23620.
79. J. Peng, D. Schwalbe-Koda, K. Akkiraju, T. Xie, L. Giordano, Y. Yu, C. J. Eom, J. R. Lunger, D. J. Zheng, R. R. Rao, S. Muy, J. C. Grossman, K. Reuter, R. Gómez-Bombarelli and Y. Shao-Horn, *Nat. Rev. Mater.*, 2022, **7**, 991–1009.
80. A. K. Cheetham and R. Seshadri, *Chem. Mater.*, 2024, **36**, 3490–3495.
81. L. Nordheim, *Ann. Phys.*, 1931, **401**, 607–640.
82. P. Soven, *Phys. Rev.*, 1967, **156**, 809–813.
83. L. Kaufman and H. Bernstein, *Computer Calculation of Phase Diagrams with Special Reference to Refractory Metals*, Academic Press, New York, 1970.
84. J. M. Sanchez, F. Ducastelle and D. Gratias, *Phys. A*, 1984, **128**, 334–350.

85. A. van de Walle, M. Asta and G. Ceder, *Calphad*, 2002, **26**, 539–553.
86. M. Ångqvist, W. A. Muñoz, J. M. Rahm, E. Fransson, C. Durniak, P. Rozyczko, T. H. Rod and P. Erhart, *Adv. Theory Simul.*, 2019, **2**, 1900015.
87. L. Barroso-Luque, P. Zhong, J. H. Yang, F. Xie, T. Chen, B. Ouyang and G. Ceder, *Phys. Rev. B*, 2022, **106**, 144202.
88. A. Zunger, S.-H. Wei, L. G. Ferreira and J. E. Bernard, *Phys. Rev. Lett.*, 1990, **65**, 353–356.
89. S.-H. Wei, L. G. Ferreira, J. E. Bernard and A. Zunger, *Phys. Rev. B*, 1990, **42**, 9622–9649.
90. K. Yang, C. Oses and S. Curtarolo, *Chem. Mater.*, 2016, **28**, 6484–6492.
91. R. Singh, A. Sharma, P. Singh, G. Balasubramanian and D. D. Johnson, *Nat. Comput. Sci.*, 2021, **1**, 54–61.
92. N. Lopanitsyna, G. Fraux, M. A. Springer, S. De and M. Ceriotti, *Phys. Rev. Mater.*, 2023, **7**, 045802.
93. J. Peng, J. Damewood, J. Karaguesian, J. R. Lunger and R. Gómez-Bombarelli, *Preprint at arXiv*, 2024, 10.48550/arXiv.2409.13851.
94. M. H. Petersen, R. Zhu, H. Dai, S. Aggarwal, W. Nong, A. P. Chen, A. Bhowmik, J. M. Garcia-Lastra and K. Hippalgaonkar, *Preprint at arXiv*, 2025, 10.48550/arXiv.2507.18275.
95. J. Nam, J. Peng and R. Gómez-Bombarelli, *Nat. Commun.*, 2025, **16**, 4350.
96. S. Divilov, H. Eckert, S. D. Thiel, S. D. Griesemer, R. Friedrich, N. H. Anderson, M. J. Mehl, D. Hicks, M. Esters, N. Hotz, X. Campilongo, A. Calzolari and S. Curtarolo, *High Entropy Alloys Mater.*, 2025, **3**, 178–187.
97. N. J. Ramer and A. M. Rappe, *Phys. Rev. B*, 2000, **62**, R743–R746.
98. C. Eckhardt, K. Hummer and G. Kresse, *Phys. Rev. B*, 2014, **89**, 165201.
99. L. Bellaiche and D. Vanderbilt, *Phys. Rev. B*, 2000, **61**, 7877–7882.
100. B. Winkler, C. Pickard and V. Milman, *Chem. Phys. Lett.*, 2002, **362**, 266–270.
101. J. Íñiguez, D. Vanderbilt and L. Bellaiche, *Phys. Rev. B*, 2003, **67**, 224107.

102. B. T. Payne, M. Juelsholt, M. A. Pérez-Osorio, D. L. R. Melvin, G. J. Cuello, E. Suard, D. J. M. Irving, N. H. Rees, M. Feavioir, E. Petrucco, S. P. Day, G. J. Rees and P. G. Bruce, *Energy Environ. Sci.*, 2025, **18**, 8876–8888.
103. F. Yonezawa and K. Morigaki, *Prog. Theor. Phys. Suppl.*, 1973, **53**, 1–76.
104. P. Soven, *Phys. Rev. B*, 1970, **2**, 4715–4722.
105. H. Shiba, *Prog. Theor. Phys.*, 1971, **46**, 77–94.
106. D. D. Johnson, D. M. Nicholson, F. J. Pinski, B. L. Gyorffy and G. M. Stocks, *Phys. Rev. Lett.*, 1986, **56**, 2088–2091.
107. D. D. Johnson, D. M. Nicholson, F. J. Pinski, B. L. Györffy and G. M. Stocks, *Phys. Rev. B*, 1990, **41**, 9701–9716.
108. P. Singh, A. V. Smirnov and D. D. Johnson, *Phys. Rev. B*, 2015, **91**, 224204.
109. B. L. Gyorffy, *Phys. Rev. B*, 1972, **5**, 2382–2384.
110. P. L. Alcázar Ruano, D. Martínez, O. Arroyo-Gascón, Y. Baba, J. Quereda and F. Domínguez-Adame, *Phys. Rev. B*, 2025, **112**, 064204.
111. D. A. Rowlands, X.-G. Zhang and A. Gonis, *Phys. Rev. B*, 2008, **78**, 115119.
112. D. Chandler, *Introduction to Modern Statistical Mechanics*, Oxford University Press, New York, 1987.
113. A. van de Walle and G. Ceder, *Rev. Mod. Phys.*, 2002, **74**, 11–45.
114. G. Ceder, *Comput. Mater. Sci.*, 1993, **1**, 144–150.
115. G. D. Garbulsky and G. Ceder, *Phys. Rev. B*, 1994, **49**, 6327–6330.
116. G. D. Garbulsky, *PhD thesis*, Massachusetts Institute of Technology, 1996.
117. A. Van der Ven, *PhD thesis*, Massachusetts Institute of Technology, 2000.
118. D. B. Laks, L. G. Ferreira, S. Froyen and A. Zunger, *Phys. Rev. B*, 1992, **46**, 12587–12605.
119. N. A. Zarkevich and D. D. Johnson, *Phys. Rev. Lett.*, 2004, **92**, 255702.
120. J. M. Sanchez, *Phys. Rev. B*, 2010, **81**, 224202.
121. J.-Z. Xie, X.-Y. Zhou and H. Jiang, *J. Chem. Phys.*, 2022, **157**, 200901.

122. B. Puchala, J. C. Thomas, A. R. Natarajan, J. G. Goiri, S. S. Behara, J. L. Kaufman and A. Van der Ven, *Comput. Mater. Sci.*, 2023, **217**, 111897.
123. L. Barroso-Luque and G. Ceder, *npj Comput. Mater.*, 2024, **10**, 158.
124. J. M. Sanchez, *Phys. Rev. B*, 2019, **99**, 134206.
125. P. D. Tepesch, G. D. Garbulsky and G. Ceder, *Phys. Rev. Lett.*, 1995, **74**, 2272–2275.
126. A. Seko, Y. Koyama and I. Tanaka, *Phys. Rev. B*, 2009, **80**, 165122.
127. A. van de Walle, *Calphad*, 2009, **33**, 266–278.
128. X. Zhang and M. H. F. Sluiter, *J. Phase Equilib. Diffus.*, 2016, **37**, 44–52.
129. L. Barroso-Luque, J. H. Yang and G. Ceder, *Phys. Rev. B*, 2021, **104**, 224203.
130. S. Rigamonti, M. Troppenz, M. Kuban, A. Hübner and C. Draxl, *npj Comput. Mater.*, 2024, **10**, 195.
131. T. Mueller and G. Ceder, *Phys. Rev. B*, 2009, **80**, 024103.
132. L. J. Nelson, V. Ozoliņš, C. S. Reese, F. Zhou and G. L. W. Hart, *Phys. Rev. B*, 2013, **88**, 155105.
133. P. Zhong, T. Chen, L. Barroso-Luque, F. Xie and G. Ceder, *Phys. Rev. B*, 2022, **106**, 024203.
134. W. Huang, A. Urban, Z. Rong, Z. Ding, C. Luo and G. Ceder, *npj Comput. Mater.*, 2017, **3**, 30.
135. B. Ouyang, T. Chakraborty, N. Kim, N. H. Perry, T. Mueller, N. R. Aluru and E. Ertekin, *Chem. Mater.*, 2019, **31**, 3144–3153.
136. H. Ji, A. Urban, D. A. Kitchaev, D.-H. Kwon, N. Artrith, C. Ophus, W. Huang, Z. Cai, T. Shi, J. C. Kim, H. Kim and G. Ceder, *Nat. Commun.*, 2019, **10**, 592.
137. A. van de Walle and G. Ceder, *J. Phase Equilib.*, 2002, **23**, 348.
138. K. Wang, D. Cheng, C.-L. Fu and B.-C. Zhou, *Phys. Rev. Mater.*, 2020, **4**, 013606.
139. D. Cheng, K. Wang and B.-C. Zhou, *Acta Mater.*, 2023, **242**, 118443.
140. F. Xie, P. Zhong, L. Barroso-Luque, B. Ouyang and G. Ceder, *Comput. Mater. Sci.*, 2023, **218**, 112000.

141. C. Wolverton and A. Zunger, *Phys. Rev. Lett.*, 1998, **81**, 606–609.
142. T. Chen, J. Yang, L. Barroso-Luque and G. Ceder, *ACS Energy Lett.*, 2023, **8**, 314–319.
143. X. Guo, C. Chen and S. P. Ong, *Chem. Mater.*, 2023, **35**, 1537–1546.
144. C.-L. Fu, R. P. Gorrey and B.-C. Zhou, *Acta Mater.*, 2024, **277**, 120138.
145. A. Roy, K. Sieradzki, M. J. Waters, J. M. Rondinelli and I. McCue, *Scr. Mater.*, 2026, **274**, 117137.
146. T.-c. Liu, S. B. Torrisi and C. Wolverton, *Small*, 2026, **22**, e14811.
147. S. S. Aamlid, S. Mugiraneza, M. U. González-Rivas, G. King, A. M. Hallas and J. Rottler, *Chem. Mater.*, 2024, **36**, 9636–9645.
148. P. Zhong, S. Gupta, B. Deng, K. Jun and G. Ceder, *ACS Energy Lett.*, 2024, **9**, 2775–2781.
149. L. Huang, P. Zhong, Y. Ha, Z. Cai, Y.-W. Byeon, T.-Y. Huang, Y. Sun, F. Xie, H.-M. Hau, H. Kim, M. Balasubramanian, B. D. McCloskey, W. Yang and G. Ceder, *Adv. Energy Mater.*, 2023, **13**, 2202345.
150. P. Zhong, Z. Cai, Y. Zhang, R. Giovine, B. Ouyang, G. Zeng, Y. Chen, R. Clément, Z. Lun and G. Ceder, *Chem. Mater.*, 2020, **32**, 10728–10736.
151. J. H. Yang, T. Chen, L. Barroso-Luque, Z. Jadidi and G. Ceder, *npj Comput. Mater.*, 2022, **8**, 133.
152. P. Zhong, F. Xie, L. Barroso-Luque, L. Huang and G. Ceder, *PRX Energy*, 2023, **2**, 043005.
153. Y. L. Müller and A. R. Natarajan, *npj Comput. Mater.*, 2025, **11**, 60.
154. L. Wang, B. Shen, Z.-D. He, Z. Ye, Y. Zeng, C. A. Mirkin and B. Ouyang, *Nat. Commun.*, 2026, **17**, 3093.
155. R. Drautz, *Phys. Rev. B*, 2019, **99**, 014104.
156. J. P. Darby, D. P. Kovács, I. Batatia, M. A. Caro, G. L. W. Hart, C. Ortner and G. Csányi, *Phys. Rev. Lett.*, 2023, **131**, 028001.
157. I. Vorotnikov, F. Romashov, N. Rybin, M. Rakhuba and I. S. Novikov, *J. Chem. Phys.*, 2025, **163**, 244112.

158. V. Blum and A. Zunger, *Phys. Rev. B*, 2004, **70**, 155108.
159. K. Wang, D. Cheng and B.-C. Zhou, *npj Comput. Mater.*, 2023, **9**, 75.
160. F. Zhou, T. Maxisch and G. Ceder, *Phys. Rev. Lett.*, 2006, **97**, 155704.
161. A. van de Walle, P. Tiwary, M. de Jong, D. L. Olmsted, M. Asta, A. Dick, D. Shin, Y. Wang, L.-Q. Chen and Z.-K. Liu, *Calphad*, 2013, **42**, 13–18.
162. A. P. Kadzielawa, *Preprint at arXiv*, 2026, 10.48550/arXiv.2602.10872.
163. C. Jiang, C. Wolverton, J. Sofo, L.-Q. Chen and Z.-K. Liu, *Phys. Rev. B*, 2004, **69**, 214202.
164. D. Shin, R. Arróyave, Z.-K. Liu and A. de Walle, *Phys. Rev. B*, 2006, **74**, 024204.
165. Z. Jiang, Y. Nahas, B. Xu, S. Prosandeev, D. Wang and L. Bellaiche, *J. Phys. Condens. Matter*, 2016, **28**, 475901.
166. M. C. Gao, C. Niu, C. Jiang and D. L. Irving, in *Applications of Special Quasi-random Structures to High-Entropy Alloys*, ed. M. C. Gao, J.-W. Yeh, P. K. Liaw and Y. Zhang, Springer, Cham, 2016, pp. 333–368.
167. D. Gehringer, M. Friák and D. Holec, *Comput. Phys. Commun.*, 2023, **286**, 108664.
168. J.-C. Lian, L. Li, G.-F. Huang, W. Hu and W.-Q. Huang, *Phys. Rev. B*, 2025, **111**, 224207.
169. M. Lebeda, J. Drahokoupil, P. Vlčák, Š. Svoboda and A. van de Walle, *J. Comput. Sci.*, 2026, **96**, 102846.
170. T.-c. Liu, A. Salgado-Casanova, S. Yubuchi, B. Baldassarri, M. Aykol, J. Yoshida, H. Yamasaki, Y. Zhu, S. B. Torrisi and C. Wolverton, *Adv. Energy Mater.*, 2025, **15**, e03660.
171. L. Wang, Y. Wang, J. Martin, E. Scivally, Z. He, D.-h. Kim, D.-h. Yeon, Y. Zeng, D. Chen and B. Ouyang, *EES Batter.*, 2025, **1**, 1731–1739.
172. T. Schuler, M. Nastar, K. Li and C.-C. Fu, *Acta Mater.*, 2024, **276**, 120074.
173. K. Li, T. Schuler, C.-C. Fu and M. Nastar, *Acta Mater.*, 2024, **281**, 120355.
174. A. Seko and I. Tanaka, *Phys. Rev. B*, 2015, **91**, 024106.
175. J. Liu, M. V. Fernández-Serra and P. B. Allen, *Phys. Rev. B*, 2016, **93**, 054207.

176. R. Grau-Crespo, S. Hamad, C. R. A. Catlow and N. H. de Leeuw, *J. Phys. Condens. Matter*, 2007, **19**, 256201.
177. G. L. W. Hart and R. W. Forcade, *Phys. Rev. B*, 2008, **77**, 224115.
178. K. Okhotnikov, T. Charpentier and S. Cadars, *J. Cheminform.*, 2016, **8**, 17.
179. P. Sarker, T. Harrington, C. Toher, C. Oses, M. Samiee, J.-P. Maria, D. W. Brenner, K. S. Vecchio and S. Curtarolo, *Nat. Commun.*, 2018, **9**, 4980.
180. S. Divilov, H. Eckert, D. Hicks, C. Oses, C. Toher, R. Friedrich, M. Esters, M. J. Mehl, A. C. Zettel, Y. Lederer, E. Zurek, J.-P. Maria, D. W. Brenner, X. Campilongo, S. Filipović, W. G. Fahrenholtz, C. J. Ryan, C. M. DeSalle, R. J. Creales, D. E. Wolfe, A. Calzolari and S. Curtarolo, *Nature*, 2024, **625**, 66–73.
181. M. Esters, C. Oses, D. Hicks, M. J. Mehl, M. Jahnátek, M. D. Hossain, J.-P. Maria, D. W. Brenner, C. Toher and S. Curtarolo, *Nat. Commun.*, 2021, **12**, 5747.
182. A. Calzolari, C. Oses, C. Toher, M. Esters, X. Campilongo, S. P. Stepanoff, D. E. Wolfe and S. Curtarolo, *Nat. Commun.*, 2022, **13**, 5993.
183. M. Esters, A. Smolyanyuk, C. Oses, D. Hicks, S. Divilov, H. Eckert, X. Campilongo, C. Toher and S. Curtarolo, *Acta Mater.*, 2023, **245**, 118594.
184. C. Toher, C. Oses, M. Esters, D. Hicks, G. N. Kotsonis, C. M. Rost, D. W. Brenner, J.-P. Maria and S. Curtarolo, *MRS Bull.*, 2022, **47**, 194–202.
185. C. Jiang and B. P. Uberuaga, *Phys. Rev. Lett.*, 2016, **116**, 105501.
186. V. Sorkin, T. L. Tan, Z. G. Yu and Y. W. Zhang, *Comput. Mater. Sci.*, 2021, **188**, 110213.
187. H. H. Kristoffersen and J. Rossmeisl, *J. Phys. Chem. C*, 2022, **126**, 6782–6790.
188. A. Novick, Q. Nguyen, R. Garnett, E. Toberer and V. Stevanović, *Phys. Rev. Mater.*, 2023, **7**, 063801.
189. M. C. Kuner, E. Rothchild, M. D. Asta and D. C. Chrzan, *Comput. Mater. Sci.*, 2024, **238**, 112924.
190. R. F. Moran, D. McKay, P. C. Tornstrom, A. Aziz, A. Fernandes, R. Grau-Crespo and S. E. Ashbrook, *J. Am. Chem. Soc.*, 2019, **141**, 17838–17846.
191. J. Liao, H. Chen, Y. Xie, Z. Li, S. Tan, S. Zhou, L. Jiang, X. Zhang, M. Liu, Y.-B. He, F. Kang, Z. Lun, S. Zhao and T. Hou, *Adv. Energy Mater.*, 2025, **15**, 2501857.

192. P. Shi, Y. Yang, B. Yao, J. Si and Y. Wang, *Nanoscale Adv.*, 2024, **6**, 3793–3800.
193. A. Roy, K. Sieradzki, J. M. Rondinelli and I. D. McCue, *Phys. Rev. B*, 2024, **110**, 085420.
194. H. Tang, H. Chun, R. Gomez-Bombarelli, Y. Mishin and J. Li, *Preprint at arXiv*, 2025, 10.48550/arXiv.2512.22370.
195. X. Jin, S. Chen and T. Li, *Phys. Rev. Mater.*, 2021, **5**, 104606.
196. N. Oyeniran and C. Hu, *Preprint at arXiv*, 2026, 10.48550/arXiv.2602.17889.
197. S. Kirkpatrick, C. D. Gelatt and M. P. Vecchi, *Science*, 1983, **220**, 671–680.
198. K. Hukushima and K. Nemoto, *J. Phys. Soc. Japan*, 1996, **65**, 1604–1608.
199. D. J. Earl and M. W. Deem, *Phys. Chem. Chem. Phys.*, 2005, **7**, 3910–3916.
200. S. Kasamatsu and O. Sugino, *J. Phys. Condens. Matter*, 2019, **31**, 085901.
201. K. Zhu, E. Trizio, J. Zhang, R. Hu, L. Jiang, T. Hou and L. Bonati, *Chem. Rev.*, 2026, **126**, 671–713.
202. E. C. Neyts and A. Bogaerts, *Theor. Chem. Acc.*, 2012, **132**, 1320.
203. T. D. Doležal, E. Tekoglu, J.-S. Bae, G.-D. Sim, R. Freitas and J. Li, *Comput. Mater. Sci.*, 2025, **253**, 113858.
204. X. Xu, K. Cai and P. Xie, *Preprint at arXiv*, 2025, 10.48550/arXiv.2511.11097.
205. D. J. Wales and J. P. K. Doye, *J. Phys. Chem. A*, 1997, **101**, 5111–5116.
206. Y. Zhang, Z. Li, Z.-K. Han and R. Ouyang, *J. Chem. Theory Comput.*, 2024, **20**, 6971–6979.
207. S. Goedecker, *J. Chem. Phys.*, 2004, **120**, 9911–9917.
208. A. Talapatra, R. Arróyave, P. Entel, I. Valencia-Jaime and A. H. Romero, *Phys. Rev. B*, 2015, **92**, 054107.
209. T. C. Le and D. A. Winkler, *Chem. Rev.*, 2016, **116**, 6107–6132.
210. J. Dean, M. J. Cowan, J. Estes, M. Ramadan and G. Mpourmpakis, *ACS Nano*, 2020, **14**, 8171–8180.
211. C. E. Mohn and W. Kob, *Comput. Mater. Sci.*, 2009, **45**, 111–117.

212. G. Anand, *Mater. Manuf. Process.*, 2023, **38**, 2044–2050.
213. P.-W. Guan, C. D. Spataru, V. Stavila, R. Jones, P. A. Sharma and M. D. Witman, *PRX Energy*, 2025, **4**, 033013.
214. Z. Fang, T.-W. Hsu and Q. Yan, *ACS Nano*, 2025, **19**, 37353–37363.
215. X. Liu, K. Yang, F. Zhou and P. Xu, *J. Chem. Theory Comput.*, 2025, **21**, 12784–12795.
216. X. Liu, K. Yang, Y. Liu, F. Zhou, D. Fan, Z. Pei, P. Xu and Y. Tian, *npj Comput. Mater.*, 2025, **11**, 267.
217. C. Niu and L. Liu, *Comput. Mater. Sci.*, 2025, **253**, 113792.
218. B. Camino, J. Buckeridge, N. Chancellor, C. R. A. Catlow, A. M. Ferrari, P. A. Warburton, A. A. Sokol and S. M. Woodley, *Sci. Adv.*, 2025, **11**, eadt7156.
219. W. Chen, A. Hilhorst, G. Bokas, S. Gorsse, P. J. Jacques and G. Hautier, *Nat. Commun.*, 2023, **14**, 2856.
220. H. Lukas, S. G. Lukas and B. Sundman, *Computational Thermodynamics: The Calphad Method*, Cambridge University Press, New York, 2007.
221. I. Ansara, N. Dupin, H. L. Lukas and B. Sundman, *J. Alloys Compd.*, 1997, **247**, 20–30.
222. A. van de Walle, R. Sun, Q.-J. Hong and S. Kadkhodaei, *Calphad*, 2017, **58**, 70–81.
223. Y. Lederer, C. Toher, K. S. Vecchio and S. Curtarolo, *Acta Mater.*, 2018, **159**, 364–383.
224. C. Shen, *Comput. Mater. Sci.*, 2025, **258**, 113970.
225. S. Zhu, D. Saritürk and R. Arróyave, *npj Comput. Mater.*, 2025, **11**, 340.
226. S. Zhu, D. Saritürk and R. Arróyave, *Acta Mater.*, 2025, **286**, 120747.
227. C. Kunselman, S. Zhu, D. Saritürk and R. Arróyave, *J. Phase Equilib. Diffus.*, 2025, 10.1007/s11669-025-01222-2.
228. P. Friederich, F. Häse, J. Proppe and A. Aspuru-Guzik, *Nat. Mater.*, 2021, **20**, 750–761.
229. O. T. Unke, S. Chmiela, H. E. Sauceda, M. Gastegger, I. Poltavsky, K. T. Schütt, A. Tkatchenko and K.-R. Müller, *Chem. Rev.*, 2021, **121**, 10142–10186.
230. T. W. Ko and S. P. Ong, *Nat. Comput. Sci.*, 2023, **3**, 998–1000.

231. B. Kalita, H. Gokcan and O. Isayev, *Nat. Comput. Sci.*, 2025, **5**, 1120–1132.
232. J. Liu, P. Wang, J. Luan, J. Chen, P. Cai, J. Chen, X. Lu, Y. Fan, Z. Yu and K. Chou, *J. Chem. Theory Comput.*, 2024, **20**, 11082–11092.
233. S. A. Ibrahim, J. Yang, T. Shi, C. Zhang, D. Chen, J. Li, Y. Li, J. C. Mbazor, Y. Zhang, Z. Su and C. Lu, *J. Phys. Chem. C*, 2026, **130**, 4538–4553.
234. C. Chen, Y. Zuo, W. Ye, X. Li and S. P. Ong, *Nat. Comput. Sci.*, 2021, **1**, 46–53.
235. H. Zhang, R. Huang, J. Chen, J. M. Rondinelli and W. Chen, *Mach. Learn.: Sci. Technol.*, 2025, **6**, 025005.
236. L. Wang, T. He and B. Ouyang, *ACS Mater. Lett.*, 2025, **7**, 2708–2715.
237. G. Deshmukh, N. J. Wichrowski, N. Evangelou, P. G. Ghanekar, S. Deshpande, I. G. Kevrekidis and J. Greeley, *npj Comput. Mater.*, 2024, **10**, 116.
238. Z. Fang and Q. Yan, *npj Comput. Mater.*, 2024, **10**, 91.
239. J. Behler and M. Parrinello, *Phys. Rev. Lett.*, 2007, **98**, 146401.
240. A. P. Bartók, M. C. Payne, R. Kondor and G. Csányi, *Phys. Rev. Lett.*, 2010, **104**, 136403.
241. T. Xie and J. C. Grossman, *Phys. Rev. Lett.*, 2018, **120**, 145301.
242. C. Chen, W. Ye, Y. Zuo, C. Zheng and S. P. Ong, *Chem. Mater.*, 2019, **31**, 3564–3572.
243. J. Damewood, J. Karaguesian, J. R. Lunger, A. R. Tan, M. Xie, J. Peng and R. Gómez-Bombarelli, *Annu. Rev. Mater. Res.*, 2023, **53**, 399–426.
244. G. Corso, H. Stark, S. Jegelka, T. Jaakkola and R. Barzilay, *Nat. Rev. Methods Primers*, 2024, **4**, 17.
245. J. R. Lunger, J. Karaguesian, H. Chun, J. Peng, Y. Tseo, C. H. Shan, B. Han, Y. Shao-Horn and R. Gómez-Bombarelli, *npj Comput. Mater.*, 2024, **10**, 80.
246. K. T. Schütt, H. E. Saucedo, P.-J. Kindermans, A. Tkatchenko and K.-R. Müller, *J. Chem. Phys.*, 2018, **148**, 241722.
247. J. Gasteiger, C. Yeshwanth and S. Günnemann, *Advances in Neural Information Processing Systems*, 2021, pp. 15421–15433.
248. C. W. Park, M. Kornbluth, J. Vandermause, C. Wolverton, B. Kozinsky and J. P. Mailoa, *npj Comput. Mater.*, 2021, **7**, 73.

249. T. E. Smidt, *Trends Chem.*, 2021, **3**, 82–85.
250. S. Batzner, A. Musaelian, L. Sun, M. Geiger, J. P. Mailoa, M. Kornbluth, N. Molinari, T. E. Smidt and B. Kozinsky, *Nat. Commun.*, 2022, **13**, 2453.
251. I. Batatia, D. P. Kovacs, G. Simm, C. Ortner and G. Csanyi, *Advances in Neural Information Processing Systems*, 2022, pp. 11423–11436.
252. A. Duval, S. V. Mathis, C. K. Joshi, V. Schmidt, S. Miret, F. D. Malliaros, T. Cohen, P. Lio, Y. Bengio and M. Bronstein, *Preprint at arXiv*, 2023, 10.48550/arXiv.2312.07511.
253. I. Batatia, S. Batzner, D. P. Kovács, A. Musaelian, G. N. C. Simm, R. Drautz, C. Ortner, B. Kozinsky and G. Csányi, *Nat. Mach. Intell.*, 2025, **7**, 56–67.
254. M. Wen, M. K. Horton, J. M. Munro, P. Huck and K. A. Persson, *Digit. Discov.*, 2024, **3**, 869–882.
255. W. Yan, X. Lai, Y. Chen, W. Zhang, J. Wu and X. Xu, *J. Am. Chem. Soc.*, 2025, **147**, 47044–47056.
256. K. Sheriff, D. Xiao, Y. Cao, L. R. Owen and R. Freitas, *Preprint at arXiv*, 2025, 10.48550/arXiv.2506.12592.
257. Y. Cao, K. Sheriff and R. Freitas, *npj Comput. Mater.*, 2025, **11**, 268.
258. K. Li, K. Choudhary, B. DeCost, M. Greenwood and J. Hattract-Simpers, *J. Mater. Chem. A*, 2024, **12**, 12412–12422.
259. S. Chen, X. Jin, W. Zhao and T. Li, *Phys. Rev. Mater.*, 2024, **8**, 043805.
260. L. An, H. Ma, J. Liu, W. Guo and X. Wen, *npj Comput. Mater.*, 2025, **11**, 226.
261. V. Choyal, N. Sagar and G. Sai Gautam, *J. Chem. Theory Comput.*, 2024, **20**, 4844–4856.
262. J. Riebesell, R. E. A. Goodall, P. Benner, Y. Chiang, B. Deng, G. Ceder, M. Asta, A. A. Lee, A. Jain and K. A. Persson, *Nat. Mach. Intell.*, 2025, **7**, 836–847.
263. Y. Liu, J. Wang, H. Deng, Y. Sun, X.-Q. Chen and P. Liu, *Preprint at arXiv*, 2025, 10.48550/arXiv.2510.16697.
264. B. Deng, P. Zhong, K. Jun, J. Riebesell, K. Han, C. J. Bartel and G. Ceder, *Nat. Mach. Intell.*, 2023, **5**, 1031–1041.

265. A. Merchant, S. Batzner, S. S. Schoenholz, M. Aykol, G. Cheon and E. D. Cubuk, *Nature*, 2023, **624**, 80–85.
266. J. Schmidt, T. F. T. Cerqueira, A. H. Romero, A. Loew, F. Jäger, H.-C. Wang, S. Botti and M. A. L. Marques, *Mater. Today Phys.*, 2024, **48**, 101560.
267. L. Barroso-Luque, M. Shuaibi, X. Fu, B. M. Wood, M. Dzamba, M. Gao, A. Rizvi, C. L. Zitnick and Z. W. Ulissi, *Preprint at arXiv*, 2025, 10.48550/arXiv.2410.12771.
268. A. D. Kaplan, R. Liu, J. Qi, T. W. Ko, B. Deng, J. Riebesell, G. Ceder, K. A. Persson and S. P. Ong, *Preprint at arXiv*, 2025, 10.48550/arXiv.2503.04070.
269. A. Mazitov, S. Chorna, G. Fraux, M. Bercx, G. Pizzi, S. De and M. Ceriotti, *Sci. Data*, 2025, **12**, 1857.
270. D. S. Levine, M. Shuaibi, E. W. C. Spotte-Smith, M. G. Taylor, M. R. Hasyim, K. Michel, I. Batatia, G. Csányi, M. Dzamba, P. Eastman, N. C. Frey, X. Fu, V. Gharakhanyan, A. S. Krishnapriyan, J. A. Rackers, S. Raja, A. Rizvi, A. S. Rosen, Z. Ulissi, S. Vargas, C. L. Zitnick, S. M. Blau and B. M. Wood, *Preprint at arXiv*, 2026, 10.48550/arXiv.2505.08762.
271. C. Malosso, F. Bigi, P. Pegolo, J. W. Abbott, P. Loche, M. Rossi, M. Ceriotti and A. Mazitov, *Preprint at arXiv*, 2026, 10.48550/arXiv.2603.02089.
272. J. Choi, G. Nam, J. Choi and Y. Jung, *JACS Au*, 2025, **5**, 1499–1518.
273. C. Chen and S. P. Ong, *Nat. Comput. Sci.*, 2022, **2**, 718–728.
274. D. Zhang, X. Liu, X. Zhang, C. Zhang, C. Cai, H. Bi, Y. Du, X. Qin, A. Peng, J. Huang, B. Li, Y. Shan, J. Zeng, Y. Zhang, S. Liu, Y. Li, J. Chang, X. Wang, S. Zhou, J. Liu, X. Luo, Z. Wang, W. Jiang, J. Wu, Y. Yang, J. Yang, M. Yang, F.-Q. Gong, L. Zhang, M. Shi, F.-Z. Dai, D. M. York, S. Liu, T. Zhu, Z. Zhong, J. Lv, J. Cheng, W. Jia, M. Chen, G. Ke, W. E, L. Zhang and H. Wang, *npj Comput. Mater.*, 2024, **10**, 293.
275. C. M. Clausen, J. Rossmeisl and Z. W. Ulissi, *J. Phys. Chem. C*, 2024, **128**, 11190–11195.
276. I. Batatia, P. Benner, Y. Chiang, A. M. Elena, D. P. Kovács, J. Riebesell, X. R. Advincula, M. Asta, M. Avaylon, W. J. Baldwin, F. Berger, N. Bernstein, A. Bhowmik, F. Bigi, S. M. Blau, V. Cărare, M. Ceriotti, S. Chong, J. P. Darby, S. De, F. Della Pia, V. L. Deringer, R. Elijošius, Z. El-Machachi, E. Fako, F. Falcioni, A. C. Ferrari, J. L. A. Gardner, M. J. Gawkowski, A. Genreith-Schriever, J. George, R. E. A. Goodall, J. Grandel, C. P. Grey, P. Grigorev, S. Han, W. Handley, H. H. Heenen, K. Hermansson, C. H. Ho, S. Hofmann,

- C. Holm, J. Jaafar, K. S. Jakob, H. Jung, V. Kapil, A. D. Kaplan, N. Karimitari, J. R. Kermode, P. Kourtis, N. Kroupa, J. Kullgren, M. C. Kuner, D. Kuryla, G. Liepuoniute, C. Lin, J. T. Margraf, I.-B. Magdău, A. Michaelides, J. H. Moore, A. A. Naik, S. P. Niblett, S. W. Norwood, N. O'Neill, C. Ortner, K. A. Persson, K. Reuter, A. S. Rosen, L. A. M. Rosset, L. L. Schaaf, C. Schran, B. X. Shi, E. Sivonxay, T. K. Stenczel, C. Sutton, V. Svahn, T. D. Swinburne, J. Tilly, C. van der Oord, S. Vargas, E. Varga-Umbrich, T. Vegge, M. Vondrák, Y. Wang, W. C. Witt, T. Wolf, F. Zills and G. Csányi, *J. Chem. Phys.*, 2025, **163**, 184110.
277. A. Mazitov, F. Bigi, M. Kellner, P. Pegolo, D. Tisi, G. Fraux, S. Pozdnyakov, P. Loche and M. Ceriotti, *Nat. Commun.*, 2025, **16**, 10653.
278. B. Wood, M. Dzamba, X. Fu, M. Gao, M. Shuaibi, L. Barroso-Luque, K. Abdelmaqsoud, V. Gharakhanyan, J. Kitchin, D. Levine, K. Michel, A. Sriram, T. Cohen, A. Das, S. Sahoo, A. Rizvi, Z. Ulissi and L. Zitnick, *Advances in Neural Information Processing Systems*, 2025, pp. 129391–129427.
279. M. Biswas, R. Desai, G. Bidna and A. Mannodi-Kanakithodi, *J. Chem. Inf. Model.*, 2026, **66**, 1353–1370.
280. R. S. Ullberg, J. D. Langhout, M. M. Butala and S. R. Phillpot, *ACS Appl. Energy Mater.*, 2026, **9**, 3703–3715.
281. K. S. Jakob, R. Marschall, K. Reuter and J. T. Margraf, *Preprint at ChemRxiv*, 2026, 10.26434/chemrxiv.15002514/v1.
282. M. H. Petersen, S. Lysgaard, A. Bhowmik, K. Hippalgaonkar and J. M. G. Lastra, *Preprint at arXiv*, 2026, 10.48550/arXiv.2603.26471.
283. B. He, Z. Lai, D. Wang, X. Liu, Y. Liu, M. Xu, B. Pu, Q. Wang, R. Wang, M. Avdeev and S. Shi, *Acta Mater.*, 2026, **302**, 121628.
284. S. Han and S. De, *Preprint at ChemRxiv*, 2025, 10.26434/chemrxiv-2025-19gnz-v2.
285. F. Zhou, H. Chen, P. Xu, K. Yang, Z. Pei and X. Liu, *Preprint at arXiv*, 2026, 10.48550/arXiv.2603.21207.
286. K. Sheriff, Y. Cao, T. Smidt and R. Freitas, *Proc. Natl. Acad. Sci.*, 2024, **121**, e2322962121.
287. M. Islam, K. Sheriff and R. Freitas, *Acta Mater.*, 2026, **306**, 121838.

288. S. Wei, M. W. Qureshi, J. Wei, L. Liu, X. Hu, J. Xi, S. Attarian, R. Su, H. Zhang, E. Willing, X. Wang, K. Sridharan, P. M. Voyles, J. H. Perepezko and I. Szlufarska, *Nat. Commun.*, 2026, **17**, 2362.
289. A. Aspuru-Guzik and V. Bernales, *Polyhedron*, 2025, **281**, 117707.
290. A. Vriza, U. Kornu, A. Koneru, H. Chan and S. K. R. S. Sankaranarayanan, *Digit. Discov.*, 2026, **5**, 440–452.
291. G. Liu, S. Yang and Y. Zhong, *Digit. Discov.*, 2026, 10.1039/D6DD00043F.
292. S. G. H. Kumar, Y. Zou, A. Wang, J. Valdés-Hernández, T. W. Ko, N. Yue, O. Leng, H. Xu, C. Crebolder, A. Aspuru-Guzik and V. Bernales, *Preprint at arXiv*, 2026, 10.48550/arXiv.2602.17886.
293. H. Xin, J. R. Kitchin and H. J. Kulik, *Nat. Mach. Intell.*, 2025, **7**, 1373–1375.
294. M. K. Horton, P. Huck, R. X. Yang, J. M. Munro, S. Dwaraknath, A. M. Ganose, R. S. Kingsbury, M. Wen, J. X. Shen, T. S. Mathis, A. D. Kaplan, K. Berket, J. Riebesell, J. George, A. S. Rosen, E. W. C. Spotte-Smith, M. J. McDermott, O. A. Cohen, A. Dunn, M. C. Kuner, G.-M. Rignanese, G. Petretto, D. Waroquiers, S. M. Griffin, J. B. Neaton, D. C. Chrzan, M. Asta, G. Hautier, S. Cholia, G. Ceder, S. P. Ong, A. Jain and K. A. Persson, *Nat. Mater.*, 2025, **24**, 1522–1532.
295. C. Chen, D. T. Nguyen, S. J. Lee, N. A. Baker, A. S. Karakoti, L. Lauw, C. Owen, K. T. Mueller, B. A. Bilodeau, V. Murugesan and M. Troyer, *J. Am. Chem. Soc.*, 2024, **146**, 20009–20018.
296. C. Zeni, R. Pinsler, D. Zügner, A. Fowler, M. Horton, X. Fu, Z. Wang, A. Shysheya, J. Crabbé, S. Ueda, R. Sordillo, L. Sun, J. Smith, B. Nguyen, H. Schulz, S. Lewis, C.-W. Huang, Z. Lu, Y. Zhou, H. Yang, H. Hao, J. Li, C. Yang, W. Li, R. Tomioka and T. Xie, *Nature*, 2025, **639**, 624–632.
297. P.-P. De Breuck, H.-C. Wang, G.-M. Rignanese, S. Botti and M. A. L. Marques, *npj Comput. Mater.*, 2025, **11**, 370.
298. D. Antypov, C. M. Collins, M. S. Dyer, J. B. Claridge and M. J. Rosseinsky, *J. Appl. Crystallogr.*, 2025, **58**, 659–677.
299. K. S. Jakob, A. Walsh, K. Reuter and J. T. Margraf, *Adv. Mater.*, 2026, **38**, e14226.
300. D. B. McHaffie, Z. W. B. Iton, J. M. Bienz, F. A. L. Laskowski and K. A. See, *Digit. Discov.*, 2025, **4**, 1518–1533.

301. Y. Huang, W. Nong, S. Yamazaki, M. H. Petersen, J. Wang, R. Zhu and K. Hippalgaonkar, *Preprint at arXiv*, 2026, 10.48550/arXiv.2604.17994.
302. A. R. Falkowski and T. D. Sparks, *Digit. Discov.*, 2025, **4**, 1833–1843.
303. M. Martirosyan, T. Egg, P. Höllmer, G. Karypis, M. Transtrum, A. Roitberg, M. Liu, R. Hennig, E. Tadmor and S. Martiniani, *Advances in Neural Information Processing Systems*, 2025.
304. P. Hagemann, S. Müller, J. George and P. Benner, *Preprint at arXiv*, 2025, 10.48550/arXiv.2512.09514.
305. M. Negishi, H. Park, K. O. Mastej and A. Walsh, *Preprint at arXiv*, 2026, 10.48550/arXiv.2510.12405.
306. S. Yamazaki, Y. Huang, M. H. Petersen, W. Nong and K. Hippalgaonkar, *Preprint at arXiv*, 2026, 10.48550/arXiv.2604.21386.
307. M. Juelsholt, *Mater. Horiz.*, 2026, 10.1039/D6MH00268D.
308. K. Sheriff, Y. Cao and R. Freitas, *npj Comput. Mater.*, 2024, **10**, 215.
309. P. Zhong, X. Dai, B. Deng, G. Ceder and K. A. Persson, *Mater. Horiz.*, 2025, **12**, 9669–9678.
310. A. P. Bartók, R. Kondor and G. Csányi, *Phys. Rev. B*, 2013, **87**, 184115.
311. M. J. Willatt, F. Musil and M. Ceriotti, *Phys. Chem. Chem. Phys.*, 2018, **20**, 29661–29668.
312. A. Mazitov, M. A. Springer, N. Lopanitsyna, G. Fraux, S. De and M. Ceriotti, *J. Phys. Mater.*, 2024, **7**, 025007.
313. F. Ekström Kelvinius, O. B. Andersson, A. S. Parackal, D. Qian, R. Armiento and F. Lindsten, *Proceedings of the 42nd International Conference on Machine Learning*, 2025, pp. 15130–15147.
314. A. Belsky, M. Hellenbrandt, V. L. Karen and P. Luksch, *Acta Crystallogr. Sect. B*, 2002, **58**, 364–369.
315. M. Hellenbrandt, *Crystallogr. Rev.*, 2004, **10**, 17–22.
316. L. Wu, R. Jiao, Q. Li, M. Li, S. Li, S. Jin and W. Huang, *Preprint at arXiv*, 2026, 10.48550/arXiv.2602.04734.

317. A. X. B. Yong, T. Su and E. Ertekin, *Digit. Discov.*, 2024, **3**, 1889–1909.
318. J. Damewood, D. Schwalbe-Koda and R. Gómez-Bombarelli, *npj Comput. Mater.*, 2022, **8**, 61.
319. X. Du, J. Nam, S. Liu and R. Gómez-Bombarelli, *Preprint at arXiv*, 2026, 10.48550/arXiv.2603.14695.
320. M. J. Karcz, L. Messina, E. Kawasaki and E. Bourasseau, *Sci. Rep.*, 2026, **16**, 14568.
321. G. Henkelman, H. Jónsson, T. Lelièvre, N. Mousseau and A. F. Voter, *Handbook of Materials Modeling: Methods: Theory and Modeling*, Springer International Publishing, Cham, 2020, pp. 825–834.
322. R. L. Kam, K. Jun, L. Barroso-Luque, J. H. Yang, F. Xie and G. Ceder, *Chem. Mater.*, 2023, **35**, 9111–9126.
323. S. Thaler and J. Zavadlav, *Nat. Commun.*, 2021, **12**, 6884.
324. X. Wang, J. Li, L. Yang, F. Chen, Y. Wang, J. Chang, J. Chen, W. Feng, L. Zhang and K. Yu, *J. Chem. Theory Comput.*, 2023, **19**, 5897–5909.
325. B. Han and K. Yu, *Nat. Commun.*, 2025, **16**, 816.
326. S. Gong, Y. Zhang, Z. Mu, Z. Pu, H. Wang, X. Han, Z. Yu, M. Chen, T. Zheng, Z. Wang, L. Chen, Z. Yang, X. Wu, S. Shi, W. Gao, W. Yan and L. Xiang, *Nat. Mach. Intell.*, 2025, **7**, 543–552.
327. Z. Yang, Y. Wu, X. Han, Z. Zhang, H. Lai, Z. Mu, T. Zheng, S. Liu, Z. Pu, Z. Wang, Z. Yu, S. Gong and W. Yan, *Nat. Mach. Intell.*, 2026, **8**, 186–196.
328. X. Wang, J. Chen, Z. Zhu and P. Zhong, *Preprint at arXiv*, 2026, 10.48550/arXiv.2604.07979.
329. R. L. Kam, S. Wang and G. Ceder, *Preprint at arXiv*, 2026, 10.48550/arXiv.2603.17263.
330. M. Kellner, T. Hansen, T. Bligaard, K. W. Jacobsen and M. Ceriotti, *Preprint at arXiv*, 2026, 10.48550/arXiv.2604.24607.
331. K. Nelson, T. Kreiman, S. Levine and A. S. Krishnapriyan, *Preprint at arXiv*, 2026, 10.48550/arXiv.2604.01169.
332. S. Kirklin, J. E. Saal, B. Meredig, A. Thompson, J. W. Doak, M. Aykol, S. Rühl and C. Wolverton, *npj Comput. Mater.*, 2015, **1**, 15010.

333. A. Dunn, Q. Wang, A. Ganose, D. Dopp and A. Jain, *npj Comput. Mater.*, 2020, **6**, 138.
334. Y. Chiang, T. Kreiman, C. Zhang, M. C. Kuner, E. J. Weaver, I. Amin, H. Park, Y. Lim, J. Kim, D. Chrzan, A. Walsh, S. M. Blau, M. Asta and A. S. Krishnapriyan, The Thirty-Ninth Annual Conference on Neural Information Processing Systems Datasets and Benchmarks Track, 2026.
335. B. Cheng, R.-R. Griffiths, S. Wengert, C. Kunkel, T. Stenczel, B. Zhu, V. L. Deringer, N. Bernstein, J. T. Margraf, K. Reuter and G. Csanyi, *Acc. Chem. Res.*, 2020, **53**, 1981–1991.
336. J. Qi, T. W. Ko, B. C. Wood, T. A. Pham and S. P. Ong, *npj Comput. Mater.*, 2024, **10**, 43.
337. T. Warford, F. L. Thiemann and G. Csányi, *Preprint at arXiv*, 2026, 10.48550/arXiv.2601.21056.
338. R. S. Kingsbury, A. S. Rosen, A. S. Gupta, J. M. Munro, S. P. Ong, A. Jain, S. Dwaraknath, M. K. Horton and K. A. Persson, *npj Comput. Mater.*, 2022, **8**, 195.
339. T. W. Ko and S. P. Ong, *npj Comput. Mater.*, 2025, **11**, 65.
340. J. Kim, J. Kim, J. Kim, J. Lee, Y. Park, Y. Kang and S. Han, *J. Am. Chem. Soc.*, 2025, **147**, 1042–1054.
341. J. Kim, J. You, Y. Park, Y. Lim, Y. Kang, J. Kim, H. Jeon, S. Ju, D. Hong, S. Y. Lee, S. Choi, Y. Kim, J. W. Lee and S. Han, *Nat. Commun.*, 2026, **17**, 3432.
342. B. Deng, Y. Choi, P. Zhong, J. Riebesell, S. Anand, Z. Li, K. Jun, K. A. Persson and G. Ceder, *npj Comput. Mater.*, 2025, **11**, 9.
343. S. Edamadaka, S. Yang, J. Li and R. Gómez-Bombarelli, *Preprint at arXiv*, 2025, 10.48550/arXiv.2512.03750.
344. S. Chorna, D. Tisi, C. Malosso, W. B. How, M. Ceriotti and S. Chong, *Adv. Intell. Syst.*, 2026, 10.1002/aisy.202501497.
345. Z. Li and A. Walsh, *Nat. Mach. Intell.*, 2026, 10.1038/s42256-026-01235-7.
346. J. Dai, S. Adhikari and M. Wen, *Rev. Chem. Eng.*, 2025, **41**, 333–357.
347. F. Grasselli, S. Chong, V. Kapil, S. Bonfanti and K. Rossi, *Digit. Discov.*, 2025, **4**, 2654–2675.

348. T. Frömbgen, E. Surzhikova, J. Dölz, J. Proppe, B. Kirchner and C. R. Jacob, *Chem. Rev.*, 2026, **126**, 4189–4236.
349. A. Klein and D. Sudarikov, *Phys. Chem. Chem. Phys.*, 2025, **27**, 6390–6399.
350. C. R. DeSilva, M. D. Witman and D. R. Trinkle, *Phys. Rev. Mater.*, 2025, **9**, 125801.
351. A. Potter, Y. Wang, K. Hamkins, D. Kong, Y. Li, J. Qin and X. Zheng, *Nat. Commun.*, 2026, 10.1038/s41467-026-70835-z.
352. M. D. Witman, A. Goyal, T. Ogitsu, A. H. McDaniel and S. Lany, *Nat. Comput. Sci.*, 2023, **3**, 675–686.
353. B. Baldassarri, J. He, A. Gopakumar, S. Griesemer, A. J. A. Salgado-Casanova, T.-C. Liu, S. B. Torrisi and C. Wolverton, *Chem. Mater.*, 2023, **35**, 10619–10634.
354. L. Way, C. D. Spataru, R. E. Jones, D. R. Trinkle, A. J. E. Rowberg, J. B. Varley, R. B. Wexler, C. M. Smyth, T. C. Douglas, S. R. Bishop, E. J. Fuller, A. H. McDaniel, S. Lany and M. D. Witman, *Chem. Mater.*, 2025, **37**, 6473–6484.
355. I. Mosquera-Lois, S. R. Kavanagh, A. M. Ganose and A. Walsh, *npj Comput. Mater.*, 2024, **10**, 121.
356. Z. Yang, X. Liu, X. Zhang, P. Huang, K. S. Novoselov and L. Shen, *npj Comput. Mater.*, 2025, **11**, 229.
357. X. Wang, I. Mosquera-Lois and A. Walsh, *Preprint at arXiv*, 2026, 10.48550/arXiv.2603.05238.
358. T. W. Ko, J. A. Finkler, S. Goedecker and J. Behler, *Nat. Commun.*, 2021, **12**, 398.
359. R. Gao, C. Yam, J. Mao, S. Chen, G. Chen and Z. Hu, *Nat. Commun.*, 2025, **16**, 10484.
360. B. Cheng, *npj Comput. Mater.*, 2025, **11**, 80.
361. D. S. King, D. Kim, P. Zhong and B. Cheng, *Nat. Commun.*, 2025, **16**, 8763.
362. D. Kim, X. Wang, S. Vargas, P. Zhong, D. S. King, T. J. Inizan and B. Cheng, *J. Chem. Theory Comput.*, 2025, **21**, 12709–12724.
363. P. Zhong, D. Kim, D. S. King and B. Cheng, *npj Comput. Mater.*, 2025, **11**, 384.
364. D. Kim and B. Cheng, *J. Chem. Phys.*, 2026, **164**, 60901.

365. H. Ramasubramanian, A. Vazquez-Mayagoitia, G. Sivaraman and A. C. Thakur, *Preprint at arXiv*, 2025, 10.48550/arXiv.2510.13055.
366. Y. Ji, J. Liang and Z. Xu, *Phys. Rev. Lett.*, 2025, **135**, 178001.
367. R. Guo, H. Yu, L. Hong, S. Chen, X. Gong and H. Xiang, *Phys. Rev. B*, 2026, **113**, 174101.
368. L. Zhang, T. Cui, D. Zhou, L. Bai, S. Zhang, L. Rossi, M. Su, W. Ouyang and P.-A. Heng, *Preprint at arXiv*, 2026, 10.48550/arXiv.2603.18389.
369. J. T. Frank, S. Chmiela, K.-R. Müller and O. T. Unke, *Nat. Mach. Intell.*, 2026, **8**, 388–402.
370. E. Qu, B. M. Wood, A. S. Krishnapriyan and Z. W. Ulissi, *Preprint at arXiv*, 2026, 10.48550/arXiv.2603.06567.
371. J. C. Thomas and A. Van der Ven, *J. Mech. Phys. Solids*, 2017, **107**, 76–95.
372. J. C. Thomas, J. S. Bechtel and A. Van der Ven, *Phys. Rev. B*, 2018, **98**, 094105.
373. X. Li, H. Yu, F. Lou, J. Feng, M.-H. Whangbo and H. Xiang, *Molecules*, 2021, **26**, 803.
374. D. A. Kitchaev, E. C. Schueller and A. Van der Ven, *Phys. Rev. B*, 2020, **101**, 054409.
375. D. A. Kitchaev and A. Van der Ven, *Phys. Rev. Mater.*, 2021, **5**, 124408.
376. T. S. Kostiuchenko, A. V. Shapeev and I. S. Novikov, *Chin. Phys. Lett.*, 2024, **41**, 66101.
377. H. Yu, Y. Zhong, L. Hong, C. Xu, W. Ren, X. Gong and H. Xiang, *Phys. Rev. B*, 2024, **109**, 144426.
378. H. Yu, B. Liu, Y. Zhong, L. Hong, J. Ji, C. Xu, X. Gong and H. Xiang, *Phys. Rev. B*, 2024, **110**, 104427.
379. T. Yang, Z. Cai, Z. Huang, W. Tang, R. Shi, A. Godfrey, H. Liu, Y. Lin, C.-W. Nan, M. Ye, L. Zhang, K. Wang, H. Wang and B. Xu, *Phys. Rev. B*, 2024, **110**, 064427.
380. W. Xu, R. Y. Sanspeur, A. Kolluru, B. Deng, P. Harrington, S. Farrell, K. Reuter and J. R. Kitchin, *Proc. Natl. Acad. Sci.*, 2025, **122**, e2422973122.
381. D. Zheng, X. Peng, Y. Huang, Y. Wang, D. Zhang, Z. Huang, Z. Cai, L. Zhang, M. Chen, B. Xu and W. Zhou, *npj Comput. Mater.*, 2026, **12**, 52.

382. C. H. Ho, C. van der Oord, J. P. Darby, T. Keane, R. L. Benson, C. R. Espinoza, R. Kulkarni, E. Spinu, M. Papanikolaou, R. Tomsett, R. M. Forrest, J. J. Bean, G. Csányi and C. Ortner, *Preprint at arXiv*, 2026, 10.48550/arXiv.2604.08143.
383. Y. Zhong, H. Yu, M. Su, X. Gong and H. Xiang, *npj Comput. Mater.*, 2023, **9**, 182.
384. Y. Zhong, R. Wang, X. Gong and H. Xiang, *Nat. Mach. Intell.*, 2026, **8**, 403–414.
385. M. J. Cliffe, M. T. Dove, D. A. Drabold and A. L. Goodwin, *Phys. Rev. Lett.*, 2010, **104**, 125501.
386. A. Attiaoui, S. Chen, J. C. Woicik, J. Z. Lentz, L. M. Vogl, J. E. Meyer, K. Mukherjee, A. Minor, T. Li and P. C. McIntyre, *Preprint at arXiv*, 2026, 10.48550/arXiv.2603.27876.
387. H. Kwon, T. Hsu, W. Sun, W. Jeong, F. Aydin, J. Chapman, X. Chen, V. Lordi, M. R. Carbone, D. Lu, F. Zhou and T. Anh Pham, *Mach. Learn.: Sci. Technol.*, 2024, **5**, 45037.
388. G. Guo, J. Goldfeder, L. Lan, A. Ray, A. H. Yang, B. Chen, S. J. L. Billinge and H. Lipson, *npj Comput. Mater.*, 2024, **10**, 209.
389. E. A. Riesel, T. Mackey, H. Nilforoshan, M. Xu, C. K. Badding, A. B. Altman, J. Leskovec and D. E. Freedman, *J. Am. Chem. Soc.*, 2024, **146**, 30340–30348.
390. Q. Lai, F. Xu, L. Yao, Z. Gao, S. Liu, H. Wang, S. Lu, D. He, L. Wang, L. Zhang, C. Wang and G. Ke, *Adv. Sci.*, 2025, **12**, 2410722.
391. G. Guo, T. L. Saidi, M. W. Terban, M. Valsecchi, S. J. L. Billinge and H. Lipson, *Nat. Mater.*, 2025, **24**, 1726–1734.
392. Q. Li, R. Jiao, L. Wu, T. Zhu, W. Huang, S. Jin, Y. Liu, H. Weng and X. Chen, *Nat. Commun.*, 2025, **16**, 7428.
393. A. S. Anker, J. L. A. Gardner, L. A. M. Rosset, A. L. Goodwin and V. L. Deringer, *Preprint at arXiv*, 2026, 10.48550/arXiv.2510.05938.
394. J. Guo and D. Schwalbe-Koda, *Preprint at arXiv*, 2026, 10.48550/arXiv.2603.23210.
395. S. R. Kharel, F. Meng, X. Qu, M. R. Carbone and D. Lu, *Phys. Rev. Mater.*, 2025, **9**, 043803.
396. K. Kulaev, B. Protsenko, W. Cheng, Q. Liu, D. Gorbunov, M. Lifar, V. Vlasenko, A. Burlov, S. Guda, A. Guda, M. Soldatov and A. Soldatov, *J. Phys. Chem. Lett.*, 2026, **17**, 4190–4199.

397. V. F. Grizzi, L. N. Pretzie, J. Xu and C. Liu, *Preprint at arXiv*, 2026, 10.48550/arXiv.2604.12140.
398. S. R. Spurgeon, C. Ophus, L. Jones, A. Petford-Long, S. V. Kalinin, M. J. Olszta, R. E. Dunin-Borkowski, N. Salmon, K. Hattar, W.-C. D. Yang, R. Sharma, Y. Du, A. Chiaramonti, H. Zheng, E. C. Buck, L. Kovarik, R. L. Penn, D. Li, X. Zhang, M. Murayama and M. L. Taheri, *Nat. Mater.*, 2021, **20**, 274–279.
399. P. A. Crozier, M. Leibovich, P. Haluai, M. Tan, A. M. Thomas, J. Vincent, S. Mohan, A. Marcos Morales, S. A. Kulkarni, D. S. Matteson, Y. Wang and C. Fernandez-Granda, *Science*, 2025, **387**, 949–954.
400. T. Na Narong, Z. N. Zachko, S. B. Torrisi and S. J. L. Billinge, *npj Comput. Mater.*, 2025, **11**, 98.
401. Y. Zhu and L. F. Tadesse, *Matter*, 2026, **9**, 102434.
402. A. A. Corrao, P. M. Maffettone, B. Ravel, T. A. Caswell, S. I. Campbell, H. Joress, S. Wilkins and D. Olds, *Preprint at arXiv*, 2026, 10.48550/arXiv.2509.22959.
403. A. C. Johnson, C. Fajardo, L. Sansguiri, W. Ye and S. B. Torrisi, *Preprint at arXiv*, 2026, 10.48550/arXiv.2603.06011.
404. N. Segal, A. Subramanian, M. Li, B. K. Miller and R. Gómez-Bombarelli, *Digit. Discov.*, 2026, **5**, 1590–1599.
405. D. J. Zheng, J. Peng, K. McCormack, H. Xu, J. S. Kang, Z. Wang, Z. Ren, J. Li, Y. Román-Leshkov and Y. Shao-Horn, *EES Catal.*, 2024, **2**, 1186–1209.
406. H. Xin, J. R. Kitchin, N. López, N. M. Schweitzer, N. Artrith, F. Che, L. C. Grabow, G. T. K. K. Gunasooriya, H. J. Kulik, T. Laino, H. Li, S. Linic, A. J. Medford, R. J. Meyer, J. Peng, C. Phillips, J. Qian, L. Qi, W. J. Shaw, Z. W. Ulissi, S. Wang and X. Wang, *Nat. Catal.*, 2026, **9**, 102–111.
407. D. Zhang, Y. Chen, C. Liu, Y. Liu, H. Xin, J. Peng, P. Ou and H. Li, *Angew. Chem. Int. Ed.*, 2026, **65**, e26150.
408. J. Peng, L. Giordano, T. C. Davenport and Y. Shao-Horn, *Chem. Mater.*, 2022, **34**, 7774–7787.
409. T.-H. Shen, L. Spillane, J. Peng, Y. Shao-Horn and V. Tileli, *Nat. Catal.*, 2022, **5**, 30–36.

410. J. Peng, J. J. Giner-Sanz, L. Giordano, W. P. Mounfield, G. M. Leverick, Y. Yu, Y. Román-Leshkov and Y. Shao-Horn, *Joule*, 2023, **7**, 150–167.
411. K. Reuter and M. Scheffler, *Phys. Rev. B*, 2001, **65**, 035406.
412. X. Rong and A. M. Kolpak, *J. Phys. Chem. Lett.*, 2015, **6**, 1785–1789.
413. X. Du, M. Liu, J. Peng, H. Chun, A. Hoffman, B. Yildiz, L. Li, M. Z. Bazant and R. Gómez-Bombarelli, *ACS Cent. Sci.*, 2025, **11**, 1558–1572.
414. F. Riccius, N. Bergmann, H. H. Heenen and K. Reuter, *Adv. Sci.*, 2025, **12**, e13878.
415. Z. Zhang and X. Zhou, *MRS Commun.*, 2026, **16**, 167–179.
416. X. Du, J. K. Damewood, J. R. Lunger, R. Millan, B. Yildiz, L. Li and R. Gómez-Bombarelli, *Nat. Comput. Sci.*, 2023, **3**, 1034–1044.
417. D. Schwalbe-Koda, N. Govindarajan and J. B. Varley, *Digit. Discov.*, 2025, **4**, 234–251.
418. N. Rønne, A. Aspuru-Guzik and B. Hammer, *Phys. Rev. B*, 2024, **110**, 235427.
419. N. Govindarajan, G. Kastlunger, J. A. Gauthier, J. Cheng, I. Filot, A. Hagopian, H. A. Hansen, J. Huang, P. M. Kowalski, J. Liu, J. M. Lombardi, M. Maraschin, A. Peterson, H. S. Pillai, H. Prats, C. J. Price, R. van Roij, J. Rossmesl, R. R. Seemakurthi, S.-J. Shin, A. Smith, J.-X. Zhu and K. Doblhoff-Dier, *ACS Energy Lett.*, 2025, **10**, 4277–4288.
420. T. Wang, H. Iriawan, J. Peng, R. R. Rao, B. Huang, D. Zheng, D. Menga, A. Aggarwal, S. Yuan, J. Eom, Y. Zhang, K. McCormack, Y. Román-Leshkov, J. Grossman and Y. Shao-Horn, *Chem. Rev.*, 2025, **125**, 1420–1467.